FLOW AND HEAT TRANSFER IN MICROFLUIDIC DEVICES WITH APPLICATION TO OPTOTHERMAL ANALYTE PRECONCENTRATION AND MANIPULATION

by

Mohsen Akbari

M.Sc., Sharif University of Technology, 2005

B.Sc., Sharif University of Technology, 2002

THESIS SUBMITTED IN PARTIAL FULFILLMENT

OF THE REQUIREMENTS FOR THE DEGREE OF

DOCTOR OF PHILOSOPHY

IN THE DEPARTMENT

OF

MECHATRONIC SYSTEMS ENGINEERING

FACULTY OF APPLIED SCIENCE

SIMON FRASER UNIVERSITY

Summer 2011

APPROVAL

Name: Mohsen Akbari

Degree: DOCTOR OF PHILOSOPHY

Title of Thesis: Flow and heat transfer in microfluidic devices with application to optothermal analyte preconcentration and manipulation

Examining Committee: Dr. Woo Soo Kim (Chair)

Dr. Majid Bahrami; P.Eng (Supervisor)

Dr. David Sinton; P.Eng (Supervisor)

Dr. Bonnie Gray; P.Eng (Supervisor)

Dr. Carolyn Sparrey; P.Eng (Internal Examiner)

Dr. Boris Stoeber; P.Eng; (External Examiner); Department of Mechanical Engineering, University of British Columbia

Date Approved: July 21st, 2011

Abstract

This work describes a novel optothermal method for electrokinetic concentration and manipulation of charged analytes using light energy, for the first time. The method uses the optical field control provided by a digital projector to regulate the local fluid temperature in microfluidics. Thermal characteristics of the heating system have been assessed by using the temperature-dependent fluorescent dye method. Temperature rises up to 20°C (maximum temperature achieved in this experiment was about 50°C) have been obtained with the rate of $\sim 0.8^{\circ}\mathrm{C/s}$. The effect of the source size and light intensity on the temperature profile is investigated and the ability of the system to generate a moving heat source is demonstrated. A theoretical investigation is also performed by modeling the system as a moving plane source on a half-space. Effects of heat source geometry, speed, and power on the maximum temperature are investigated and it has been shown that by choosing an appropriate length scale, maximum temperature in dimensionless form becomes a weak function of source geometry. For the flow field control in the proposed system, the fundamental problem of fluid flow through straight/variable cross-section microchannels with general cross-sectional shapes are investigated. Approximate models are developed and verifications are performed by careful independent experiments and numerical simulations. Further verification is also performed by comparing the results with those collected from the literature.

The concentration enrichment in the present approach is achieved by balancing the bulk flow (either electroosmotic, pressure driven, or both) in a microcapillary against the electrophoretic migrative flux of an analyte along a controlled temperature profile provided by the contactless heating method. Almost a 500-fold increase in the local concentration of sample analytes within 15 minutes is demonstrated. Optically-controlled transport of the focused band was successfully demonstrated by moving the heater image with the velocity

of about 167μm/min. Transporting the concentrated band has been achieved by adjusting the heater image in an external computer. This ability of the system can be used for sequential concentration and separation of different analytes and transporting the focused bands to the point of analysis.

Keywords: microfluidics, lab on chip, preconcentration, manipulation, optothermal heating, transport phenomena, fluid flow, heat transfer

To my family, especially my father for his unconditional support and in memory of my mother.

Acknowledgments

Well, acknowledgments...! Looking back over the past several years and thinking about everything that has happened during my graduate career, I can see many difficulties. There were moments during my Ph.D. that I told myself:" ok! that's it! I am stuck with all these tasks and yet there is no progress. I am going to be doing this stuff forever!" But there were always people who helped me through those tough times and I am sure I could not survive those hectic times without their support. I would first like to thank my supervisors for their guidance, patience, and assistance. There are no words to describe Professor Majid Bahrami's patience in getting me started with my research and mentoring me from the initial steps towards the end of the program. He gave me excellent advices on how to handle different problems and how to present my ideas. I appreciate his technical advices as much as our friendly conversations about life, sports, and whatever else came up. Professor David Sinton was the first who introduced me to the field of microfluidics. I immediately admired his passion and dedication to his research and students. He got me started on the TGF project and pushed me to tackle some interesting problems. He always supported my ideas. I will never forget the time we spent in the lab disassembling a video projector to figure out what is going on there! I also would like to thank Prof. Bonnie Gray for her advice and service on my committee. I need to thank the lab members in Laboratory for Alternative Energy Conversion (LAEC) especially, Dr. Peyman Taheri who taught me how to use Latex! Dr. Ali Tamayol for his kind suggestions and the discussions we had on different topics, Dr. Ehsan Sadeghi, who was not only my lab mate, but was my roommate for two years. In addition, I would like to thank Mehran Ahmadi, Kelsey Wong, Golnoosh Mostafavi, Setareh Shahsavari, and Hamidreza Sadeghifar for the friendly environment they provided in LAEC. I also had a chance to work with The Sinton group at UVic during my Ph.D. I would like to thank my close friend Carlos Escobedo for his generous helps. Joe

Wang, Brent Scarff, Paul Wood, and Ali Kazemi were my other friends in the Sinton lab who were so kind and helpful to me. I am very thankful for the financial support of Natural Sciences and Engineering Research Council (NSERC) of Canada, the Canada Research Chairs Program, BC Innovation Council, and Simon Fraser University. Last but not least, I would like to thank my family in Iran. My father who always believed in me, for being an unending source of encouragement and support and inspiration throughout my academic career. I would like to dedicate the last words to my mother who passed away one month before I started my Ph.D. She was always an unlimited source of courage and hope for me and I wouldn't reach this level without her sacrifices.

Contents

List of Tables

List of Figures

Chapter 1

Introduction

1.1 Background and Motivations

Microfluidics is the science and technology in which small amounts of fluids (10^{-18} to 10^{-9} liters) are manipulated in channels with dimensions of one to hundreds of micrometers [1]. The wealth of interest and research in the technology has spurred the emergence of fields known as micro total analysis systems (μTAS) or lab-on-a-chip devices (LOCs) [2]. These microfluidic systems can be used in medical, pharmaceutical and defence applications; for instance, in drug delivery, DNA analysis, and biological/chemical agent detection sensors on micro systems. The fundamental benefits of scaling down transport phenomena to the micro (or nano) scales lead to several advantages of these systems over their macroscale counterparts: low sample and reagent consumption, effective heat dissipation due to higher surface area/volume ratio, faster separations with higher efficiency, existence of laminar flow, low power consumption, portability, and the ability to multiplex several assays.

One challenge posed by miniaturization lies in the detection of very dilute solutions of analytes in ultra-small volumes, nanoliters or less (see Figure 1.1 for the limitation of different detection techniques, adapted from [4]). In addition, there is frequently a mismatch between the extremely small quantities of sample used for analysis and the often much larger quantities needed for loading the sample into the microfluidic device and transporting it to the point of analysis. Table 1.1 shows the typical weight quantities of samples required for analytical testing; adapted from [3].

Improved temperature control is one of the main motivating factors for these microflu-

Table 1.1: Weight quantities of samples typically required for analytical testing; adapted from [3].

Years	Required sample amount
1960-1970	10-100 μg
1971-1980	1-10 μg
1981-1990	10-100 ng
1991-1995	1-100 pg
1996-2000	1-100 fg
2000-2005	10-100 ag

idic chip based systems. Active control of fluid temperatures is now central to many microfluidic, LOCs, and microelectromechanical systems (MEMS). Examples are DNA amplification [5], sample preconcentration and separation [6], flow regulation (valving and actuation) [7], molecular synthesis [8], manipulation of molecules [10], and highly integrated MEMS [9].

Addressing these challenges, the aims of this dissertation are to:

- introduce a novel heating method for local temperature control in microfluidics through which localized temperature zones in small dimensions (order of micrometers to millimeters) can be achieved. With this approach, the location and the shape of these temperature zones can be dynamically assigned. This enables dynamic thermal management of a microfluidic device.

- develop a flexible and contactless method for analyte preconcentration and manipulation with the ability to increase the local concentration of different analytes at any location along the microfluidic device and transport the concentrated band to the point of analysis.

- investigate the fluid and thermal transport in microscales for better understanding of the heat transfer and flow mechanisms in microscale. This provides a powerful tool for design and optimization of the proposed optothermal system.

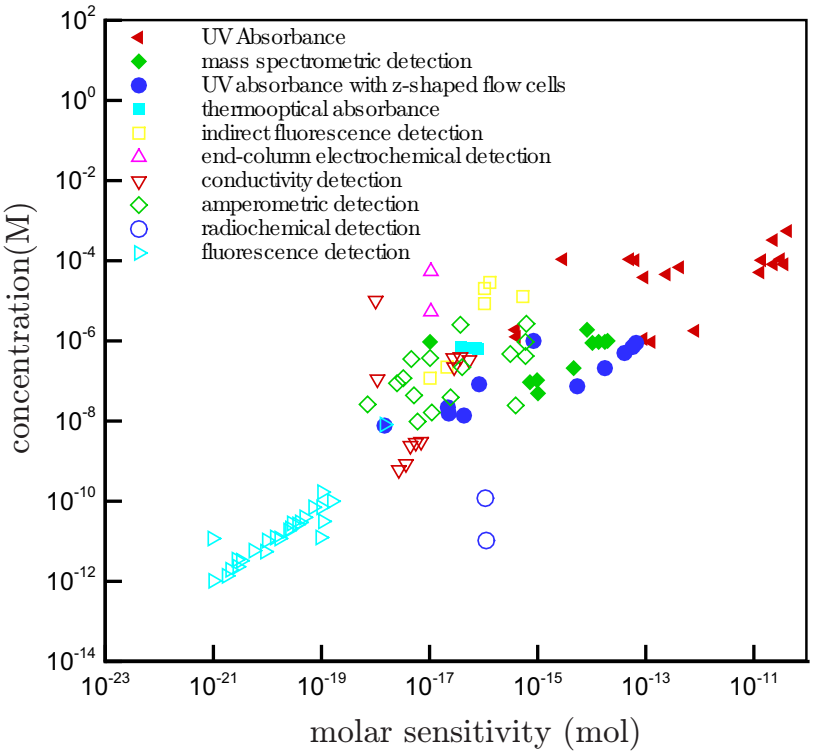

Figure 1.1: Detection techniques for capillary electrophoresis (adapted from [4]). Molar sensitivity (here defined as the number of moles detected) and concentration are plotted on the horizontal and vertical axes, respectively. Fluorescence detection is observed to have the highest sensitivity among other CE detection schemes.

To fulfill the research objectives, a systematic theoretical-experimental approach is designed to study three different fundamental problems involved in the present project:

- *hydrodynamics:* pressure driven and electroosmotic flow in microchannels with general cross-sectional area and constant/variable wall shapes.
- *heat transfer:* local fluid temperature distribution in microchannels in the presence of fluid flow and external stationary/moving heat source.
- *electrokinetics:* species distribution as a result of specific flow condition and temperature profile.

Figure 1.2 illustrates various components of the present research and its deliverables.

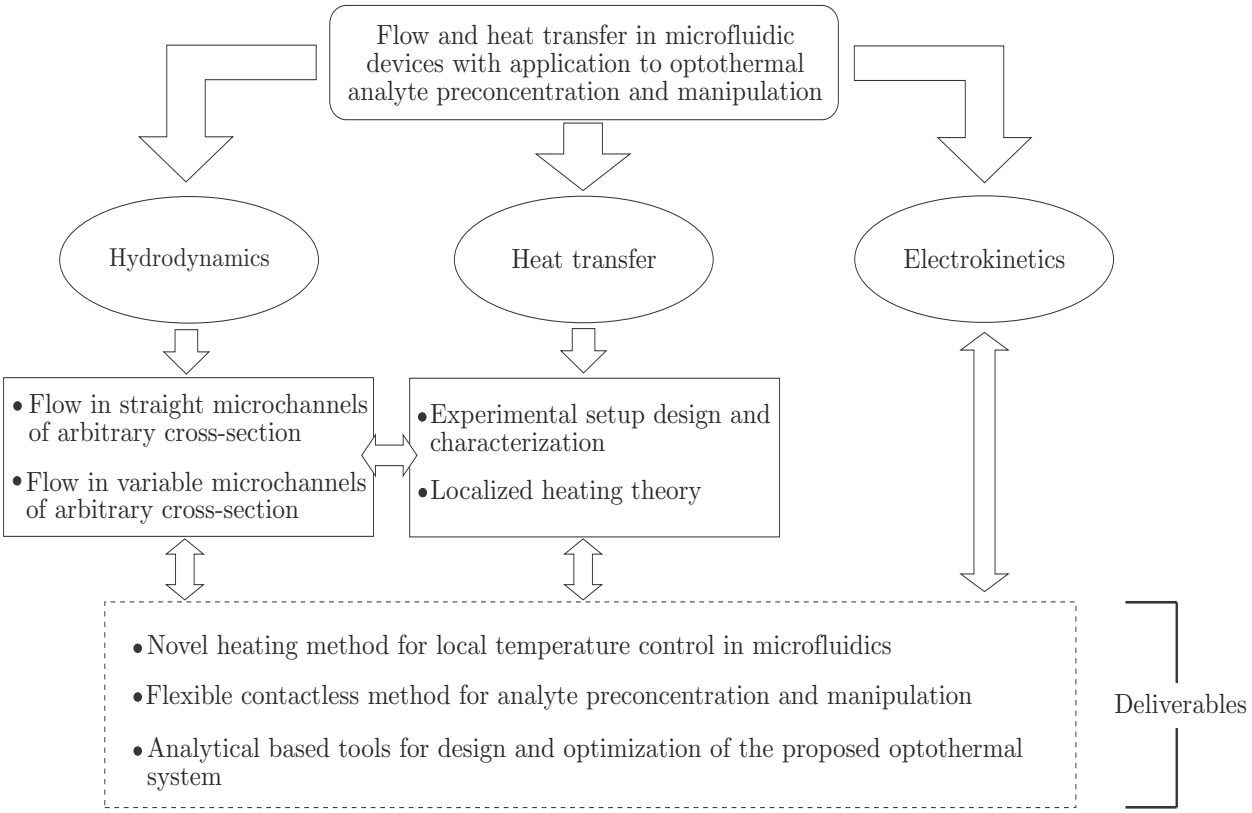

Figure 1.2: Scope of the present research, various components, and deliverables of the proposed research

1.2 Organization of the dissertation

This dissertation is comprised of four chapters which are organized as follows:

Chapter 1 is dedicated to the background and motivations of the present work. In Chapter 2, a comprehensive literature review is provided on three major aspects of this dissertation: (i) preconcentration techniques in microfluidics, (ii) heating methods in the context of temperature control in microfluidic and lab-on-chip devices, and (iii) fluid flow in microscale including experimental and numerical studies on both straight and variable cross-section microchannels as well as available analytical models for channels with various cross-sectional area.

Chapter 3 provides the summary of the contributions of present research. Optothermal

ous cross-sectional area.

Chapter 3 provides the summary of the contributions of present research. Optothermal analyte preconcentration and manipulation by means of a contactless heating system is demonstrated in Sec. 3.1 for the first time. Details of the experimentation, ability of the system to increase the local concentration of different model analytes and transportation of the focused bands along a microchannel is provided in Sec. 3.1. The focused band is shown to be successfully transported along a microcapillary by adjusting the image of the heater in an external computer.

Details of the contactless heating system is provided in Sec. 3.2 with the ability of the proposed system to control the location and size of the heated area as well as the amount of heat that enters the heated area. Moreover, the unique capability of the system for generating a moving heated area in a model microfluidic device is demonstrated. For better understanding of the temperature distribution due to a stationary or moving heat source as well as investigating the effects of the heat source shape on the temperature distribution, a detailed theoretical study is included in Sec. 3.2. Proposed theory is supported by an independent experimentation.

A detailed theoretical and experimental analysis of laminar flow in straight and variable cross-section microchannels of arbitrary shape is provided in Sec. 3.3. Pressure drop in microchannels as compared to theory based on arbitrary cross-section is investigated. An independent experimentation is designed and performed to compare the general approximate model for straight microchannels of general cross-section with experimental data. Later, the approximate model is extended to slowly-varying micrchannels of arbitrary cross-section and a unified model is proposed which accounts for both frictional and inertial effects. The same experimental setup is used, but for variable cross-section channels to validate the proposed approximate model. Further verification of the model is performed by comparing the results with the available numerical and experimental data in the literature.

Finally, Chapter 4 provides conclusions and future investigations that may stem from this work. Conceptual devices are included that operate based on the principles presented in this study. The objective of this dissertation and future research is the development of flexible, simple, reliable and commercializable micro-analytical devices.

Bibliography

[1] G. Whitesides, The origins and the future of microfluidics, Nature 442 (7101) (2006) 368–373.

[2] G. J. Sommer, Electrokinetic gradient-based focusing mechanisms for rapid, on-chip concentration and separation of proteins, Ph.D. Dissertation 2008, Univ. Michigan, MI.

[3] N. Guzman, R. Majors, New directions for concentration sensitivity enhancement in CE and microchip technology, LC GC NORTH AMERICA 19 (1) (2001) 14–31.

[4] S. Devasenathipathy, J. Santiago, Electrokinetic flow diagnostics, Microscale Diagnostic Techniques (2005) 113–154.

[5] M.U. Kopp, A.J. de Mello, and A. Manz, Chemical amplification: continuous-flow PCR on a chip, Science 280 (1998) 1046-1048.

[6] D. Ross, L. Locascio, Microfluidic temperature gradient focusing, Anal. Chem. 74 (11) (2002) 2556–2564.

[7] T. Thorsen, S.J. Maerkl, and S.R. Quake, Microfluidic large-scale integration, Science 298 (2002) 580-584.

[8] S. Caddick, and R. Fitzmaurice, Microwave enhanced synthesis, Tetrahedron 65(17) (2009) 3325–3355.

[9] A. Richter, G. Paschew, Optoelectrothermic control of highly integrated polymer-based MEMS applied in an artificial skin, Advanced Materials 21(9) (2009) 979–983.

[10] S. Duhr, and D. Braun, Why molecules move along a temperature gradient PNAS 103(52) (2006) 19678-19682.

Chapter 2

Literature Review

In this chapter, a comprehensive literature review will be performed on three major aspects of the present thesis; i.e., preconcentration techniques in microfluidics, heating methods in the context of temperature control in microfluidic and lab-on-chip devices, and fluid flow in microscale. The first part summarizes the available preconcentration methods in the literature including the temperature gradient focusing techniques used in this work. The second part of this section provides a review on the available heating strategies used in the literature to control the local temperature in microfluidicc device along with a brief discussion on the advantages and disadvantages of each method. The last part of this section is dedicated to a comprehensive review on the available theoretical/experimental studies reported in the literature for the flow in variable cross-section microchannels of arbitrary cross-section. This part will provide the required background for the design and optimization of the proposed optothermal system in the context of bulk flow control in microscale.

2.1 Preconcentration Techniques

Since the introduction of "micrototal analysis systems (μTAS)" by Manz et al. [1] in 1990, various chemical operations have been miniaturized and integrated onto the planar chips [2–5]. Capillary electrophoresis (CE) analysis has also been miniaturized and applied to microfluidic devices, which is called microchip electrophoresis (MCE) [6]. It is well known that due to the short optical path length or extremely small amount of injected samples, the low-concentration sensitivity in CE and MCE is often problematic [7]. Thus, several

approaches have been proposed in CE and MCE based on (i) increasing the optical path length and (ii) using preconcentration techniques. Enhancement of the path length can hardly be performed in microsystems because of the fabrication limitations. Thus, sample preconcentration techniques have been mainly employed in CE and MCE.

A great deal of effort has been devoted to develop new methods of preconcentration and separation or to improve the existing methods. The available methods can be classified into two categories: dynamic and trapping methods. The dynamic methods are based on the variation of migration velocities of analytes, while in the trapping methods analytes are trapped and concentrated at a fabricated micro- or nano-structure such as packed beds, immobilized polymers, and membranes [7]. A detailed treatment of the trapping techniques is beyond the scope of this dissertation. However, the reader is referred to a recent review paper of Sueyoshi et al. [7]. The remaining of this section is devoted to the detailed literature review of the dynamic methods.

Table 2.1 lists the available dynamic preconcentration methods in the literature and the typical reported concentration enrichment. The dynamic methods can be categorized into the following groups:

1. field amplified stacking (FAS)
2. isotachophoresis(ITP)
3. sweeping
4. electric field gradient focusing (EFGF)
5. isoelectric focusing (IEF)
6. temperature gradient focusing (TGF)
7. thermophoresis focusing (TPF)

In the field amplified stacking method (FAS), which has been first employed for MCE by Jacobson and Ramsey [8] in 1995, a sample solution with low conductivity is injected into a microchannel filled with high conductivity buffer solution. Concentration enrichment occurs around the boundary due to the difference in the local electric field in high and

Table 2.1: Available dynamic preconcentration methods in the literature.

method	typical concentration enrichment(-fold)	concentrated analytes	comments
field amplified stacking (FAS)	$4-1100$	fluorescent dyes, amino acids, proteins, metal ions,amines, steroids, DNA molecules, GAGs	• concentration enrichment is difficult for samples containing high-concentration salts • neutral analytes cannot be concentrated withought the help of micellar electrokinetic chromatography • distortion of the high/low conductivity boundary decreases the enrichment efficiency
isotachophoresis(ITP)	$10-10^6$	paraquat, diquat, Inorganic anions, SDS-proteins, ACLARA eTags, alexa fluor 488, BODIPY, DNA fragments, HAS, tyrosine kinase, DNA ladder immnocomplex,	○ the electrophoretic mobility must be determined before each test • cannot be performed for neutral analytes
sweeping	$100-500$	Rhodamine dyes, Fluorescein dyes, Estrogens	• neutral analytes can be concentrated • only useful for small hydrophobic analytes with a high affinity for a mobile micellar phase
electric field gradient focusing (EFGF)	$150-10^4$	proteins, peptides	• ion-permeable membranes are required to maintain the hydrodynamic counterflow and the electric field gradient in the tapered channel • applicable to large molecules.
isoelectric focusing (IEF)	–	proteins, peptides, SDS-proteins, drugs, R-Phycoerythrin	• limited to analytes with an accessible pI, • low concentration enrichment fe or proteins due to the low solubility of most proteins at their pIs
temperature gradient focusing (TGF)	$100\text{-}10^4$	proteins, fluorescent dyes, amino acids, polystyrene particles GFP, DNA,	• buffer with temperature dependent ionic strength is required
thermophoresis focusing (TPF)	16	DNA molecules	• height temperature gradient is required focusing is slower than other methods

low conductivity solutions. Several papers have been devoted to improve the enrichment efficiency of the original idea in MCE by introducing new injection techniques [9–12], combining FAS with micellar electrokinetic chromatography (MEKC) for neutral analytes [13], and performing surface treatment to eliminate the distortion of the high/low conductivity boundary [14–17].

In order to overcome the main drawback of FAS method in the enrichment of samples containing high-concentration salts, isotachophoresis method (ITP) was first introduced in MCE by Walker et al. [18] in 1998. In the ITP, an ionic sample solution is introduced between leading (LE) and terminating (TE) electrolyte solutions with the condition of $\mu_{ep,LE} > \mu_{ep,S} > \mu_{ep,TE}$, where $\mu_{ep,LE}$, $\mu_{ep,S}$, and $\mu_{ep,TE}$ are the electrophoretic mobilities of LE, sample and TE solutions, respectively. By applying an electric field, sample ions are separated in the order of electrophoretic mobilities, and then all the divided zones migrate with a uniform velocity (axial average velocity) toward a detection point. The method has been improved by several authors such as Kaniansky et al. [19], Graß et al. [20], Huang et al. [21], Ma et al. [22], and Bahga et al. [23] for lab-on-chip devices. The main disadvantage of ITP is that the electrophoretic mobility of LE, sample and TE should be determined before each experiment. Moreover, this method can only be applied to charged analytes.

Both FAS and ITP methods require charged molecules to produce the concentrated bands. The first concentration enrichment and separation of neutral compounds was developed by Quirino and Terabe [24] in 1998 by a method usually referred to as the *sweeping* method. In this method, the interactions between the sample and micelle allow the separation of neutral samples. The method has been first miniaturized by Sera et al. [25] followed by further modifications performed by Liu et al. [26], Chen et al. [27], and Gong et al. [28] to improve its efficiency. Although over one million-fold enhancement is reported in the literature for CE [29, 30], the sweeping is not so effective in MCE and typical concentration enrichments of 100-500 can be found in the literature. Moreover, the stacking effect (the distortion of the high/low conductivity boundary) still exists in the sweeping method which eventually lessens the concentration enrichment efficiency.

In all above-mentioned methods, the concentration enrichment of the compounds increases with time along a moving boundary which requires relatively long channels to achieve higher concentrations and/or better separation efficiencies. To overcome such a problem, another class of preconcentration methods have been utilized which are usually

referred to as *equilibrium gradient focusing (EGF)* methods. These methods provide the ability of simultaneous concentration and separation of analytes [31]. In EGF, the migration direction of analytes is inversed along a channel while the bulk velocity of the background buffer is kept constant. As a result, analytes are *focused* at the points where the migrating velocities become zero. Due to the nature of the focusing, peaks become both narrower and more concentrated throughout the separation, allowing for higher resolutions and sensitivity. The most prevalent example of the equilibrium gradient focusing methods is called isoelectric focusing (IEF) [32], which involves the focusing of analytes at their respective isoelectric points (pIs, the pH at which a particular molecule carries no net electrical charge) along a pH gradient. IEF is first used in a miniaturized format by Hofmann et al. [33] followed by further modifications performed by several authors to shorten the focusing time and increase the separation resolution [34–37]. IEF is limited in application because it is restricted to use with analytes with an accessible pI. Additionally, the concentration to which a protein can be focused with IEF is severely limited by the low solubility of most proteins at their pIs [38].

Electric field gradient focusing (EFGF), is first introduced by Koegler and Ivory [39, 40] in 1996 to increase for the concentration enrichment of proteins. In EFGF, sample molecules migrate in a channel with an electric field gradient, and the focusing occurs by balancing the electrophoretic velocity of an analyte against the bulk velocity of the buffer containing the analyte. The electric field gradient is usually generated by using a tapered channel filled with a ion-permeable membrane. Although EFGF is reported to be an efficient method, concentration enrichment up to 10^4 is reported in the literature[7], only large molecules or particles that cannot pass through the membrane can be concentrated.

Recently, by using the thermophoresis effect (the phenomenon of the motion of suspended particles induced by the temperature gradients in fluids [41]) instead of electrophoresis velocity, Duhr and Braun [42] introduced a novel method for the focusing of DNA molecules. The method is called thermophoresis focusing (TPF). An IR laser beam is used to generate high temperature gradients ($\sim 10^6\,^{\circ}\mathrm{C/m}$) and 16-fold enrichment is reported within 15 minutes. In another work, Weinert and Braun [122] developed an optical conveyor based on this method to increase the concentration of DNA molecules. TPF is a promising method due to the fact that it can be applied to both charged and neutral compounds. However, the method is slow [42] and requires high temperature gradients for

small particles.

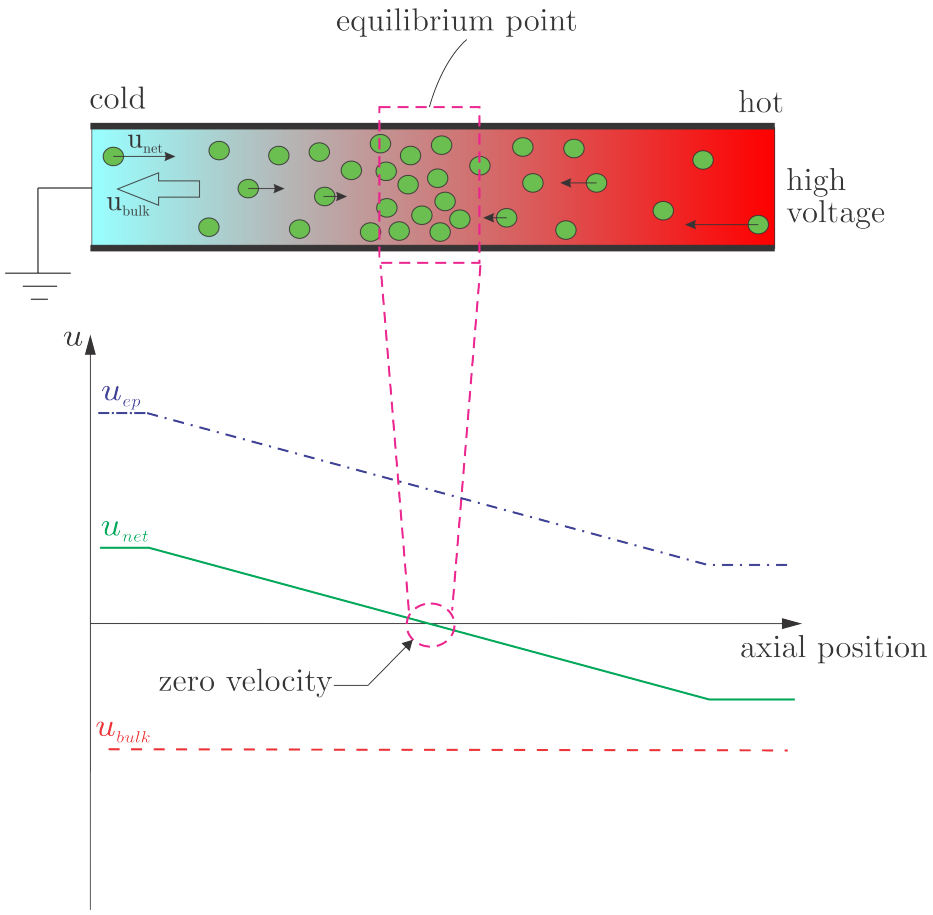

Figure 2.1: Schematic illustration of temperature gradient focusing condition in a straight microchannel. A linear temperature gradient is produced with hot and cold regions on the right and left, respectively. By applying a high voltage and negative polarity on the right hand side, negatively charged particles (depicted by green circles) move toward the ground electrode (on the right) with the electrophoretic velocity of u_{ep}. The electrophoretic velocity varies along the temperature gradient and is balanced by a constant bulk velocity at an equilibrium point where the net velocity becomes zero.

To overcome the major drawbacks of other focusing methods, the temperature gradient focusing (TGF) technique is introduced by Ross and Locascio[38] in 2002. TGF is more advantageous than EFGF and IEF in terms of easier operation (no membrane or salt bridge

is required) and the applicability to a wide range of analytes. Its principle is the same as EFGF; in both methods the electrophoretic velocity is balanced by the bulk velocity which can be either, electroosmotic velocity (EO), or a combination of pressure driven velocity (PD) and EO. Figure 2.1 shows the schematic illustration of the temperature gradient focusing in a straight microchannel with a linear temperature distribution. The key insight of the TGF method is that a buffer with a temperature-dependent ionic strength would be required for TGF; otherwise the primary temperature-dependent parameter would be the viscosity and temperature gradient does not affect the electrophoretic velocity. Also, by using relatively short microchannels, resolutions comparable to other methods utilizing long separation channels can be achieved [43]. Several works have been devoted to TGF since its first introduction, mostly done by Ross and coworkers [44–51]. These studies are listed in Table 2.2. As can be seen, TGF can be used in the analysis of a wide variety of analytes including chiral-compounds and pharmaceutical molecules [45], DNA molecules [38, 50], amines, amino acids [38, 45, 47], proteins [38, 52–54], and most of the fluorescence dyes. TGF method in its original form has three main drawbacks:

- it only works for charged analytes,
- its peak capacity is limited; only 2-3 peaks can be simultaneously focused and separated,
- integration on a lab-on-chip device is difficult.

Addressing these issues, several improvements have been performed to the original TGF method. Balss et al. [44] and later Kamande et al. [48] combined the TGF and MEKC methods to concentrate and separate neutral analytes. To improve the peak capacity of the method, Hoebel et al. [47] introduced a novel scanning separation method in which the analytes can be sequentially separated by applying a variable bulk flow rate over time. Kim et al. [52, 53] used a tapered microchannel on a PDMS chip for the formation of the gradient of Joule heating. By using a single channel device without applying pressure, the concentration of FITC-labelled BSA is increased to at least 200-fold within 2 min. However, due to "the thermal runaway" (i.e. a situation where an increase in temperature changes the electrical conductivity in a way that causes a further increase in joule heating, leading to unstable temperature increase), unstable focusing bands have been reported [52].

Performing TGF in a PDMS/Glass hybrid microchip by Matsui et al. [55], TGF challenges in polymeric devices are discussed. It has been highlighted that the variation of the surface zeta-potential due the temperature distribution, highly concentrated analytes around the focusing point, and using different materials (glass and PDMS) leads to the distortion of the ideal plug-wise velocity and lowers the focusing and separation resolution.

Under the assumption of dilute solution and low Reynolds number, the detailed theory of TGF is investigated by Ghosal and Horek [56]. Considering the variation of the electrical conductivity and surface zeta-potential in the presence of both pressure driven and electroosmotic flow, analytical expressions have been proposed for the velocity field and concentration distribution. Their theory [56] takes into account the fact that the axial inhomogeneity created by the variation of the focusing parameters along the channel would create an induced pressure gradient and associated Taylor-Aris dispersion. The theory of Ghosal and Holek [56] is verified by Huber and Santiago [57, 58] through experimental studies and it has been shown that the one-dimensional averaged convection-diffusion equation for the distribution of species is reasonably accurate for any value of Peclet numbers (which is defined as the ratio of convection over diffusion) and applied electric fields. The assumption of dilute solution fails when low concentration buffers are used or the concentration of the sample increases such that the interactions between the sample and buffer ions are not negligible anymore. Addressing this issue, Lin et al. [31] performed an analytical/experimental study to investigate the nonlinear sample-buffer interactions in TGF. They [31] showed that when the enhanced concentration of one or more of the ions in the sample becomes comparable to the background electrolyte ion concentration, the electric field driving the concentration enhancement will be distorted, and the enhancement will be less effective.This limits the separation resolution of the method and/or leads to unstable bands. Several other numerical studies have also been carried out for the case of TGF via joule heating effect in a variable cross-section channel by Sommer et al. [53], Tang et al. [59] and Ge et al. [60] with the goal of integrating TGF on a lab-on-chip device.

2.2 Fluid temperature control in microdevices

Improved temperature control was one of the main motivating factors for some of the earliest microfluidic chip based and microelectromechanical systems (MEMS). Active control

Table 2.2: Summary of previous works on TGF.

Author	year	concentrated analytes	maximum reported concentration enrichment/time
Ross and Locascio [38]	2002	Oregon Green 488 carboxylic acid, Cascade Blue hydrazide,serine, tyrosine, GFP, fluorescently labeled DNA, aspartic acid, fluorescently labeled polystyrene microshperes	10000/100 min
Balss et al. [44, 45, 50]	2004	DNA, Rhodamine B, amino acids, small pharmaceutical molecules	600/30 min
Ghosal and Horek [56]	2005	-	-
Shackman et al. [46]	2006	Fluorescein, carboxyfluorescein (FAM), Blue DND-167 and 192 dyes, and Lysosensor	-
Hoebel et al. [47]	2006	L-aspartic acid, fluorescein (FAM), succinimidyl ester	2000/time not reported
Kim et al. [52, 53]	2006,2007	Fluorescein-Na, BSA	200/2 min
Kamande et al.[48]	2007	coumarin laser dyes	25/min
Huber and Santiago [57, 58]	2007	fluorescein, Bodipy proprionic acid, and Oregon Green 488 carboxylic acid	-
Munson et al. [49]	2007	Oregon Green 488 carboxylic acid, 5-carboxyfluorescein, succinimidyl ester	1000/time not reported
Matsui et al. [55]	2007	Oregon Green 488 carboxylic	30/45 sec
Lin et al. [31]	2008	Oregon Green 488 carboxylic	-
Tang and Yang [59]	2008	-	-
Becker et al.[54]	2009	Fluorescence dyes, different proteins	2/ time not reported
Ge et al. [60]	2010	Fluorescein-Na	500/1 min

of fluid temperatures is now central to many microfluidic and lab on chip applications. Examples include: chemical synthesis in microreactors [61, 62], polymerase chain reaction (PCR) (a molecular biological tool to replicate DNA and create copies of specific fragments of DNA; see Ref. [64] for a comprehensive review), preconcentration and separation techniques [38, 44–53, 55], and flow and analyte manipulation [66–68, 97]. The following section is dedicated to the review of available heating methods for temperature control in microfluidic and MEMS applications. We divide the present heating technologies into two major categories of contact and contactless methods. However, some techniques that cannot be categorized into these two major groups are separately classified as miscellaneous heating methods.

2.2.1 Contact methods

In contact heating methods, the desired temperature profile is usually created by means of electrothermal conversion in a heating element, which is in direct contact with the source of power and its components. Table 2.3 lists the summary of the available contact heating techniques in the literature along with their applications in microfluidic systems. Contact methods can be divided into the following groups:

- thin film heaters
- heating/cooling blocks
- embedded resistance wires/conductive filled epoxy
- flexible printed circuits
- hot/cold water streams

Thin film heaters

Thin film heating elements are one of the most popular formats of contact heating methods that have been widely used in the literature. Thin film heaters have been reported to be used in PCR analysis [69, 81, 93–96], patch clamping, chemical synthesis, and cell culture [62, 63, 75, 77–79], flow manipulation [65, 76, 97], fluidic self-assembly [98], gas sensors, and micro-calorimeters [83].

Table 2.3: Summary of contact heating methods for microfluidic applications

method	applications	comments
thin film	• DNA amplification • patch clamping, chemical synthesis, and cell culture • flow manipulation • fluidic self-assembly • gas sensors and micro-calorimeters	• main materials:Pt, polysilicon, and ITO • fast thermal responses ($\sim$0.5°C/ms), smaller heaters gives faster responses • requires complex fabrication preocess • array of heaters in an integrated device requires a complex controling system • fixed geometry, no on-demand control on the location and size of the heater
heating block	• DNA amplification • preconcentration and separation of analytes • fluid steering	• types: metallic blocks and Peltiers modules • slow temperature ramps • field of view blockage • large footprints
embedded resistance wires or conductive filled polymer	• flow measurement • particle manipulation via thermophoresis effect	• portable and inexpensive • non temperature distribution due to non uniform filling of the channels with epoxy and/or contact resistance between the wire and fluidic channel
flexible printed circuits	• DNA amplification	• low cost • heating rate $\sim$8°C/s • functionality is not demonstrated for flow through DNA amplification
hot/cold water streams	• DNA amplification • protein conformation analysis • cell imaging	• complex system, need syringe pumps, lines of water, hot/cold Peltiers, etc. • requires complex fabrication • heating rate $\sim$4°C/s • able to reach temperatures below the room temperature

The fabrication process includes thin film deposition techniques followed by micromachining methods to form the heating elements on a microfluidic device. For better thermal stability a thin film sensor is usually fabricated using the same method to record and control the temperature at the vicinity of the heating element. Most common materials for the fabrication of thin film elements are platinum (Pt) [62, 81, 93, 94, 98], polysilicon [69–71, 97], and indium tin oxide (ITO) [74–79]. Pt is the most commonly used material due to its ability to withstand high temperatures, good chemical stability, high antioxidation and purity, and easy micromachining [64]. However, in recent years, much attention has been paid to heater elements made from ITO because of its advantageous properties such as optical transparency, low resistivity, and strong adhesion to glass. Polysilicon is a material consisting of many small silicon particles and is used in doped form for thin film heater elements. Common dopant for polysilicon heaters are arsenic, phosphorus, and boron [12]. The amount of dopants used in the compound controls the electrical characteristics of a polysilicon thin film.

In addition to the above-mentioned materials, nickel (Ni) [82–84], aluminium (Al) [72, 73], silver/graphite inks [85], silver/palladium [86, 87], nichrome [88–90], and aluminium nitride [91] have also been used in the fabrication of thin film heaters in microfluidic applications.

The ability to produce small features by micromachining reduces the thermal mass of the system, thus ultra-fast heating ramps can be achieved. For instance, heating rates up to about $500^{\circ}\mathrm{C/s}$ have been obtained by using very small heaters with the size of 100 μm for patch-clamp studies [62]. In order to minimize heat leakages to the ambient and/or other components of the microchip, low thermal conductivity materials such as SU-8 (thermal conductivity 0.2 W/m.K), PDMS (thermal conductivity 0.18 W/m.K), and Pyrex glass (thermal conductivity 1.1 W/m.K) instead of silicon (thermal conductivity 150 W/m.K) to construct microchannels [62]. Furthermore, to minimize the heat losses through lead wires, long heaters can be designed such that the total heater electrical resistance becomes much larger than the resistance of the leading wires.

Although the fabrication process for thin film heater patterning is well established, the process is still complicated, time consuming and typically requires clean room facilities. Also, once the heating elements are fabricated, no changes in the heater size and location can be made. Visibility limitation is another challenge that has to be taken into account

when a thin-film heating system is designed. Using ITO as a heating material and transparent materials such as SU-8 and PDMS is recommended to overcome this issue.

Heating/cooling blocks

Utilizing heating/cooling blocks is another popular method that has been widely used in the literature for temperature control in microfluidic devices. In this method heating is provided by the attachment of a Peltier element or a cartridge heater inserted into a metal block to the substrates. For cooling, a coolant (usually water) is passed through a coil that is fabricated in a metal block. Cold Peltier modules can also be employed to provide the required cooling. The main advantage of using heating and cooling blocks compared to thin-film heaters is their simpler fabrication process in which micromachining and deposition processes are usually not required and there are less sealing issues involved.

Heating/cooling blocks have been widely used in microfluidic DNA amplification systems (PCR) [100–103]. Challenges such as large thermal masses and thermal cross-talk between three temperature zones in continuous-flow systems make it hard to achieve fast thermal transitions in the thermal cycles and/or separate different reaction zones with different temperatures. These issues have led to several modifications in the heating block-based PCR systems; examples are using continuous flow thermal gradient PCR [104] and/or improving the insulating methods by utilizing new materials [105]. In addition to PCR systems, heating blocks have also been used in preconcentration and separation of sample analytes via temperature gradient focusing (TGF) [38, 44, 45, 55, 57, 99, 106] and fluid steering [107]. In these applications, lower heating and cooling rates have less importance, but large footprints, optical blockage of the field of view due to the existence of metallic heating and cooling elements, and the difficulty in the integration of the heating/cooling elements on a microchip assembly become challenging issues. Moreover, in the design and fabrication of heating/cooling block microfluidic systems, good thermal contact between the heating/cooling element and process zone should be ensured. To do so, several conduction-supporting materials such as mineral oil [108] or metallic thin film wafers [102] can be used.

Embedded resistance wires or conductive-filled polymers

In the interest of simplifying the fabrication process and enhancing the portability of the microfluidic device, embedded resistance wires and/or conductive-filled polymers methods have been used in some papers [92, 109–112]. Fu and Li [109] presented a simple heating method by embedding a resistance wire into a PDMS chip to provide localized heating. Two different configurations of point and line heaters were fabricated and it was shown that by putting the heaters on the side of the channels, the blockage of the field of view can be avoided. Using a similar approach, Fu and Li [110] proposed a method for the measurement of average flow velocity in microcapillary. A Gaussian shape temperature distribution was generated by applying a localized heat pulse with the resistance wire. The average fluid velocity was then determined by monitoring the variation of the peak temperature location with time. Although the fabrication is simple and cost-effective, accurate positioning of the heater with respect to the heated channel is unlikely. This leads to non-uniform contact resistant between the heating element and the heated microchannel; thus, less uniformity in the temperature profile can be observed. Moreover, since the electrical resistance of the resistance wires are usually in the same order as the connecting wires, a considerable amount of heat is generated in the leading wires and the contacts.

In another attempt, Vigolo and coworkers [92] filled auxiliary channels beside a main channel with a silver-filled two component epoxy at room temperature and then cured it at high temperatures (80°C) for about an hour to form heating elements. Different configurations of the auxiliary channels were investigated and it was shown that uniform temperatures (with the temperature stability of $\pm 2-3$°C) can be obtained by using two parallel auxiliary channels on the side of the main channel. Later, they [111] used this approach to produce a controlled temperature gradient across a microchannel and investigate microfluidic separation based on the thermophoresis effect. Challenges posed by this simple and cost-effective method are the difficulty of the method to be used in integrated microfluidic devices, non-uniform filling of the epoxy inside the auxiliary channel, and non-negligible electrical contact resistance between the epoxy and the leads.

Flexible printed circuits

In the case of cost/fabrication trade-off, a simple and cost-effective method is to use the flexible printed circuit (FPC) technology. Shen and coworkers [113] used this method to design a stationary (single chamber) PCR thermocycler. Their glass chip-based device was made from low cost materials and assembled together with adhesive bonding. Reasonable temperature stability of $\pm 0.3^{\circ}\mathrm{C}$ was reported with the maximum transitional rate of $8^{\circ}\mathrm{C/s}$. Major challenges associated with this approach are to: (i) find appropriate biocompatible adhesive for bonding, which can stand high temperatures up to $100^{\circ}\mathrm{C}$ and shows no inhibition to chemical reactions; and (ii) establish reliable electrical connections to ensure signal integrity, prolong lifetime of interconnects, and avoid contamination of the fluid sample [114]. This method has not been reported to be used in other microfluidic applications so far.

Hot/cold water streams

In many of the above-mentioned methods, cooling is usually based on natural convection to the ambient; thus temperatures below the room temperature is not possible. To overcome this issue, Casquillas et al. [116] proposed a rapid heating/cooling method by using hot and cold streams of water for the application of high resolution cell imaging. The method includes two hot and cold Peltier modules connected to a temperature control channel and a main channel for the chemical analysis. Each Peltier module was set to a certain temperature and the working temperature of the main channel was controlled by changing the direction of water flow using a syringe pump. Relatively fast temperature responses of $\sim 4^{\circ}\mathrm{C/s}$ was obtained using this method. Similar approach has been used for other applications such as DNA amplification [117] and protein conformation analysis [115]. Major drawback associated with this method is its complexity due to number of involved components. This hinders the possibility of such a system to be integrated on a microfluidic device.

2.2.2 Contactless methods

The contact heating methods described in the previous section has number of inherent drawbacks: (1) they usually have large thermal mass, which limits the thermal response of

the system; (2) the fabrication process is fairly complex, time consuming, and/or expensive; (3) once the microchip is fabricated *a priori*, on-the-fly reconfiguration of the system is not possible; (4) there is a need for extensive interfacing with the external environment and elaborate proportional/integral/derivative (PID) control; this becomes a big issue when integration with other elements of a microchip should be taken into account; and (5) localized heating without affecting other parts of the microchip assembly through connecting elements is hard to achieve and/or requires complex design. These restrictions have triggered a great deal of interest in the development of contactless heating approaches in which the heating part is not in direct contact with the source of power. Available contactless methods can be divided into six groups:

- halogen/tungsten-based
- laser-based
- digital projection-based
- hot/cold air-based
- microwave irradiation-based
- induction-based

Table 2.4 lists these methods along with their applications in microfluidic systems and MEMS.

Halogen/Tungsten lamp

Halogen/Tungsten lamps emit a continuous spectrum of light, from near ultraviolet (UV) to deep into the infrared (IR) [143]. A tungsten/halogen lamp can be an ideal contactless heat source due to many advantages such as: simple design, low price, and almost instantaneous transition times for the lamp to reach very high temperatures [144]. Oda and coworkers [144] utilized a tungsten lamp to perform PCR analysis in a single-well (stationary) format. The amount of heating was controlled by regulating the power consumption of the lamp and the cooling was provided by using compressed air at room temperature. To eliminate wavelengths that could interfere with the PCR reaction and to focus the light, a lens and

Table 2.4: Summary of contactless heating methods for microfluidic applications.

method	applications	comments
Halogen/Tungsten lamp	• DNA amplification	• ultra fast heating rates up to $\sim 65^{\circ}C/s$ • multiplexing is hard to perform • requires additional optics to eliminate wavelengths intefering the reaction • low power efficiency
laser-based	• DNA amplification • preconcentration and analyte manipulation • flow regulation	• provides a focused light thus needs less energy • excellent for localized heating • requires accurate positioning of the laser beam • needs technical skills • ultra fast heating rates up to $\sim 67^{\circ}C/s$
digitized light-based	• sample preconcentration and manipulation • valving and actuation	• no complex fabrication or controlling system is required • flexible and easy to apply with no special skill • provides localized heating • not energy efficient • requires accurate optical design
hot-air based	• DNA amplification	• fast thermal responses up to $10^{\circ}C/s$ • commercial thermocyclers are available for DNA amplification • localized heating is not easy to achieve
microwave-based	• DNA amplification • molecular and nanoparticle synthesis • proteomic analysis and cell lysis • water actuation • heating water drops	• ultra fast heating rates up to $\sim 2^{\circ}C/ms$ • requires complex fabrication and controlling system
induction-based	• DNA amplification • cell lysis • microchip thermal bonding	• relatively low power consumption • simple fabrication steps and controlling systems • fast thermal responses up to $6^{\circ}C/s$ • hard to be integrated in a microfluidic system • the winding should be close to the heater to obtain optimum energy transfer

filter system was employed. They [144] reported rapid heating and cooling rates of $\sim$10 $^{\circ}$C/s and $\sim$20 $^{\circ}$C/s, respectively. With a similar approach but in a fused silica capillary, Hühmer and Landers [145] performed a PCR analysis with less reagent consumption. Very fast heating rate of $\sim$65 $^{\circ}$C/s was reported in their work while the cooling rate of $\sim$20 $^{\circ}$C/s was achieved by utilizing a compressed air jet. In another work, Ke and coworkers [146] used a regular halogen lamp (100 W) and an on-off fan to perform PCR analysis in a thermal cycler chamber with the heating and cooling rates of $\sim$4 $^{\circ}$C/s.

Despite the advantages associated with a halogen/tungsten lamp as a heat source, this approach suffers from various drawbacks. The lamp light is non-coherent and non-focused. This usually leads to large focused projections and limits the heating efficiency when heating of small dimensions is required. Accurate positioning of the reaction mixture at the focal distance of the optics is also required for the system to work with maximum efficiency. In terms of power consumption, the method is not efficient due to the energy losses in the air and optics. This complicates the design and development of battery-powered portable microfluidic devices.

Laser-based systems

With recent interests in optofluidic [147, 148], laser-based systems have become attractive methods for local temperature control in microfluidics. In these systems, the photothermal effect produced by a laser beam is transferred to heat by absorbing in a target material. The target material can be a black ink point [118], a coated surface with gold or ITO [67], or the working fluid itself [42]. The major advantage associated with a laser-based system is that the light beam is coherent and focused. This results in less energy consumption (power consumption is usually in the order of milliwatts), higher efficiencies and possibility of the system to become portable. Another advantage of such a system is the high resolution of spatially localized heating, the ability to move the heated area along the chip, and the property of being a point source.

Laser-based systems have been utilized in many microfluidic applications. Takana and coworkers [118] and later Slyandev and coworkers [119] used an IR diode laser for the temperature control in a PCR microdevice. They [118, 119] used black ink to absorb the laser beam energy and convert it into heat. Ultra-fast heating and cooling rates of $\sim$65 $^{\circ}$C/s and $\sim$53 $^{\circ}$C/s have been reported with a beam diameter of about 150 μm [119].

Faster temperature ramps can be achieved by decreasing the size of the laser beam.

In another application, Braun and Libchaber [120] used an IR laser beam with the diameter of about 25 μm to increase the local temperature of an aqueous solution and trap DNA molecules via thermophoresis effect and free convection in a microchannel. With temperature gradients as high as $\sim 1.8 \times 10^5\,^{\circ}\mathrm{C/m}$ (corresponding temperature difference is $\sim 2.3\,^{\circ}\mathrm{C}$), depletion of DNA molecules due to the thermophoresis effect has been achieved. Later, Duhr and Braun [42] combined the thermophoresis effect with a pressure driven counter flow to increase the local concentration of DNA molecules with the amount of 16-folds in 15 minutes. In a recent work, Weinert and Braun [122] resolved the slow concentration enrichment issue of the previous systems by introducing an optical conveyer for molecules. They combined the thermophoretic drift and bidirectional flow to achieve 100-fold increase in the DNA molecule concentration within 10 seconds.

Laser-mediated heating systems is also used for on-the fly flow regulation in microfluidic devices and MEMS [67, 123]. Shirasaki et al. [123] developed a valving method for on-chip cell sorting by using a thermo-responsive hydrogel (a polymeric gel that undergoes phase change due to the variation of temperature) as a working solution. They achieved rapid valving (valving times ~ 120 ms) by using an IR laser beam with the power of ~ 615 mW to directly heat the gel solution. To reduce the power consumption and the total cost of the system, Kirshnan and coworkers [67] presented a new design by using a PDMS based microchip mounted on a glass slide, which is coated with a light absorbing material on one side. Relatively fast valving times (valving times ~ 1 s) were achieved by using a low power laser beam (40 mW). They [67] studied the IR absorbance of different materials and showed that ITO serves as a better light absorbing material when compared to gold and glass.

Digital projection-based

Laser-based heating approaches have been shown to be very attractive. However, accurate positioning of the laser beam, especially for small channel dimensions is a main challenge that may affect the feasibility of these methods for microfluidic systems. This becomes a critical issue when multiplex analysis is concerned. To overcome this limitation, digitized projection heating methods have been recently used by several authors [68, 154, 155]. Digital projection systems and digital micromirror arrays offer excellent spatial control of

light distribution using relatively inexpensive, commercially available components. In this method, a projector is used to project the heater pattern onto the surface of a microfluidic assembly. The projector light is absorbed on the surface of a light absorbing material and is converted into heat to provide the desired temperature profile. Present method has unique advantages over other contactless techniques:

1. *flexibility*, which enables the generation of reconfigurable virtual heaters with on-the-fly control of their location, size, and the amount of heat that enters into the heated area;

2. *simplicity*, a commercial video projector equipped with several optics can provide the required heating pattern; moreover, no complex fabrication process or controlling system is required for multiplexing.

This approach has been utilized in applications such as valving and actuation [154, 155] and analyte preconcentration and manipulation [68]. Hua et al. [154] presented an optically microactuator array, called microfluidic *flash memory*, by using a commercial video projector and individual phase-change wax based actuators. In another work, Richter and Paschew [155] used a similar approach to develop a highly integrated polymer based microelectromechanical system (MEMS) with application in artificial skin. They utilized a thermoresponsive polymeric gel as an actuating material. The volume of such material can reversibly change by more than 90% swelling or shrinking in certain temperatures [155]; thus the valving/actuation can be achieved by changing the local temperature of the polymeric gel. In a recent work, Akbari et al. [68] used a commercial video projector and introduced an optothermal analyte preconcentration and manipulation technique via temperature gradient focusing (TGF). By projecting the heater image onto the surface of a light absorbing material, the required temperature distribution for the preconcentration was obtained. They successfully demonstrated the ability of their system to increase the local concentration of sample analytes and transportation of the focused bands along a microcapillary by adjusting the heater image in an external computer.

Despite several advantages associated with this promising heating approach, yet there are some drawbacks that may affect the efficiency of this approach in the present format: (1) the method is not optimized in terms of energy consumption, thus the heating system

is bulky and expensive; (2) the light intensity provided by the video projector is high; this may interfere with the fluorescence microscopy and causes some problems such as rapid photobleaching of the dye and the increasing of the background noise.

Hot/cold air-based

Application of hot-air based heating methods in microfluidics was first reported by Wittwer et al. [125] for PCR thermocycling. They performed the required temperature cycling by rapid switching between the air streams at desired temperatures. The method improved later by several researchers such as Swerdlow et al. [126], Zhang et al. [127], Wang et al. [128] and Lee et al. [129] to increase the heating and cooling rates as well as the efficiency of the system. Air thermocyclers (ATC) are now commercially available for DNA amplification [130]. High-velocity air jets are used at different temperatures to achieve rapid heating and cooling rates. Temperature transition rates of 5 to 10°C/s can be obtained in a typical ATC [130]. Primary advantage of the hot/cold air-based methods is their ability to provide both heating and cooling in a single unit. However, the application of this method is limited to DNA amplification and it has not been implemented in other microfluidic applications. It may be due to the fact that the local temperature control in an integrated microchip cannot be easily accomplished without impacting other components. Moreover, producing localized heating requires compressed air, micronozzles and external heating/cooling elements, which adds to the complexity of the system and hinders its portability.

Microwave-based

Microwave electric fields have attracted much attention for a number of on-chip heating applications. Main characteristics of a microwave-based heating system are:

1. rapid heating rates that can be obtained due to *in situ* heating induced by the microwave;

2. spatially selective heating by confining the electromagnetic fields to specific regions in the microfluidic network, which reduces the heating effect on other components of an integrated microfluidic device;

3. heat can be delivered using signal frequency in addition to power by exploiting the dielectric properties of the fluid.

Main application of this approach is in the DNA amplification [131–134]. The first microwave-based PCR was realized in 2003 by Fermér et al. [131]. They used a single-mode microwave cavity to heat a PCR mixture in a pipet tube in 60 minutes for 25 cycles. Later, Orrling et al. [132] presented a microwave-based heating system capable of performing PCR in a 15 ml reaction chamber for increased sample processing. An air-jet system was utilized to achieve the required cooling rates. In another work, Kempitiya and coworkers [133] proposed a microwave-based PCR system for parallel DNA amplification platforms. With the power of less than 400 mW, they showed that their system can provide heating and cooling rates of $\sim 6-7^{\circ}$C/s. In a recent work, Shaw et al. [134] demonstrated an ultra-fast microwave-based PCR microchip. In order to achieve fast cooling rates, their system was equipped with an air impingement element. The heating and cooling rates up to 65 $^{\circ}$C/s was reported in their work. It should be noted that, all above-mentioned PCR systems were based on the stationary platform. No study was found for the application of microwave heating method in flow-through PCR systems.

Aside from the DNA amplification, microwave technology has become very important in synthesis and it is reasonable to assert that there are now very few areas of synthetic organic chemistry that have not been shown to be enhanced using microwave heating [135]. It has become recognized that many chemical reactions, which require heating are likely to proceed more rapidly using this different form of heating [135]. A comprehensive review on the microwave enhanced synthesis is presented in a recent paper by Caddick and Fitzmaurice [135]. Moreover, Gerbec and coworkers [136] reported a microwave-based method for nanoparticle synthesis. With application in proteomic analysis and cell lysis, Lin et al. [137] proposed a novel microwave-assisted protein digestion method by using magnetic nanoparticles as excellent microwave irradiation absorber. They showed that the efficiency of protein digestion was greatly improved by this approach [137]. Shah and coworkers [141] integrated a thin film microwave transmission line in a microfluidic device to heat fluids with relevant buffer salt concentrations over a wide range of frequencies. The application of such a microchip is for cell lysis, in which maintaining fluid temperature in the vicinity of 94 $^{\circ}$C is necessary [142]. Ramos et al. [138] used AC electric fields at microwave frequencies for electrothermal actuation of water. They argued that there

are two mechanisms for the induced flow: (i) natural convection and (ii) electrothermally induced motion that are resulted from the induced localized heating in the bulk of water solutions due to the microwave fields. The importance of each mechanism is discussed in a numerical study performed by the same authors [139]. Issadore et al. [140] proposed a microwave-based approach that selectively heats water droplets in a two phase water-oil medium. The method is based on the fact that water absorbs microwave power more efficiently than polymers, glass, and oils because of its permanent molecular dipole moment that has large dielectric loss at GHz frequencies. Since each droplet is thermally isolated, ultra-fast heating ramps of 2 °C/ms can be obtained [140].

Induction-based

Addressing the issues of previous heating methods such as laborious fabrication steps, need for accurate positioning of the sample with respect to the heater, accurate configuration of lenses and filters, positioning of the reaction chamber at the appropriate focal length of the optical system, and portability restrictions; the induction-based heating methods have been used in some papers [149–153]. The fundamental concept of induction heating is similar to that for transformers. A magnetic field in an external coil induces current in a heating element, which is fixed in the microfluidic device.

Using induction heating has the following benefits [149]:

- simple fabrication steps,
- relatively fast heating rates, ~ 6.5°C/s,
- simple controlling system.

Induction-base heating was first used in a microfluidic format for PCR application [149]. Pal and Venkataraman [149] developed a microchip thermocycler for DNA amplification. A microchamber was fabricated from silicon and Pyrex and mounted on a metallic heating element. Heating and cooling rates of 6.5 °C/s and 4.2 °C/s was obtained, respectively,with low power consumption ($\sim$ 1.4 W) and free convection cooling. In a recent study, Kim and coworkers [150] developed an induction-base microheater system by embedding magnetic nanoparticles into PDMS (MNP-PDMS). A high-frequency AC magnetic field generator was utilized to induce the required heat. The temperature control was

achieved by changing the contents of the magnetic particle and the intensity of the magnetic field. PCR analysis was implemented by this method and heating rates up to 4°C/s were obtained. This heating rate highly depends on the magnetic nanoparticle contents.

Baek et al. [151] devised a wireless induction heating system in a microfluidic device with application for cell lysis. They prepared the heating units from different metallic films including copper, iron, and nickel. Effects of design parameters such as the heating material, geometry of the heater, and the magnetic field were studied in their work. They [151] showed that nickel is the most suitable material for a heating unit because it provides a faster thermal response.

In addition to above-mentioned applications, induction-based heating has been utilized for microchip thermal bonding [152, 153]. Chen and coworkers [152] used the induction heating method and combined it with water cooling to achieve rapid mold surface temperature control during the micro-feature injection molding process. Later, Knauf et al. [153] developed a cost-effective, rapid production method for polymer microfluidic device sealing based on low frequency induction heating.

Induction-based systems have few difficulties to be resolved:

- The distance between the windings should be kept as small as possible and the work piece should be as close as feasible to the coil to assure maximum energy transfer. As the magnetic center of the inductor is not necessarily its geometric center the work piece should be rotated to gain more homogeneous heat distribution [153]. This adds more restriction to the system and increases the complexity of the design and appropriate configuration of connecting tubes and/or other parts.

- In applications where optical transparency is required, metallic heaters and the magnetic coils limit field of view.

- The coil must be designed such that the cancellation of the magnetic field is avoided. The cancellation occurs when two windings running in opposite directions are too close to each other.

2.2.3 Miscellaneous methods

A detailed discussion about the available contact and contactless heating methods for microfluidic applications is presented above. There are other heating methods used in the literature that cannot be categorized in any of the above-mentioned groups. Therefore, we summarized them as a separate group called "miscellaneous methods". Two different approaches can be recognized in this class of heating method:

1. buffer Joule heating-based
2. chemical/physical process-based

Table 2.5 gives an overview of the miscellaneous heating methods. Detailed discussion about these methods are presented in the following section.

Buffer Joule heating-based

The Joule heating caused by the current flow through the buffer solution can lead to significant increases in the buffer temperature [156]. Since no thermal mass is added to the system for heating, this method can lead to relatively fast heating rates; the maximum reported heating rate in the literature is 15°C/s [159]. Stern and coworkers [159] developed a continuous-flow microfluidic PCR device by using the alternative current (AC) induced joule heating methods. They transferred the electric current directly into the PCR solution and obtained rapid heating and cooling rates of 15°C/s. In-channel Pt electrodes were utilized to transfer the AC heating current into the buffer under the conditions of minimal oxidation reduction and water electrolysis. In another work, Hu et al. [158] developed a two-temperature thermal cycling microfluidic PCR device based on direct current (DC) induced joule heating effect in a single channel. With this method, heating and cooling rates of 3°C/s and 2°C/s were obtained, respectively. The two-temperature PCR thermal cycling was achieved by electrokinetically pumping the PCR reaction solution through the microchannel forwards and backwards. To control the temperature of each cycle, they [158] changed the applied electrical current periodically between high and low values by programming the high voltage power supply. DeMello and coworkers [157] developed a microfluidic devices for spatially localized heating of microchannel environments based

Table 2.5: Summary of miscellaneous heating methods for microfluidic applications.

method	applications	comments
buffer Joule heating-based	-proof-of-concept -preconcentration and separation -DNA amplification	• no additional thermal mass to the system for heating, thus relatively fast thermal responses can be achieved • low power consumption • thermal run away and bubble formation is a potential challenge • only works with solutions with high ionic strengths
chemical/physical process-based	-proof-of-concept	• no tunable temperature is achievable • no need of external components for heating and cooling • smaller footprints are possible • no power consumption • thermal effect is sensitive to the ambient temperature • highly depends on the mixing efficiency of the reactor

on AC induced Joule heating effect in co-running channels. With this configuration, they [157] demonstrated a temperature control with the accuracy of $\pm 0.2^{\circ}$C in their system.

Joule-heating based method has also been used for preconcentration and separation of analytes in various studies [38, 52, 60]. The first demonstration of Joule-heating based TGF preconcentration was performed by Ross and Locascio [38]. They showed that the local concentration charged samples increased close to the junction of a sudden expansion. In another work, Kim et al. [52] designed a converging-diverging microchannel, and demonstrated that when a high voltage DC was applied, preconcentration and separation of charged molecules occurred at location close to the throat of the channel. Preconcentration and separation of analytes with this configuration is shown to be simple, cost effective, and efficient in terms of power consumption [52]. In a recent study, Ge et al. [60] performed both experimental and numerical investigation of TGF-based preconcentration in a sudden expansion.

Key features of Joule-heating based methods are: low thermal mass, simplicity in terms of fabrication and controlling, low cost and power consumption, and fast thermal response. On the other hand, there are several substantial drawbacks involved in the systems using the Joule-heating effect:

• the system works for solutions with high ionic strength, Joule heating becomes insignificant for low ionic strengths solutions due to smaller electrical conductivities;

• electrical conductivity of solutions is highly temperature dependent, thus as conductivity increases at higher temperatures, more Joule heating is induced which leads to the uncontrollable temperature rise in the system which is usually referred to as the *thermal runaway*;

• bubble formation due the electrolysis of the aqueous solutions at the electrodes when high voltages are applied are usually problematic.

Chemical/physical reaction-based

Chemical/physical reaction-based methods are not only used for heating purposes, but also can be used for cooling applications. These methods based on the exploitation of endothermic or exothermic processes in microchannels to respectively cool or heat solutions in an adjacent microchannel. The extent of the thermal effect can be controlled by either the flow ratio of the two components, or by selection of the components based on their chemical or

physical properties[160]. Major advantage of such a system is its ability to generate the required temperatures (even below the ambient temperature) without using any external heat exchanger, fan, Peltier module, or complex fabrication steps. These benefits eventually lead to the decrease of the device footprint, improve the possibility of integration and portability, and lower the total cost of the system. To the author's best knowledge, the first chemical-reaction based temperature control method was introduced by Guijt et al. [160] for a proof-of-concept for DNA amplification analysis. They used vacuum as the driving force to control the flow ratio of two chemical components which were mixed to produce the appropriate temperature. In another study, Maltezos and coworkers [161] used evaporation process to provide a novel cooling method for microfluidic applications. They demonstrated an ultra-fast cooling rate of 40°C/s under optimal condition. One major drawback associated with the chemical/physical process-based method is that tunable temperature control cannot be easily achieved. Moreover, the amount of heating and cooling depends on the ambient temperature and the mixing efficiency of the reactor.

2.3 Fluid flow in microchannels of general cross-section

The concept of flow through microchannels of arbitrary cross-sections forms the basis of a class of problems in microfluidics which has applications in micromixer design [162–166], accelerated particle electrophoresis [167, 168], heat transfer augmentation in micro heat sinks [169–172], flow through porous media [173–177], blood flow in the context of biomechanics [178], preconcentration and separation of molecules [38, 52], and polymer processing [179, 180].

As a result of recent advances in microfabrication techniques, microchannels with different cross sectional geometries are fabricated for both commercial and scientific purposes. For instance, microchannels produced directly by techniques such as chemical etching on silicon wafers have a trapezoidal cross-section [181] while using the soft lithography [182] or CO_2 laser ablation methods lead to nearly rectangular or triangular cross-sections, respectively [167, 168, 180, 183–185] .

As a result of this trend, a large number of studies have focused on flow and pressure drop investigations in straight and variable cross-section microchannels with a range of cross-sectional geometries. Table 2.6 lists some examples of previous experimental and

numerical studies on the laminar flow and pressure drop in microchannels with uniform and/or variable cross-sections. Most of these studies show that the traditional theory for fluid flow in macroscale is applicable in the microscale for liquid flow. For gas flows, however, when the channel length scale becomes comparable with the mean free path of the flowing gas (i.e., for high Knudsen numbers), no-slip boundary condition is no longer valid at the wall or in the extreme case higher order conservation equations should be used instead of the regular Navier-stokes equations [203]. For a comprehensive review of the literature on single phase flow in micro scales, the reader is referred to the papers of Papautsky et al. [200], Steinke and Kandlikar [201], and Hrnjak et al. [202]. The reader is referred to read ref. [204] for a comprehensive study on the flow in ducts with different cross-sectional shapes.

In the context of analytical modeling and finding exact solutions for fluid flow in straight channels with different cross-sectional geometries, few analytical studies have been performed for straight microchannels [205–207]. Yovanovich and Muzychka [205] showed that if the square root of cross-sectional area is used in the definition of the Poiseuille number, more consistent results can be obtained for various geometries. Sisavath et al. [208] made an assessment of hydraulic radius, Saint-Venant, and Aissen's approximations to determine the hydraulic resistance of laminar fully developed flow in straight channels with irregular shapes. Comparing the proposed approximations with the available exact solutions, they showed that Saint-Venant, and Aissen's approximations are within 15can be in error by as much as 50bahrami2007novel introduced a general analytical model for the prediction of the Poiseuille number based on the square root of cross-sectional area in laminar fully developed flow along a straight microchannel of arbitrary cross-section. Using a "bottom-up" approach, they [206] showed that for constant fluid properties and flow rate in fixed cross-section channels, the Poiseuille number is only a function of geometrical parameters of the cross-section, i.e., cross-sectional perimeter, area, and polar moment of inertia. Their model was successfully validated against the numerical and experimental data for a wide variety of geometries including: hyperelliptical, trapezoidal, sinusoidal, square duct with two adjacent round corners, rhombic, circular sector, circular segment, annular sector, rectangular with semi-circular ends, and moon-shaped channels [185, 206]. In a recent paper, Bahrami et al. [207] extended their general model to slip flow condition in a straight channel of arbitrary cross-section. Their model is shown to predict the numerical

Table 2.6: Examples of previous numerical and experimental studies on the laminar flow pressure drop in microchannels of straight and variable cross-sections.

Author(s)	year	channel geometry	$D_h[\mu m]$	Reynolds number range	comments
Chow & Soda [186]	1972	Circ.	–	< 25	numerical study
Tuckerman & Pease [169]	1981	Rect.	86 – 95	–	experimental study
Sparrow & Prata [170]	1983	Circ.	–	< 100	numerical and experimental study channels with linear wall
Pfahler et al. [187]	1990	Rect.	1.6 – 76	–	experimental study
Hemmat & Borhan [188]	1995	Circ.	–	creeping flow	numerical study channels with linear wall
Qu et al. [189]	2000	Trap.	51 – 169	6 – 1447	numerical and experimental study channels with linear wall
Xu et al. [190]	2000	Rect.	30 – 344	5 – 4620	experimental study straight channel
Zhang et al. [191]	2002	Rect.	25 – 60	–	experimental study straight channel
Judy et al. [192]	2002	Rect./Circ.	14 – 149	7.6 – 2251	experimental study straight channel
Li [193]	2003	Circ.	80 – 205	300 – 2500	experimental study straight channel
Wu and Cheng [194]	2003	Trap./Triang.	26 – 291	11.1 – 3060	experimental study straight channel
Liu and Garimella [195]	2004	Rect.	244 – 974	230 – 6500	experimental study straight channel
Hsieh et al. [196]	2004	Rect.	146	< 1000	experimental study straight channel
Baviere et al.[197]	2005	Rect.	4.5 – 21	0.1 – 300	experimental study straight channel
Oliveira et al. [180]	2007	Rect.	82 – 153	3.21	numerical and experimental study hyperbolic contraction
Akbari et al.[185]	2009	Rect.	116 – 192	1 – 40	experimental study straight channel
Akbari et al.[198]	2010	Circ.	-	< 100	numerical study sinusoidal and linear walls
Akbari et al. [199]	2011	Rect.	66 – 140	10 – 70	experimental study variable cross-section channel with linear wall

and experimental results obtained from the literature with good accuracy.

A simple model to approximate the flow in a variable cross-section microchannel is to assume that the fluid flow at each axial location along the channel resembles the fully developed flow that would exist at that location if the channel shape did not vary with axial direction; this is usually referred to as the *lubrication approximation* [198, 209]. The overall pressure drop is then calculated by integrating the local pressure gradient over the total length of the channel. Although good results can be obtained for creeping flow in mildly constricted channels, this method is not accurate when the inertia effects become important or the amplitude of the constriction is substantial [210]. To obtain more accurate solutions, *asymptotic series solution* has been used by several authors for sinusoidal tubes [178, 186, 210–212] and two-dimensional channels with sinusoidal walls [213]. In this method, the solution of the Navier-Stokes equations is obtained by expanding the flow variables in powers of a small parameter characterizing the slowly varying character of the bounding walls; usually referred as *perturbation parameter*. Although the asymptotic solution method gives more accurate results compared to the lubrication approximation, the final solution for pressure drop and velocity field has a complex form even for simple cross-sectional geometries such as parallel plates or circular tubes.

Numerical and experimental methods are also used to investigate the laminar flow along slowly varying cross-section channels. Deiber and Schowalter [214] performed a numerical study on the creeping flow through tubes with sinusoidal axial variations in diameter by using finite difference technique. The pressure drop results were then compared with those measured through an independent experimentation. Borhan and Hemmat [188] used the boundary integral method to solve the Navier-stokes equations under the condition of creeping flow for axisymmetric capillary tubes whose diameter varies sinusoidally in the axial direction. Detailed velocity and pressure distributions within the capillary were obtained and the critical values of the geometrical parameters leading to flow reversal were reported.

Finding analytical solutions for many practical cross-sections such as rectangle or trapezoid even for straight channels is complex and/or impossible. There are few works in the literature which are dealing with the hydrodynamics of laminar flow in slowly-varying channels of non-circular cross-section [163, 215, 216]. Lauga et al. [163] used the perturbation theory for creeping flow in channels constrained geometrically to remain between

two parallel planes. Up to the first order accuracy of the perturbation solution, they showed that the velocity components perpendicular to the constraint plane cannot be zero unless the channel has both constant curvature and constant cross-sectional width. They only reported the zeroth order of the pressure gradient, which is identical to the lubrication approximation and only accounts for frictional effects. In another work, Gat et al. [216] studied the laminar incompressible gas flow through narrow channels with a variable cross-section using a higher order Hele-Shaw approximation [217]. Their method shows improvement over the classical Hele-Shaw solution [217]; however, it does not account for the inertia effects that usually occurs in contractions or expansions. Wild et al. [215] used the perturbation theory to calculate the velocity and pressure distribution in an elliptical tube whose cross-sectional area varies slowly with a given profile along the axial direction. They [215] showed that the velocity distribution has a complicated form even up to the first order accuracy, but the local pressure gradient remains only a function of axial direction.

Bibliography

[1] A. Manz, N. Graber, H. Widmer, Miniaturized total chemical analysis systems: a novel concept for chemical sensing, Sensors and actuators B: Chemical 1 (1-6) (1990) 244–248.

[2] M. Tokeshi, T. Minagawa, T. Kitamori, Integration of a microextraction system: Solvent extraction of a Co-2-nitroso-5-dimethylaminophenol complex on a microchip, Journal of Chromatography A 894 (1-2) (2000) 19–23.

[3] K. Sato, M. Yamanaka, H. Takahashi, M. Tokeshi, H. Kimura, T. Kitamori, Microchip-based immunoassay system with branching multichannels for simultaneous determination of interferon−3b3, Electrophoresis 23 (5) (2002) 734–739.

[4] S. Ohira, K. Toda, S. Ikebe, P. Dasgupta, Hybrid microfabricated device for field measurement of atmospheric sulfur dioxide, Anal. Chem. 74 (22) (2002) 5890–5896.

[5] E. Tamaki, K. Sato, M. Tokeshi, K. Sato, M. Aihara, T. Kitamori, Single-cell analysis by a scanning thermal lens microscope with a microchip: Direct monitoring of cytochrome C distribution during apoptosis process, Anal. Chem. 74 (7) (2002) 1560–1564.

[6] A. Manz, D. Harrison, E. Verpoorte, and J. Fettinger, Planar chips technology for miniaturization and integration of separation techniques into monitoring systems:: Capillary electrophoresis on a chip, Journal of Chromatography A 593 (1-2) (1992) 253–258.

[7] K. Sueyoshi, F. Kitagawa, K. Otsuka, Recent progress of online sample preconcen-

tration techniques in microchip electrophoresis, Journal of separation science 31 (14) (2008) 2650–2666.

[8] S. Jacobson, J. Ramsey, Microchip electrophoresis with sample stacking, Electrophoresis 16 (1) (1995) 481–486.

[9] J. Lichtenberg, E. Verpoorte, N. de Rooij, Sample preconcentration by field amplification stacking for microchip-based capillary electrophoresis, Electrophoresis 22 (2) (2001) 258–271.

[10] N. Beard, C. Zhang, et al., In-column field-amplified sample stacking of biogenic amines on microfabricated electrophoresis devices, Electrophoresis 24 (4) (2003) 732–739.

[11] M. Gong, K.Wehmeyer, P. Limbach, F. Arias, W. Heineman, On-line sample preconcentration using field-amplified stacking injection in microchip capillary electrophoresis, Anal. Chem. 78 (11) (2006) 3730–3737.

[12] L. Zhang, X. Yin, Field amplified sample stacking coupled with chip-based capillary electrophoresis using negative pressure sample injection technique, Journal of Chromatography A 1137 (2) (2006) 243–248.

[13] J. Palmer, D. Burgi, N. Munro, J. Landers, Electrokinetic injection for stacking neutral analytes in capillary and microchip electrophoresis, Anal. Chem. 73 (4) (2001) 725–731.

[14] H. Yang, R. Chien, Sample stacking in laboratory-on-a-chip devices, Journal of Chromatography A 924 (1-2) (2001) 155–163.

[15] D. Kim, S. Kang, On-channel base stacking in microchip capillary gel electrophoresis for highsensitivity DNA fragment analysis, Journal of Chromatography A 1064 (1) (2005) 121–127.

[16] Y. Zhang, G. Ping, B. Zhu, N. Kaji, M. Tokeshi, Y. Baba, Enhanced electrophoretic resolution of monosulfate glycosaminoglycan disaccharide isomers on poly (methyl methacrylate) chips, Electrophoresis 28 (3) (2007) 414–421.

[17] B. Jung, R. Bharadwaj, J. Santiago, Thousandfold signal increase using field-amplified sample stacking for on-chip electrophoresis, Electrophoresis 24 (19-20) (2003) 3476–3483.

[18] P. Walker III, M. Morris, M. Burns, B. Johnson, Isotachophoretic separations on a microchip. Normal Raman spectroscopy detection, Anal. Chem. 70 (18) (1998) 3766–3769.

[19] D. Kaniansky, M. Masar, J. Bielcvikov´a, F. Ivanyi, F. Eisenbeiss, B. Stanislawski, B. Grass, A. Neyer, M. J ohnck, Capillary electrophoresis separations on a planar chip with the column-coupling configuration of the separation channels, Anal. Chem. 72 (15) (2000) 3596–3604.

[20] B. Graß, R. Hergenroder, A. Neyer, D. Siepe, Determination of selenoamino acids by coupling of isotachophoresis/capillary zone electrophoresis on a PMMA microchip, Journal of Separation Science 25 (3) (2002) 135–140.

[21] H. Huang, F. Xu, Z. Dai, B. Lin, On-line isotachophoretic preconcentration and gel electrophoretic separation of sodium dodecyl sulfate-proteins on a microchip, Electrophoresis 26 (11) (2005) 2254–2260.

[22] B. Ma, X. Zhou, G. Wang, H. Huang, Z. Dai, J. Qin, B. Lin, Integrated isotachophoretic preconcentration with zone electrophoresis separation on a quartz microchip for UV detection of flavonoids, Electrophoresis 27 (24) (2006) 4904–4909.

[23] S. Bahga, M. Bercovici, J. Santiago, Ionic strength effects on electrophoretic focusing and separations, Electrophoresis 31 (5) (2010) 910–919.

[24] J. Quirino, S. Terabe, Exceeding 5000-fold concentration of dilute analytes in micellar electrokinetic chromatography, Science 282 (5388) (1998) 465-468.

[25] Y. Sera, N. Matsubara, K. Otsuka, S. Terabe, Sweeping on a microchip: Concentration profiles of the focused zone in micellar electrokinetic chromatography, Electrophoresis 22 (16) (2001) 3509–3513.

[26] Y. Liu, R. Foote, S. Jacobson, J. Ramsey, Stacking due to ionic transport number mismatch during sample sweeping on microchips, Lab on a Chip 5 (4) (2005) 457–465.

[27] C. Chen, S. Yen, H. Makamba, C. Li, M. Tsai, S. Chen, Semihydrodynamic injection for high salt stacking and sweeping on microchip electrophoresis and its application for the analysis of Estrogen and Estrogen Binding, Anal. Chem. 79 (1) (2007) 195–201.

[28] M. Gong, K. Wehmeyer, P. Limbach, W. Heineman, Flow manipulation for sweeping with a cationic surfactant in microchip capillary electrophoresis, Journal of Chromatography A 1167 (2) (2007) 217–224.

[29] J. Quirino, S. Terabe, Approaching a million-fold sensitivity increase in capillary electrophoresis with direct ultraviolet detection: cation-selective exhaustive injection and sweeping, Anal. Chem. 72 (5) (2000) 1023–1030.

[30] F. Kitagawa, T. Tsuneka, Y. Akimoto, K. Sueyoshi, K. Uchiyama, A. Hattori, K. Otsuka, Toward million-fold sensitivity enhancement by sweeping in capillary electrophoresis combined with thermal lens microscopic detection using an interface chip, Journal of Chromatography A 1106 (1-2) (2006) 36–42.

[31] H. Lin, J. Shackman, D. Ross, Finite sample effect in temperature gradient focusing, Lab on a Chip 8 (6) (2008) 969–978.

[32] P. Righetti, A. Bossi, Isoelectric focusing of proteins and peptides in gel slabs and in capillaries, Analytica Chimica Acta 372 (1-2) (1998) 1–19.

[33] O. Hofmann, D. Che, K. Cruickshank, U. M Muller, Adaptation of capillary isoelectric focusing to microchannels on a glass chip, Anal. Chem. 71 (3) (1999) 678–686.

[34] F. Raisi, P. Belgrader, D. Borkholder, A. Herr, G. Kintz, F. Pourhamadi, M. Taylor, M. Northrup, Microchip isoelectric focusing using a miniature scanning detection system, Electrophoresis 22 (11) (2001) 2291–2295.

[35] J. Sanders, Z. Huang, J. Landers, Acousto-optical deflection-based whole channel scanning for microchip isoelectric focusing with laser-induced fluorescence detection, Lab on a Chip 1 (2) (2001) 167–172.

[36] H. Cui, K. Horiuchi, P. Dutta, C. Ivory, Isoelectric focusing in a poly (dimethylsiloxane) microfluidic chip, Anal. Chem 77 (5) (2005) 1303–1309.

[37] J. Han, A. Singh, Rapid protein separations in ultra-short microchannels: microchip sodium dodecyl sulfate-polyacrylamide gel electrophoresis and isoelectric focusing, Journal of Chromatography A 1049 (1-2) (2004) 205–209.

[38] D. Ross, L. Locascio, Microfluidic temperature gradient focusing, Anal. Chem. 74 (11) (2002) 2556–2564.

[39] W. Koegler, C. Ivory, Field gradient focusing: a novel method for protein separation, Biotechnology Progress 12 (6) (1996) 822–836.

[40] W. Koegler, C. Ivory, Focusing proteins in an electric field gradient, Journal of Chromatography A 726 (1-2) (1996) 229–236.

[41] I. Goldhirsch, D. Ronis, Theory of thermophoresis. I. General considerations and modecoupling analysis, Physical Review A 27 (3) (1983) 1616–1634.

[42] S. Duhr, D. Braun, Optothermal molecule trapping by opposing fluid flow with thermophoretic drift, Physical review letters 97 (3) (2006) 38103.

[43] J. Shackman, M. Munson, D. Ross, Temperature gradient focusing for microchannel separations, Analytical and Bioanalytical Chemistry 387 (1) (2007) 155–158.

[44] K. Balss, W. Vreeland, P. Howell, A. Henry, D. Ross, Micellar affinity gradient focusing: a new method for electrokinetic focusing, J. Am. Chem. Soc 126 (7) (2004) 1936–1937.

[45] K. Balss, W. Vreeland, K. Phinney, D. Ross, Simultaneous concentration and separation of enantiomers with chiral temperature gradient focusing, Anal. Chem 76 (24) (2004) 7243–7249.

[46] J. Shackman, M. Munson, C. Kan, D. Ross, Quantitative temperature gradient focusing performed using background electrolytes at various pH values, Electrophoresis 27 (17) (2006) 3420–3427.

[47] S. Hoebel, K. Balss, B. Jones, C. Malliaris, M. Munson, W. Vreeland, D. Ross, Scanning temperature gradient focusing, Anal. Chem 78 (20) (2006) 7186–7190.

[48] M. Kamande, D. Ross, L. Locascio, M. Lowry, I. Warner, Simultaneous concentration and separation of coumarins using a molecular micelle in micellar affinity gradient focusing, Anal. Chem. 79 (5) (2007) 1791–1796.

[49] M. Munson, G. Danger, J. Shackman, D. Ross, Temperature gradient focusing with field amplified continuous sample injection for dual-stage analyte enrichment and separation, Anal. Chem. 79 (16) (2007) 6201–6207.

[50] K. Balss, D. Ross, H. Begley, K. Olsen, M. Tarlov, DNA hybridization assays using temperature gradient focusing and peptide nucleic acids, J. Am. Chem. Soc 126 (41) (2004) 13474–13479.

[51] M. Munson, J. Meacham, L. Locascio, D. Ross, Counterflow rejection of adsorbing proteins for characterization of biomolecular interactions by temperature gradient focusing, Anal. Chem. 80 (1) (2008) 172–178.

[52] S. Kim, G. Sommer, M. Burns, E. Hasselbrink, Low-power concentration and separation using temperature gradient focusing via Joule heating, Anal. Chem 78 (23) (2006) 8028–8035.

[53] G. Sommer, S. Kim, R. Littrell, E. Hasselbrink, Theoretical and numerical analysis of temperature gradient focusing via Joule heating, Lab on a Chip 7 (7) (2007) 898–907.

[54] M. Becker, A. Mansouri, C. Beilein, D. Janasek, Temperature gradient focusing in miniaturized free-flow electrophoresis devices, Electrophoresis 30 (24) (2009) 4206–4212.

[55] T. Matsui, J. Franzke, A. Manz, D. Janasek, Temperature gradient focusing in a PDMS/glass hybrid microfluidic chip, Electrophoresis 28 (24) (2007) 4606–4611.

[56] S. Ghosal, J. Horek, Mathematical model describing gradient focusing methods for trace analytes, Anal. Chem. 77 (16) (2005) 5380–5384.

[57] D. Huber, J. Santiago, Taylor-Aris dispersion in temperature gradient focusing, Electrophoresis 28 (14) (2007) 2333–2344.

[58] D. Huber, J. Santiago, Ballistic dispersion in temperature gradient focusing, in: Proc. R. Soc. A 464 (2008) 595–612.

[59] G. Tang, C. Yang, Numerical modeling of Joule heating-induced temperature gradient focusing in microfluidic channels, Electrophoresis 29 (5) (2008) 1006–1012.

[60] Z. Ge, C. Yang, G. Tang, Concentration enhancement of sample solutes in a sudden expansion microchannel with Joule heating, International Journal of Heat and Mass Transfer 53 (13-14) (2010) 2722–2731.

[61] P. Watts, An Chemical synthesis in micro reactors, Chemie Ingenieur Technik 76 (2004) 555–559.

[62] T. Pennel , T. Suchyna ,J. Wang,J. Heo, J. Felske, F. Sachs, and S. Hau, Microfluidic microchip to produce temperature jumps for electrophysiology, Anal. Chem. 80 (2008) 2447-2451.

[63] E.M. Chan, A.P. Alivisatos, and R.A. Mathies, High-temperature microfluidic synthesis of CdSe nanocrystals in nanoliter droplets, JACS 127(40) (2005) 13854–13861.

[64] C. Zhang, J. Xu,W. Ma, and W. Zheng, PCR microfluidic devices for DNA amplification, Biotechnology Advances 24 (2006) 243-284.

[65] B. Stoeber, Z. Yang, D. Liepmann, and S.J. Muller, Passive flow control in microdevices using thermally responsive polymer solutions, Physics of Fluids 18 (2006) 053103.

[66] S. Duhr and D. Braun, Why molecules move along a temperature gradient, PNAS 103(52) (2006) 19678-19682.

[67] M. Krishnan, J. Oark, and D. Erickson, Optothermorheological flow manipulation, Optics Letters 34 (13) (2009) 1976-1978.

[68] M. Akbari, M. Bahrami, and D. Sinton, Optothermal analyte manipulation with temperature gradient focusing, Proceeding of IMECE2011 paper no. IMECE2010-30412 (2010).

[69] H. Yang, C.A. Choi, K.H. Chung, C.H. Jun, and Y.T. Kim, An independent temperature-controllable microelectrode array. Anal. Chem. 76 (5) (2004) 1537–1543.

[70] A.T. Woolley, D. Hadley, P. Landre, J. Andrew R.A. Mathies, and M.A. Northrup, Functional integration of PCR amplification and capillary electrophoresis in a microfabricated DNA analysis device, Anal. Chem. 68 (1996) 4081–4086.

[71] P. Belgrader, C.J. Elkin, S.B. Brown, S.N. Nasarabadi, R.G. Langlois, F.P. Milanovich, B.W. Colston Jr, and G.D. Marshall, A reusable continuous-flow polymerase chain reaction instrument for the continuous monitoring of infectious biological agents, Anal. Chem. 75 (2003) 3446–3450.

[72] M.A. Burns, C.H. Mastrangelo, T.S. Sammarco, F.P. Man, J.R. Webster, B.N. Johnsons, B. Foerster, D. Jones, et al., Microfabricated structures for integrated DNA analysis, PNAS 93(11) (1996) 5556-5561.

[73] I. Rodriguez, M. Lesaicherre, Y. Tie, Q. Zou, C. Yu, J. Singh, L.T. Meng, S. Uppili, S.F.Y. Li, P. Gopalakrishnakone, et al., Practical integration of polymerase chain reaction amplification and electrophoretic analysis in microfluidic devices for genetic analysis, Electrophoresis 24 (2003) 1522-2683.

[74] K. Sun, A. Yamaguchi, Y. Ishida, S. Matsuo, and H. Misawa, H., A heater-integrated transparent microchannel chip for continuous-flow PCR, Sensors and Actuators B: Chemical 84 (2002) 283–289.

[75] P.J. Lee, P. Sabounchi, N. Aghdam, R. Lin, and L.P. Lee, A novel high aspect ratio microfluidic design to provide a stable and uniform microenvironment for cell growth in a high throughput mammalian cell culture array, Lab on Chip 5 (2005) 44–48.

[76] J.C. Yoo, M.C. Moon, Y.J. Choi, C.J. Kang, and Y.S. Kim, A high performance microfluidic system integrated with the micropump and microvalve on the same substrate, Microelect. Eng. 83 (2006) 1684–1687.

[77] Y.S. Heo, L.M. Cabrera, J.W. Song, N. Futai, Y.C. Tung, G.D. Smith, and S. Takayama, Characterization and resolution of evaporation-mediated osmolality shifts that constrain microfluidic cell culture in poly (dimethylsiloxane) devices, Anal. Chem. 79 (2007) 1126–1134.

[78] J.Y. Cheng, M.H. Yen, C.T. Kuo, and T.H. Young, A transparent cell-culture microchamber with a variably controlled concentration gradient generator and flow field rectifier, Biomicrofluidics 2 (2008) 024105.

[79] J.L. Lin, M.H. Wu, C.Y. Kuo, K.D. Lee, and Y.L. Shen, Application of indium tin oxide (ITO)-based microheater chip with uniform thermal distribution for perfusion cell culture outside a cell incubator, Biomedical microdevices 12(3) (2010) 389–398.

[80] G.V. Kaigala, V.N. Hoang, A. Stickel, J. Lauzon, D. Manage, L.M. Pilarski, and C.J. Backhouse, An inexpensive and portable microchip-based platform for integrated RT–PCR and capillary electrophoresis, Analyst 133 (2008) 331–338.

[81] C.S. Liao, G.B. Lee, J.J.Wu, C.C. Chang, T.M. Hsieh, and F.C. Huang, Micromachined polymerase chain reaction system for multiple DNA amplification of upper respiratory tract infectious diseases, Biosens Bioelectron 20 (2005) 1341–1348.

[82] W. Zheng, and S. Chen, Continuous-flow submicroliter-scale PCR chip for DNA amplification, Proceedings of SPIE (2001) 256-262.

[83] S.Z. Ali, P.K. Guha, C.C.C. Lee, F. Udrea, W.I. Milne, T. Iwaki, J. Covington, and J.W. Gardner, High temperature SQI CMOS tungsten microheaters, Proceesing of 5th IEEE Conference on sensors (2006) 847–850.

[84] N. Shukla, S.K. Tripathi, A. Banerjee, A. Ramana, N.S. Rajput, and V.N. Kulkarni, Study of temperature rise during focused Ga ion beam irradiation using nanothermoprobe, Applied Surface Science 256(2) (2009) 475–479.

[85] C.G. Koh, W. Tan, M. Zhao, A.J. Ricco, and Z.H. Fan, Integrating polymerase chain reaction, valving, and electrophoresis in a plastic device for bacterial detection, Anal. Chem. 75 (2003) 4591–4598.

[86] C.F. Chou, R. Changrani, P. Roberts, D. Sadler, J. Burdon, F. Zenhausern, S. Lin, A. Mulholland, N. Swami, and R. Terbrueggen, A miniaturized cyclic PCR device–modeling and experiments, Microelectronic Engineering 61 (2002) 921–925.

[87] D.J. Sadler, R. Changrani, P. Roberts, C.F. Chou, and F. Zenhausern, Thermal management of BioMEMS: temperature control for ceramic-based PCR and DNA detection devices, IEEE Transactions on Comp. Pack. Tech. 26(2) (2003) 309–316.

[88] S. Poser, T. Schulz, U. Dillner, V. Baier, J.M. Kohler, D. Schimkat, G. Mayer, and A. Siebert, Chip elements for fast thermocycling, Sensors and Actuators A: Physical 62 (1997) 672–675.

[89] S. Mongpraneet, A. Wisitsora-at, T. Kamnerdtong, P. Jongpardist, and A. Tuantranont, Simulation and experiment of PDMS based thermopnuematic microvalve in microfluidic chip, 6th IEEE International Conference on Electrical Engineering/Electronics, Computer, Telecommunications and Information Technology (2009) 458–461.

[90] D. Day, and M. Gu, Nanotechnology 20 (2009) 105601.

[91] P. Belgrader, S. Young, B. Yuan, M. Primeau, L.A. Christel, F. Pourahmadi, and M.A. Northrup, A battery-powered notebook thermal cycler for rapid multiplex real-time PCR analysis, Anal. Chem. 73 (2001) 286–289.

[92] D. Vigolo, R. Rusconi, R. Piazza, and H.A. Stone, A portable device for temperature control along microchannels, Lab on Chip 10 (2010), 795-798.

[93] J. Felbel, I. Bieber, J. Pipper, and J.M. Kohler, Investigations on the compatibility of chemically oxidized silicon (SiOx)-surfaces for applications towards chip-based polymerase chain reaction. Chem. Eng. J. 101 (2004) 333–338.

[94] D.S. Yoon, Y.S. Lee, Y. Lee, H.J. Cho, S.W. Sung, K.W. Oh, et al., Precise temperature control and rapid thermal cycling in a micromachined DNA polymerase chain reaction chip. J Micromech. Microeng. 12 (2002) 813– 823.

[95] J. Wu, W. Cao, W. Wen, D.C. Chang, and P. Sheng, Polydimethylsiloxane microfluidic chip with integrated microheater and thermal sensor, Biomicrofluidics 3 (2009) 012005.

[96] T.M Hsieh, C.H. Luo,J.H. Wang,J.L. Lin, K.Y. Lien, and G.B. Lee, A two-dimensional, self-compensated, microthermal cycler for one-step reverse transcription polymerase chain reaction applications, Microfluidic Nanofluidic 6 (2009) 797–809.

[97] B. Stoeber, Z. Yang, D. Liepmann, and S.J. Muller, Flow control in microdevices using thermally responsive triblock copolymers, J. of Microelectromechanical Systems 14(12) (2005) 207-213.

[98] M. Krishnan, M.T. Tolley, H. Lipson, and D. Erickson, Hydrodynamically tunable affinities for fluidic assembly, Langmuir 25(6) (2009) 3769–3774.

[99] Z. Li, Q. He, D. Ma, H. Chen, and S.A. Soper, Thermoswitchable electrokinetic ion-enrichment/elution based on a Poly (N-isopropylacrylamide) hydrogel plug in a microchannel, Anal. Chem. 82 (2010) 10030–10036.

[100] M.U. Kopp, A.J. de Mello, and A. Manz, Chemical amplification: continuous-flow PCR on a chip, Science 280 (1998)1046 –1048.

[101] Y. Liu, C.B. Rauch, R.L. Stevens, R. Lenigk, J. Yang, B. David, and P. Grodzinski, DNA amplification and hybridization assays in integrated plastic monolithic devices, Anal. Chem. 74 (2002) 3063–3070.

[102] A. Gulliksen, L. Solli, F. Karlsen, H. Rogne, E. Hovig, T. Nordstrøm, et al., Real-time nucleic acid sequence-based amplification in nanoliter volumes, Anal. Chem. 76 (2004) 9–14.

[103] N.C. Cady, S. Stelick, M.V. Kunnavakkam, C.A. Batt, Real-time PCR detection of Listeria monocytogenes using an integrated microfluidics platform, Sens. Actuators B Chem. 107 (2005) 332–341.

[104] N. Crews, C. Wittwer, and B. Gale, Continuous-flow thermal gradient PCR, Biomedical microdevices 10(2) (2008) 187–195.

[105] Y. Zhang, and P. Ozdemir, Microfluidic DNA amplification–A review, Analytica Chimica Acta 638(2) (2009) 115–125.

[106] K.M. Robotti, H. Yin, R. Brennen, L. Trojer, and K. Killeen, Microfluidic HPLC-Chip devices with integral channels containing methylstyrenic-based monolithic media, Journal of Sep. Sci. 32(20) (2009) 3379–3387.

[107] T.J. Pappas,and L.A. Holland, Fluid steering in a microfluidic chip by means of thermally responsive phospholipids, Sensors and Actuators B: Chemical 128(2) (2008) 427–434.

[108] X. Zhou, D. Liu, R. Zhong, Z. Dai, D. Wu, H. Wang, Y. Du, Z. Xia, L. Zhang, X. Mei, et al., Determination of SARS-coronavirus by a microfluidic chip system, Electrophoresis 25(17) (2004) 3032–3039.

[109] R. Fu, B. Xu, and D. Li, Study of the temperature field in microchannels of a PDMS chip with embedded local heater using temperature-dependent fluorescent dye, Int. J.Thermal Sciences 45(9) (2006) 841–847.

[110] R. Fu, and D. Li, Flow velocity measurement in microchannels using temperature-dependent fluorescent dye, Microfluidics and Nanofluidics 3(1) (2007) 27-32.

[111] D. Vigolo, R. Rusconi, H.A. Stone, and R. Piazza, Thermophoresis: microfluidics characterization and separation, Soft Matter 6(15) (2010) 3489–3493.

[112] P. Datta, G. George, S. Tiwari, and J. Goettert, Monolithic fabrication of electro-fluidic polymer microchips, Microsystem Technologies 15(3) (2009) 463–469.

[113] K. Shen, X. Chen, M. Guo, and J. Cheng, A microchip-based PCR device using flexible printed circuit technology, Sensors and Actuators B: Chemical 105(2) (2005) 251–258.

[114] A. Wu, L. Wang, E. Jensen, R. Mathies, and B. Boser, Modular integration of electronics and microfluidic systems using flexible printed circuit boards, Lab on Chip 10 (2009) 519–521.

[115] V. Vandelinder, A.C. M. Ferreon, Y. Gambin, A.A. Deniz, and A. Groisman, High-resolution temperature-concentration diagram of α-Synuclein conformation obtained from a single Förster resonance energy transfer image in a microfluidic device, Anal. Chem. 81 (2009) 6929–6935.

[116] G.V. Casquillas, C. Fu, M. Le Berre, J. Cramer, S. Meance, A. Plecis, D. Baigl, J.J. Greffet, Y. Chen, M. Piela, et al. Fast microfluidic temperature control for high resolution live cell imaging, Lab on Chip 11 (2010) 484-489.

[117] J. Nakane, D. Broemeling, R. Donaldson, A. Marziali, T.D. Willis, M. O'Keefe, and R.W. Davis, A method for parallel, automated, thermal cycling of submicroliter samples, Genome Research 11(3) (2001) 441-447.

[118] Y. Tanaka, M.N. Slyadnev, A. Hibara, M. Tokeshi, and T. Kitamori, Noncontact photothermal control of enzyme reactions on microchip by using a compact diode laser. J Chromatogr A 894 (2000) 45–51.

[119] M.N. Slyadnev, Y. Tanaka, M. Tokeshi, and T. Kitamori, Photothermal temperature control of a chemical reaction on a microchip using an infrared diode laser, Anal. Chem. 73 (2001) 4037–4044.

[120] D. Braun, and A. Libchaber, Trapping of DNA by thermophoretic depletion and convection, Physical review letters 89 (18) (2002) 188103.

[121] A. Kumar, J.S. Kwon, S.J. Williams, N.G. Green, N.K. Yip, and S.T. Wereley, Optically modulated electrokinetic manipulation and concentration of colloidal particles near an electrode surface, Langmuir 26(7) (2010) 5262–5272.

[122] F.M. Weinert, and D. Braun, An optical conveyor for molecules, Nano letters 9(12) (2009) 4264–4267.

[123] Y. Shirasaki, J. Tanaka, H. Makazu, K. Tashiro, S. Shoji, S. Tsukita, and T. Funatsu, On-chip cell sorting system using laser-induced heating of a thermoreversible gelation polymer to control flow, Anal. Chem. 78 (2006) 695–701.

[124] M. Krishnan, J. Park and D. Erickson, Optothermorheological flow manipulation, Optics Letters 34 (2009) 1976-1978.

[125] C.T. Wittwer, G.C. Fillmore, and D.R. Hillyard, Automated polymerase chain reaction in capillary tubes with hot air, Nucleic Acids Research 17(11) (1989) 4353-4357.

[126] H. Swerdlow, B.J. Jones, and C.T. Wittwer, Fully automated DNA reaction and analysis in a fluidic capillary instrument, Anal. Chem. 69 (1997) 848–855.

[127] N. Zhang and E.S. Yeung, On-line coupling of polymerase chain reaction and capillary electrophoresis for automatic DNA typing and HIV-1 diagnosis, J. Chromatogr. B Biomed. Sci. Appl. 714 (1998) 3–11.

[128] Q. Wang and H. Gong, An integrated software solution for real-time PCR analysis based on microfluidic biochip, Proc SPIE 5119 (2003) 77–86.

[129] D.S. Lee, S.H. Park, H.Yang, K.H. Chung, T.H. Yoon, S.J. Kim, et al. Bulk micromachined submicroliter-volume PCR chip with very rapid thermal response and low power consumption, Lab on Chip 4 (2004) 401–7.

[130] Idaho Technology Inc. Rapidcycler user's guide, Idaho Technology, Idaho Falls Idaho (2004).

[131] C. Fermér, P. Nilsson, and M. Larhed, Microwave-assisted high-speed PCR. Eur. J. Pharm. Sci. 18 (2003) 129–132.

[132] K. Orrling, P. Nilsson, M. Gullberg, and M. Larhed, An effective method to perform milliliter-scale PCR utilizing highly controlled microwave thermocycling, Chem. Commun. (2004)790–791.

[133] A. Kempitiya, D.A. Borca-Tasciuc, H.S. Mohamed, and M.M. Hella, Localized microwave heating in microwells for parallel DNA amplification applications, Applied Physics Letters 94 (2009) 064106.

[134] K.J. Shaw, P.T. Docker, J.V. Yelland, C.E. Dyer, J. Greenman, G.M. Greenway, and S.J. Haswell, Rapid PCR amplification using a microfluidic device with integrated microwave heating and air impingement cooling, Lab on Chip 10 (2010) 1725–1728.

[135] S. Caddick, and R. Fitzmaurice, Microwave enhanced synthesis, Tetrahedron 65(17) (2009) 3325–3355.

[136] J.A. Gerbec, D. Magana, A. Washington, and G.F. Strouse, Microwave-enhanced reaction rates for nanoparticle synthesis, JACS 127(45) (2005) 15791–15800.

[137] S. Lin, D. Yun, D. Qi, C. Deng, Y. Li, and X. Zhang, Novel microwave-assisted digestion by trypsin-immobilized magnetic nanoparticles for proteomic analysis, Journal of proteome research 7(3) (2008) 1297–1307.

[138] A. Ramos, A. Robles, P. Garcia-Sanchez, and M.J. Freire, Microwave-induced water flows in microsystems, Applied Physics Letters 94(2) (2009) 024104.

[139] A. Ramos, A. Robles, P. Garcia-Sanchez, and M.J. Freire, Water flows induced by microwave electric fields in microsystems, J. of Electrostatics 67 (2009) 377–380.

[140] D. Issadore, K.J. Humphry, K.A. Brown, L. Sandberg, D. Weitz, and R.M. Westervelt, Microwave dielectric heating of drops in microfluidic devices, Lab on Chip 9 (2009) 1701-1706.

[141] J.J. Shah, J. Geist, and M. Gaitan, Microwave-induced adjustable nonlinear temperature gradients in microfluidic devices, J. of Micromech. and Microeng. 20 (2010) 105025.

[142] L.C. Waters, S.C. Jacobson, N. Kroutchinina, J. Khandurina, R.S. Foote, and J.M. Ramsey, Microchip device for cell lysis, multiplex PCR amplification, and electrophoretic sizing, Anal. Chem. 70 (1998) 158–162.

[143] Tungsten-Halogen lamp information, http://zeiss-campus.magnet.fsu.edu/articles/lightsources/tungstenhalogen.html.

[144] R.P. Oda, M.A. Strausbauch, A.F.R Huhmer, N. Borson, S.R. Jurrens, J. Craighead, P.J. Wettstein, B. Eckloff, B. Kline, and J.P. Landers, Infrared-mediated thermocycling for ultrafast polymerase chain reaction amplification of DNA, Anal. Chem. 70 (1998) 4361–4368.

[145] A.F.R. Hühmer and J.P. Landers, Noncontact infrared-mediated thermocycling for effective polymerase chain reaction amplification of DNA in nanoliter volumes, Anal. Chem. 72 (2000) 5507–5512.

[146] C. Ke, H. Berney, A. Mathewson, and M.M. Sheehan, Rapid amplification for the detection of Mycobacterium tuberculosis using a non-contact heating method in a silicon

microreactor based thermal cycler, Sensors and Actuators B: Chemical 102(2) (2004) 308–314.

[147] D. Psaltis, S.R. Quake, and C. Yang, Developing optofluidic technology through the fusion of microfluidics and optics, Nature 442 (2006) 381–386.

[148] C. Monat, P. Domachuk, and B.J. Eggleton, Integrated optofluidics: A new river of light, Nature Photonics 1 (2) (2007) 106–114.

[149] D. Pal and V. Venkataraman, A portable battery-operated chip thermocycler based on induction heating, Sensors and Actuators A: Physical 102 (2002) 151–156.

[150] J.A. Kim, S.H. Lee, H. Park, J.H. Kim, and T.H. Park, Microheater based on magnetic nanoparticle embedded PDMS, Nanotechnology 21 (2010) 165102.

[151] S. Baek, J. Min, J., and J.H. Park, Wireless induction heating in a microfluidic device for cell lysis, Lab on Chip 10 (2010) 909–917.

[152] S.C. Chen, W.R. Jong, Y.J. Chang, J.A. Chang, and J.C. Cin, Rapid mold temperature variation for assisting the micro injection of high aspect ratio micro-feature parts using induction heating technology, J. of Micromech. and Microeng. 16 (2006) 1783-1791.

[153] B.J. Knauf, D.P. Webb, C. Liu, and P.P. Conway, Low frequency induction heating for the sealing of plastic microfluidic systems, Microfluidics and Nanofluidics 9 (2009) 243–252.

[154] Z. Hua, R. Pal, O. Srivannavit, M.A. Burns, and E. Gulari, A light writable microfluidic "flash memory": Optically addressed actuator array with latched operation for microfluidic applications, Lab Chip 8 (2008) 488-491.

[155] A. Richter, G. Paschew, Optoelectrothermic control of highly integrated polymer-based MEMS applied in an artificial skin, Advanced Materials 21(9) (2009) 979–983.

[156] D. Erickson, D. Sinton, and D. Li, Joule heating and heat transfer in poly (dimethylsiloxane) microfluidic systems, Lab on Chip 3 (2003) 141–149.

[157] A.J. de Mello, M. Habgood, N.L. Lancaster, T. Welton, R.C.R. Wootton, Precise temperature control in microfluidic devices using Joule heating of ionic liquids, Lab on Chip 4 (2004) 417–419.

[158] G. Hu, Q. Xiang, R. Fu, B. Xu, R. Venditti, and D. Li, Electrokinetically controlled real-time polymerase chain reaction in microchannel using Joule heating effect, Analytica Chimica Acta 557 (2006) 146–151.

[159] S. Stern, C. Brooks, M. Strachan, A. Kopf-Sill, J.W. Parce, Thermal and Thermomechanical Phenomena in Electronic Systems, Proceeding of ITHERM 2002.

[160] R.M. Guijt, A. Dodge, G.W.K. van Dedem, N.F. de Rooij, and E. Verpoorte, Chemical and physical processes for integrated temperature control in microfluidic devices, Lab on Chip 3 (2003) 1–4.

[161] G. Maltezos, A. Rajagopal, and A. Scherer, Evaporative cooling in microfluidic channels, Applied Physics Letters 89 (2006) 074107.

[162] A. Stroock, S. Dertinger, A. Ajdari, I. Mezic, H. Stone, G. Whitesides, Chaotic mixer for microchannels, Science 295(5) (2002) 647 –651.

[163] E. Lauga, A. Stroock, H. Stone, Three-dimensional flows in slowly varying planar geometries, Physics of fluids 16 (2004) 3051–3063.

[164] S. Hsieh, Y. Huang, Passive mixing in micro-channels with geometric variations through μPIV and μLIF measurements, Journal of Micromechanics and Microengineering 18 (2008) 065017.

[165] R. Liu, K. Sharp, M. Olsen, M. Stremler, J. Santiago, R. Adrian, H. Aref, D. Beebe, A passive three-dimensional ´SC-shapeŠhelical micromixer, Journal of Microelectromechanical Systems 9 (2) (2000) 190–198.

[166] A. Bertsch, S. Heimgartner, P. Cousseau, P. Renaud, Static micromixers based on large-scale industrial mixer geometry, Lab on a Chip 1(1) (2001) 56–60.

[167] X. Xuan, B. Xu, D. Li, Accelerated Particle Electrophoretic Motion and Separation in Converging- Diverging Microchannels, Anal. Chem 77(14) (2005) 4323–4328.

[168] X. Xuan, D. Li, Particle motions in low-Reynolds number pressure-driven flows through converging–diverging microchannels, Journal of Micromechanics and Microengineering 16 (2006) 62–69.

[169] D.B. Tuckerman, and R.F.W. Pease, High-performance heat sinking for VLSI, Electron Device Letters 2(5) (1981) 126–129.

[170] E. Sparrow, A. Prata, Numerical solutions for laminar flow and heat transfer in a periodically converging-diverging tube, with experimental confirmation, Numerical Heat Transfer, Part A: Applications 6(4) (1983) 441–461.

[171] G. Wang, S. Vanka, Convective heat transfer in periodic wavy passages, Int. J. of Heat and Mass Transfer 38(17) (1995) 3219–3230.

[172] T. Nishimura, Y. Bian, Y. Matsumoto, K. Kunitsugu, Fluid flow and mass transfer characteristics in a sinusoidal wavy-walled tube at moderate Reynolds numbers for steady flow, Heat and Mass Transfer 39(3) (2003) 239–248.

[173] A. Lahbabi, H. Chang, Flow in periodically constricted tubes: transition to inertial and nonsteady flows, Chemical Engineering Science 41(10) (1986) 2487–2505.

[174] A. Payatakes, C. Tien, R. Turian, A new model for granular porous media: Part I. Model formulation, AIChE Journal 19 (1) (1973) 58–67.

[175] Y. Bernabé, J. Olson, The hydraulic conductance of a capillary with a sinusoidally varying cross-section, Geophysical Research Letters 27 (2) (2000) 245–248.

[176] A. Tamayol, M. Bahrami, Analytical determination of viscous permeability of fibrous porous media, Int. J. of Heat and Mass Transfer 52 (2009) 2407–2414.

[177] A. Tamayol, M. Bahrami, In-plane gas permeability of proton exchange membrane fuel cell gas diusion layers, Journal of Power Sources 196 (2010) 3559–3564.

[178] J. Forrester, D. Young, Flow through a converging-diverging tube and its implications in occlusive vascular disease–II: Theoretical and experimental results and their implications, Journal of Biomechanics 3(3) (1970) 307–310.

[179] D. James, G. Chandler, S. Armour, A converging channel rheometer for the measurement of extensional viscosity, Journal of Non-Newtonian Fluid Mechanics 35 (1990) 421–443.

[180] M. Oliveira, M. Alves, F. Pinho, G. McKinley, Viscous flow through microfabricated hyperbolic contractions, Experiments in Fluids 43 (2) (2007) 437–451.

[181] G.L. Morin, Laminar-to-turbulent flow transition in microchannels, Nanoscale and Microscale Thermophysical Engineering 8(1) (2004) 15–30.

[182] J.C. McDonald, D.C. Duffy, J.R. Anderson, D.T. Chiu, H. Wu, O.J.A. Schueller, and G.M. Whitesides, Fabrication of microfluidic systems in poly (dimethylsiloxane), Electrophoresis 21(1) (2000) 27–40.

[183] Y. Sun, Y.C. Kwok, and N.T. Nguyen, J. of Micromech. and Microeng. 16 (2006) 1681-1689.

[184] L.J. Kricka, P. Fortina, N.J. Panaro, P. Wilding, G. Alonso-Amigo, and H. Becker, Fabrication of plastic microchips by hot embossing, Lab on Chip 2(1) (2002) 1–4.

[185] M. Akbari, D. Sinton, and M. Bahrami, Pressure drop in rectangular microchannels as compared with theory based on arbitrary cross section, J. of Fluids Engineering 131 (2009) 041202.

[186] J.C.F. Chow, and K. Soda, Laminar flow in tubes with constriction, Physics of Fluids 15 (1972) 1700–1711.

[187] J. Pfahler, J. Harley, H. Bau, and J. Zemel, Liquid transport in micron and submicron channels, Sensors and Actuators A: Physical 22 (1989) 431–434.

[188] M. Hemmat, and A. Borhan, Creeping flow through sinusoidally constricted capillaries, Physics of Fluids 7 (1995) 2111-2121.

[189] W. Qu, G. Mala, et al., Heat transfer for water flow in trapezoidal silicon microchannels, Int. J. of Heat and Mass Transfer 43 (2000) 3925–3936.

[190] B. Xu, K.T. Ooti, N.T. Wong, and W.K. Choi, Experimental investigation of flow friction for liquid flow in microchannels, Int. Comm. Heat and Mass Transfer 27(8) (2000) 1165–1176.

[191] L. Zhang, J.M. Koo, L. Jiang, M. Asheghi, K.E. Goodson, J.G. Santiago, and T.W. Kenny, Measurements and modeling of two-phase flow in microchannels with nearly constant heat flux boundary conditions, J. of Microelectromechanical Systems 11(1) (2002) 12–19.

[192] J. Judy, D. Maynes, and B.W. Webb, Characterization of frictional pressure drop for liquid flows through microchannels, Int. J. of Heat and Mass Transfer 45 (2002) 3477–3489.

[193] Z.X. Li, Experimental study on flow characteristics of liquid in circular microtubes, Nanoscale and Microscale Thermophys. Eng. 7(3) (2003) 253–265.

[194] H.Y. Wu, and P. Cheng, Friction factors in smooth trapezoidal silicon microchannels with different aspect ratios, Int. J. of Heat and Mass Transfer 46 (2003) 2519–2525.

[195] D. Liu, and S.V. Garimella, Investigation of liquid flow in microchannels, J. of Thermophys. and Heat Transfer 18(1) (2004) 65–72.

[196] S.S. Hsieh, C.Y. Lin, C.F. Huang, and H.H. Tsai, Liquid flow in a micro-channel, J. of Micromech. and Microeng. 14 (2004) 436–446.

[197] R. Baviere, F. Ayela, S. Le Person, and M. Favre-Marinet, Experimental characterization of water flow through smooth rectangular microchannels, Physics of Fluids 17 (2005) 098105.

[198] M. Akbari, D. Sinton, and M. Bahrami, Laminar fully developed flow in periodically converging–diverging microtubes, Heat Transfer Engineering 31(8) (2010) 628–634.

[199] M. Akbari, D. Sinton, and M. Bahrami, Viscous flow in variable cross-section microchannels of arbitrary shapes, Int. J.Heat and Mass Transfer 54 (2011) 3970-3978.

[200] I. Papautsky, T. Ameel, and A.B. Frazier, A review of laminar single-phase flow in microchannels, Proceeding of IMECE2001 (2001).

[201] M.E. Steinke, and S.G. Kandlikar, Single-phase liquid friction factors in microchannels, Int. J. Therm. Sci. 45(11) (2006) 1073–1083.

[202] P. Hrnjak, and X. Tu, Single phase pressure drop in microchannels, Int. J. Heat and Fluid Flow 28 (2007) 2–14.

[203] P. Taheri, M. Torrilhon, and H. Struchtrup, Couette and Poiseuille microflows: analytical solutions for regularized 13-moment equations, Physics of Fluids 21 (2009) 017102.

[204] R.K. Shah, and A.L. London, *Laminar flow forced convection in ducts: a source book for compact heat exchanger analytical data*, (1978) Academic press New York, NY.

[205] M. Yovanovich, Y. Muzychka, Solutions of Poisson equation within singly and doubly connected prismatic domains, in: 1997 National Heat Transfer Conference, Baltimore, MD, 1997.

[206] M. Bahrami, M. Michael Yovanovich, J. Richard Culham, A novel solution for pressure drop in singly connected microchannels of arbitrary cross-section, Int. J. of Heat and Mass Transfer 50 (2007) 2492–2502.

[207] M. Bahrami, A. Tamayol, P. Taheri, Slip-flow pressure drop in microchannels, of general cross section, J. of Fluids Engineering 131 (2009) 031201–8.

[208] Sisavath, S. and Jing, X. and Zimmerman, R.W., Laminar flow through irregularly-shaped pores in sedimentary rocks, Transport in Porous Media 45(1) (2001) 41–62.

[209] S. Sisavath, A. Al-Yaaruby, C. Pain, R. Zimmerman, A simple model for deviations from the cubic law for a fracture undergoing dilation or closure, Pure and Applied Geophysics 160 (5) (2003) 1009–1022.

[210] S. Sisavath, X. Jing, R. Zimmerman, Creeping flow through a pipe of varying radius, Physics of Fluids 13 (2001) 2762–2772.

[211] M. Manton, Low Reynolds number flow in slowly varying axisymmetric tubes, Journal of Fluid Mechanics 49 (03) (2006) 451–459.

[212] M. Van Dyke, Slow variations in continuum mechanics, Advances in Applied Mechanics 25 (1987) 1–45.

[213] P. Kitanidis, B. Dykaar, Stokes flow in a slowly varying two-dimensional periodic pore, Transport in Porous Media 26 (1) (1997) 89–98.

[214] J. Deiber, W. Schowalter, Flow through tubes with sinusoidal axial variations in diameter, AIChE Journal 25 (4) (1979) 638–645.

[215] R. Wild, T. Pedley, D. Riley, Viscous flow in collapsible tubes of slowly varying elliptical cross-section, Journal of Fluid Mechanics 81 (02) (1977) 273–294.

[216] A. Gat, I. Frankel, D. Weihs, A higher-order Hele-Shaw approximation with application to gas flows through shallow micro-channels, Journal of Fluid Mechanics 638 (2009) 141–160.

[217] G. Batchelor, *An introduction to fluid dynamics*, (2000) Cambridge Univ. Press.

Chapter 3

Summary of Contributions

3.1 Optothermal analyte manipulation with temperature gradient focusing

Biochemical assays have seen a trend toward miniaturization as researchers strive to develop faster, more sensitive, and less expensive assays. Sample preconcentration is a critical operation required for the determination of trace amount of analytes for which the concentration in the original solution is lower than the detection limits of the instrument. Among many studies devoted to the development of preconcentration techniques, temperature gradient focusing is a novel method in which the temperature dependent electrophoretic velocity is balanced by the bulk velocity at a certain temperature along a temperature profile. In this research, an optothermal analyte preconcentration and manipulation method based on temperature gradient focusing platform is proposed. The approach presented in this thesis offers a flexible, noncontact technique for focusing and transporting of sample analytes. The local concentration of several sample analytes such as: fluorescein, Oregon Green 488, and HPTS along a microcapillary has been increased and the focused band is successfully transported along the capillary by adjusting the heater image in an external computer.

For further information, the reader is referred to Appendix A.

3.2 Local fluid temperature control in microfluidics

3.2.1 Optothermal control of local fluid temperature in microfluidics

Improved temperature control is one of the main motivating factors for some of the earliest microfluidic chip based systems. Active control of fluid temperatures is now central to many microfluidic and lab on chip applications. Amplification and sensing processes such as polymerase chain reaction (PCR), temperature gradient focusing technique (TGF), temperature gradient gel electrophoresis (TGGEF), and protein denaturation require precise temperature control for operation.

Use of an integrated electrical heater is one of the most common methods for on-chip temperature control, however, the heating structures must be designed, fabricated, and integrated within the microchip, and the location of the heated zones cannot be changed dynamically. The fabrication of integrated heaters is also fairly complex (such as patterning multilayer soft-lithography systems or on-chip heaters), and the heaters must be interfaced with the external environment (e.g. electrical connections). Limitations associated with fixed on-chip electrical heaters has motivated the development of non-contact heating approaches; particularly optothermal heating methods.

In this work, we use a commercial video projector and an optical setup to achieve optothermal heating of an aqueous solution in a microfluidic channel. This method presents improved flexibility over integrated heaters, and can produce localized heating and simultaneous heat sources at multiple locations with the ability of dynamic control on the size and and power of the heater. The thermal characteristics of the heating system were measured by using the temperature-dependent fluorescent dye method.

For further information, the reader is referred to Appendix B.

3.2.2 Geometrical effects on the temperature distribution in a half-space due to a moving heat source

Detailed knowledge about the temperature profile due to the localized heating is essential in the design and optimization of microsystems. In many cases, due to the usually small flow rates and microchannel characteristic length scales, the effect of flow on the temperature distribution is negligible, thus conduction is the dominant mode of heat transfer. Moreover,

the length scale of many heating elements is usually much smaller than the dimensions of other components of the system. Therefore, considering the heating element and the microchip assembly and/or the ambient medium as a heat source on a half-space is a fair assumption.

With that in mind, the fundamental problem of heat transfer within a half-space due to a moving heat source of hyperelliptical geometry is studied. The considered hyperelliptical geometry family covers a wide range of heat source shapes including: star-shaped, rhombic, elliptical, rectangular-with-round-corners, rectangular, circular and square. The effects of the heat source speed, aspect ratio, corners, and orientation are investigated using the general solution of a moving point source on a half-space and superposition. Selecting the square root of the heat source area as the characteristics length scale, it is shown that the maximum temperature within the half-space is a function of the beam speed (Peclet number) and the heat source aspect ratio. It is observed that the details of the exact heat source shape, e.g., sharp corners have negligible effect on the maximum temperature within the half-space. New general compact relationships are introduced that can predict the maximum temperature within the half-space with reasonable accuracy. The validity of the suggested relationships is examined by available experimental and numerical data for grinding process for medium Peclet numbers. For ultra-fast heat sources an independent experimental study is performed using a commercial CO_2 laser system. The measured depth of the engraved grooves is successfully predicted by the proposed relationships.

For further information, the reader is referred to Appendix C.

3.3 Fluid flow in microchannels

3.3.1 Pressure drop in microchannels as compared to theory based on arbitrary cross-section

In biological and life sciences, microchannels are used widely for analyzing biological materials such as proteins, DNA, cells, embryos and chemical reagents. Micro- and minichannels show potential and have been incorporated in a wide variety of unique, compact, and efficient cooling applications in microelectronic devices. Various microsystems such as micro-heat sinks, micro-biochips, micro-reactors and micro-nozzles have been developed

in recent years. Since microchannels are usually integrated in these microsystems, it is important to determine the characteristics of the fluid flow in microchannels for better design of various micro-flow devices. In parallel to the recent advances in microfluidics and microelectromechanical systems (MEMS), microfabrication techniques have evolved. As a result of recent advances in microfabrication techniques, microchannels with different cross-sectional geometries are fabricated for both commercial and scientific purposes. Some examples are: lithography (soft and photolithography), trapezoidal or rectangular, laser micromachining, triangular, and chemical etching, trapezoidal. Finding exact analytical solutions for many practical cross-sections such as rectangular or trapezoidal even for straight channels is complex and/or impossible. Thus approximate methods can be powerful tools to determine the pressure drop in microchannels with various cross-sectional geometries, without getting into the details of fluid flow and velocity distributions.

An experimental test bed was designed and samples were prepared. The experimental setup was an open loop system comprised of a syringe pump, pressure transducer, microfilter, scale, and a data acquisition system. Frictional pressure drop measurements were conducted over a range of Reynolds number from 1 to 35 for rectangular cross-section microchannels fabricated with soft lithography method in the aspect ratio range of $0.13 < \varepsilon < 0.76$. Comparing the results with the general theoretical model developed for arbitrary cross-section microchannels showed good agreement between the model and experimental data. Uncertainty analysis showed that the measurement of channel dimensions and flow rate is critical in microscales. Here, microchannel cross-section geometry was determined through processing high quality images of the channel cross-section.

For further information, the reader is referred to Appendix D.

3.3.2 Laminar flow pressure drop in converging-diverging microtubes

Laminar fully-developed flow and pressure drop in linearly varying cross-sectional converging-diverging microtubes have been investigated in this work. These microtubes are formed from a series of converging-diverging modules. An analytical model is developed for frictional flow resistance assuming parabolic axial velocity profile in the diverging and converging sections. For the range of Reynolds number and geometrical parameters considered in this work, numerical observations show that the parabolic assumption of the axial veloc-

ity is valid. The flow resistance is found to be only a function of geometrical parameters. To validate the model, a numerical study is conducted for the Reynolds number ranging from 0.01 to 100, for various taper angles, from 2 to 15 degrees and maximum-minimum radius ratios ranging from 0.5 to 1. Comparisons between the model and the numerical results show that the proposed model predicts the axial velocity and the flow resistance accurately. As expected, the flow resistance is found to be effectively independent of the Reynolds number from the numerical results. Parametric study shows that the effect of radius ratio is more significant than the taper angle. It is also observed that for small taper angles (angels smaller than 10 degree), flow resistance can be determined accurately by applying the locally Poiseuille flow approximation.

For further information, the reader is referred to Appendix E.

3.3.3 Viscous flow in variable cross-section microchannels of arbitrary shapes

The concept of flow through microchannels with gradually varying walls forms the basis of a class of problems in microfluidics which has applications in micromixer design, accelerated particle electrophoresis, heat transfer augmentation in micro heat sinks , flow through porous media, blood flow in the context of biomechanics, preconcentration and separation of molecules, and polymer processing. In most of these applications, it is required to obtain a reasonable estimate of the pressure drop in the channel for basic design and optimization. As a result, pressure drop in microconduits with variable cross-sections has been the subject of several investigations.

In this study, an approximate method for the determination of the pressure drop of laminar, single-phase flow in slowly-varying microchannels of arbitrary cross-section is developed. Starting from the solution of an elliptical cross-section, a generalized approximate model is proposed to compute the pressure drop in stream-wise periodic geometries, expansions and contractions. To verify the proposed model, an independent experimental investigation is carried out for stream-wise converging-diverging channels of rectangular cross-section with linear wall. Further validation is performed by comparing the results obtained from the present model and those obtained experimentally and numerically for a hyperbolic contraction of rectangular cross-section [180]. The proposed approach provides

a powerful tool for basic designs, parametric studies, and the optimization analyses.

For further information, the reader is referred to Appendix F.

Chapter 4

Conclusions and Future Work

The future work for this dissertation mainly revolves around the attempt towards the miniaturization of the proposed optothermal analyte preconcentration and manipulation technique, and eventually commercialization. The future microfluidic system will be a portable device with the ability to perform both preconcentration and separation processes on a single microchip. The optothermal heating method in its current format has two major drawbacks: it is bulky and thermally inefficient. Hence, future modifications will include a careful redesign and optimization of the system by substituting the current light source, i.e., mercury lamp, with a more efficient source, for example, a laser, and using digital micromirror arrays that provide excellent spatial control of light distribution. The system will be transferred to a PDMS-based platform to enhance the integrability of the process with other components of a microfluidic system, for example a sensor or a reactor. A light absorbing material, most probably indium tin oxide (ITO) or black carbon, will be coated on one surface of the analysis channels. A novel preconcentration strategy will be employed by taking advantage of the flexibility offered by the optothermal system to eliminate the pressure driven flow. Briefly, the heater image will be adjusted, analogous to a movie, with the speed of the required pressure driven velocity to produce focusing condition for the analyte molecule. This has been demonstrated through our preliminary numerical simulation.

A theoretical investigation will be performed for design and optimization purposes. This will be done by validating the proposed one-dimensional heat transfer model and combining it with species conservation equation. The final theoretical model will be able to predict the amount of concentration enrichment for one (or more) sample analyte(s)

under certain thermal and electrokinetic conditions. The model will also provide useful feedback information such as the required heat flux, heater size, and heater speed for the system to be able to separate different analytes and transport the separated bands to the point of analysis.

On the fundamental side, the theoretical study conducted for the viscous flow in microchannels of arbitrary cross-sectional shape in present work will be extended the slip-flow boundary condition. Compact general models will be developed for gas flow in slowly varying microchannels or arbitrary cross-section. This will eventually lead to a unified model that can be used for the estimation of pressure drop in microchannels with general cross-sectional shapes and arbitrary wall profile. The unified model will be supported by data collected from the literature and independent numerical and experimental studies that will be conducted. The unified model can be used in the design and optimization of microfluidic devices such as microchannel heat sinks, micromixers, microreactors, and microsensors with no need to have information about the details of the fluid flow.

Present study will also be a benchmark for another interesting research area called flow regulation using non-Newtonian fluids. Dynamic control and manipulation of flow in microchannels is essential in the development of lab-on-chip devices; applications including biomolecular separations, enzymatic assays, the polymerase chain reaction, and immunohybridization reactions assays. A valving/actuation technique will be presented based on the thermo-responsive polymeric gels. These gels undergo a volumetric or phase change in response to changes in temperature and will be used here as a working fluid in a microfluidic system. By heating certain areas of the microfluidic system or through the gel self-heating, temporary blockage of the microchannel will be achieved. The objectives of this research will be to employ thermo-responsive polymeric gels to i) develop a contactless optothermal method for on-the-fly flow control and ii) introduce a passive flow regulation method based on the self-heating behavior of the gel. This method has the following advantages over other available methods: fast flow control can be obtained due to the quick temperature diffusion in microscales, O(1ms); less complicated electronic controlling systems are required, and there are no moving parts involved. These advantages will lead to a low cost integratable valving/actuation system that can be used in many lab-on-chip devices.

Appendices

Appendix A

Optothermal analyte manipulation with temperature gradient focusing

(submitted to the Journal of Microfluidics and Nanofluidics)

Journal of Microfluidics and Nanofluidics manuscript No.
(will be inserted by the editor)

Optothermal sample preconcentration and manipulation with temperature gradient focusing

M.Akbari · M.Bahrami · D. Sinton

Received: date / Accepted: date

Abstract We present an optothermal analyte preconcentration method based on temperature gradient focusing. This approach offers a flexible, noninvasive technique for focusing and transporting charged analytes in microfluidics using light energy. The method uses the optical field control provided by a digital projector as established for particle manipulation, to achieve analogous functionality for molecular analytes for the first time. The optothermal heating system is characterized and the ability to control of the heated zone location, size and power is demonstrated. The method is applied to concentrate a sample model analyte, along a microcapillary, resulting in almost 500-fold local concentration increase in 15 minutes. Optically-controlled upstream and downstream transport of a focused analyte band is demonstrated with a heater velocity of ~ 170 μm/min.

Corresponding author: David Sinton

Department of Mechanical and Industrial Engineering, University of Toronto, 5 King's College Rd., Toronto, ON, M5S 3G8, Canada.

Tel.: +1(416)-978-3040

E-mail: sinton@mie.utoronto.ca

Keywords optothermal · temperature gradient focusing · preconcentration · analyte manipulation · microfluidics

1 Introduction

Widespread application of point-of-care (POC) medical diagnostic systems will require operation with relatively small volumes of highly complex fluids [1–5]. Challenges in the development of these systems include: the detection of very dilute solutions of analytes in small volumes, the mismatch between small volumes employed in the analysis and larger volumes required to facilitate testing, and the need to transport the sample and/or the test result. To address some of these challenges, several microfluidics-based methods for analyte preconcentration and manipulation have been developed [6], examples include: field amplified stacking (FAS) [7–10], isotachophoresis (ITP) [11,12], sweeping [13–15], electric field gradient focusing (EFGF) [16–18], and temperature gradient focusing (TGF) [6,19–29].

In TGF, the charged analytes are concentrated locally by balancing the bulk flow in a channel against the electrophoretic migrative flux of an analyte along a controlled temperature profile [6]. The principle behind the TGF mechanism is illustrated in Fig. 1. The temperature gradient is critical as local focusing of analytes occurs only at the point in the channel where the analyte velocity due to bulk flow cancels that due to electrophoresis, which is temperature dependant [6]. Available methods that can provide the required temperature variations include: thin-film heating elements made of platinum (Pt), indium tin oxide (ITO), and non-metallic polysilicon [36–38]; heating/cooling blocks [6,19,25]; embedded resistive wires or silver-filled epoxy [39,40]; external Peltier modules [6,21,41]; localized convective heating [42,43]; infrared, visible, or microwave radiation [33,34,44–46]; chemical reactions [47]; and Joule heating [25,48]. Among the abovementioned methods,

heating/cooling blocks [6,19,25], Peltier elements [21,26], and Joule heating in a variable cross-section microchannel [6,25] have been used for analyte preconcentration with TGF.

Optical methods have been widely applied to manipulate particles [49–53] and bulk fluids [54–56] in microfluidics, predominantly under the name of optofluidics [57]. Digital projection systems and digital micromirror arrays offer excellent spatial control of lighting relatively inexpensive, commercially available components. Most notably, a projected image on a photoconductive surface enabled the dynamic reconfiguration of planar electrodes that enabled the control of planar particle motion in arbitrary manner [50]. A similar method was applied to control flow, and ultimately the microfluidic structure, using a temperature-dependent viscosity fluid and local optothermal heating [58]. The flexibility offered by digital projection optics has thus been applied using various strategies for particle and bulk fluid manipulation, however, an analogous method has not been developed to date for charged molecules, the most common analytes of interest in micro total analysis systems [59].

In the present study, an optothermal analyte preconcentration and manipulation method is developed by using a commercial video projector and beam shaping optics. The major advantage associated with this method is its flexibility, which enables on-demand control of the location, size, and the amount of heat energy delivered. This enables the dynamic control of the focused band location and its on-demand transportation to, for instance, a sensor. Moreover, since the proposed method is noninvasive, predefined geometries and/or complex fabrication methods associated with integrated heaters are avoided, leading to a much simpler system. Since lower applied electric fields can be used for preconcentration, the instabilities of Joule heating effect-based systems are also avoided. Most importantly, these results demonstrate a non-invasive way to concentrate and manipulate charged analytes in microfluidics, independent of fluid flow. This capability could enable a variety of analysis protocols not possible where flow and diffusion are the only modes of transport.

We assessed the thermal characteristics of the optothermal approach using a temperature-dependent fluorescent dye. The optothermal approach is applied to preconcentrate charged analytes using TGF, and optically manipulate analytes independent of fluid flow.

2 Experimental Section

2.1 Experimental setup

An inverted epi-fluorescent microscope (Jenco, Oregon) equipped with a 5X, 0.12 N.A. long distance objective, rhodamine B (excitation: band pass 546 nm, emission: band pass 600 nm) and green (excitation: band pass 540 nm, emission: band pass 580 nm) filter sets, a broadband mercury illumination source, and a digital CCD camera were used. Image acquisition and storage were controlled by Zarbco video toolbox (Ver. 1.65) software. Ultra-small pressure driven flow was produced by using hydrostatic pressure (i.e., adjusting the relative heights of two external reservoirs). A commercial video projector (Sony, 3-LDC BrightEra, 190 W Mercury lamp, 1600/2000 ANSI lumens) equipped with special optics was used for optothermic control of the system. Figure 2 illustrates the experimental setup, which was designed to control the local fluid temperature in the capillary. The location, size, and amount of heat that entered the heated area were controlled by adjusting the heater image from an external computer.

2.2 Materials and microfluidic assembly

Background electrolyte of Tris-Borate buffer (900 mM, pH=8.5) was used for all experiments. Laser grade temperature sensitive dye, rhodamine B (Sigma Aldrish, St. Louis, MO),

was used for temperature measurements. Fluorescein was purchased from Invitrogen (Invitrogen Inc., ON) for focusing demonstrations.

A 50 mm long rectangular borosilicate glass capillary (Vitrocom, NJ) with nominal inner dimensions of 20 μm $\times$ 200 μm was used as the microchannel. The capillary was mounted on a Plexiglas substrate (25 mm$\times$75 mm $\times$ 1 mm) using an acrylic double sided tape (Adhesives Research, Inc.). The substrate was cut to the size by using a CO_2 laser system (Universal Laser System, Model VSL 3.60, Scottsdale, AZ). Pipette tips were cut, inverted (wide side down), and epoxied at the channel ends to interface to the external fluidics. A black electric tape was fixed on the surface of the microchannel, serving as a light absorbing material. Images were projected onto the surface of the black surface using the optical setup explained in Sec. 2.1.

2.3 Temperature measurement

We performed *in situ* temperature field imaging based upon the temperature-dependent quantum efficiency of rhodamine B dye, using the method described in Refs. [48,60]. Briefly, 0.3 mM rhodamine B in 900 mM Tris-borate buffer solution was prepared and introduced into the microchannel. A background and an isothermal "cold field" intensity image of the system were taken prior to each experiment. Following the acquisition of the cold field image, a rectangular strip of light was projected on the surface of the black tape to provide localized heating. Images were taken every 2 seconds with a resolution of 1280 $\times$ 1024 pixels, spanning a length of 3.5 mm of the channel. To extract the in-channel temperature profiles, the background image was first subtracted from each raw image and the cold field. The corrected raw images were then normalized with the corrected cold field images. The intensity values of the treated images were then converted to temperature using the intensity *vs.* tem-

perature calibration described as follows: a Plexiglas reservoir containing approximately 0.1mL rhodamine B dye (0.3 mM in 900 mM Tris-Borate buffer) was fabricated using a laser system (Universal laser Microsystems Inc., USA) with an embedded k-type thermocouple. The voltage read by the thermocouple was then recorded by Labview 8.5 software (National Instruments, USA) via a standard data acquisition card (National Instruments, 16 - bit, 250KS/s). Initially the reservoir was loaded with dye solution at room temperature and the entire system was heated to approximately 75°C. The system was allowed to cool in air while intensity images were taken at specified intervals and the data acquisition system recorded the instantaneous thermocouple readings. A low-pass filter was employed to cut off the high frequency noises in the thermocouple readings. Random locations close to the thermocouple in the calibration images were then selected and their average intensity at each temperature was normalized such that an intensity of 1 corresponded to the temperature of 26°C. The calibration curve agreed well with the results reported in previous works [47,48, 60]. A more detailed description of the calibration process is provided in the supporting document. It should be noted that since the channel depth in this work is much smaller than its width, the monitored 2D fluorescence intensity accurately represents the temperature field of the fluid within the microchannel.

2.4 Focusing protocol

Focusing experiments were performed using 0.1 mM of fluorescein in 900 mM Tris-Borate buffer at the pH of 8.5. Before each experiment, the channel and reservoirs were flushed with distilled water and buffer for at least 15min. Both reservoirs were emptied and 0.1 mM fluorescein solution was introduced in one reservoir and the channel was allowed to fill with the hydrostatic pressure. Then the other reservoir was filled with fluorescein and the pressure

head was applied. The heat source was projected on the surface of the black tape, the electric field was switched on after the steady state temperature was achieved, and image acquisition was performed every 20 seconds. After the electric potential was applied to the channel, the pressure head was adjusted until the focused band was observed.

3 Results and Discussion

Figure 3 demonstrates the ability of the proposed optothermal approach to provide localized heating and control the location of the heated area by adjusting the projected image. These results demonstrate localized heating through the proposed optothermal strategy, and indicate that the temperature profile along the channel due to the localized heating has a Gaussian distribution as is expected from axial conduction heat transfer. As shown, a temperature increase up to 20°C (maximum temperature achieved in this experiment was about 50°C) was obtained for a heater with the width of 1.5 mm. Due to the low Peclet number in our experiments (~ 0.015 for the velocities on the order of 0.2 mm/s), convective heat transfer and flow effects tend to have negligible influence on the temperature distribution.

The thermal response of the heating system is shown in Fig. 4. The maximum temperature along the channel is reported for each data point. After the heater image is projected, the temperature rises quite quickly but the rate slows with time and reaches its steady-state condition after about 25 seconds. The heating and cooling rates measured in this work are $\sim 0.8^{\circ}\mathrm{C}/\mathrm{s}$ for a typical heater width of 1.5 mm. Note that the heating and cooling rates vary with the heat source width such that a smaller heater size leads to faster heating/cooling ramps. Our measurements also showed that the maximum temperature varies almost linearly with the width of the projected heater. This is expected as more heat is transferred to the fluid inside the microchannel for larger heat sources.

The ability to locally concentrate a model analyte, fluorescein dye, was achieved by combining the optothermal heating strategy with the temperature gradient focusing approach. Figure 5 shows the image sequences of the focusing experiment. The applied electric field for this experiment was 200 V/cm with the positive polarity on the right reservoir. The projected heater was 1.5 mm wide. Fluorescein molecules migrate from left to right due to their negatively charged surface while the electroosmotic velocity is from right to left. To balance the net velocity of the fluorescein molecules, a 25 mm-H_2O pressure head, which was accomplished by adjusting the relative heights of two external reservoirs, was applied in favour of the electroosmotic flow (i.e., from right to left). Note that the symmetric shape of the temperature profile yields two possible locations for focusing (i.e., where $u_{net} = 0$). However, focusing only occurs at one of these points where $du_{net}/dx < 0$ and species depletion occurs at the other one. The current was monitored during the experiment to ensure that the Joule heating effect did not disturb the focused band. No change in the measured current versus time was observed throughout the entire experiment, which suggests that Joule heating effect was negligible.

Variation of normalized peak concentration versus time for two trials is plotted in Fig. 6. Normalized peak concentration was calculated as the ratio of maximum flourescein intensity at each time over the maximum initial intensity of the dye. The experiment was run twice to ensure the reproducibility of the results. After approximately 15 minutes of focusing, a 500-fold concentration enrichment was achieved with an almost linear increase over time. This trend is consistent with the results obtained by Ross and Locascio [6]. Stability of the focused band was examined by monitoring the concentration peak location over time. No change in the location of the peak concentration was observed within the period of 15 minutes.

A key benefit of optical control in microfluidics is the flexibility it provides. On-demand transport and manipulation of the focused band of analyte was achieved here by moving the projected heater image using the external computer. Figure 7 shows the image sequences of the model analyte, fluorescein, band transported in two directions, as well as the heater location at each step. The direction and magnitude of the pressure driven flow and electric field remained unchanged from those applied in Figure 4. Movies showing the controlled translation of the analyte band are available in supporting information. To ensure that the focused band is transported only by moving the heater image, the stability of the focused band at the initial location was examined by taking images every 2 seconds for 3 minutes and monitoring the location of the peak concentration. Once the stable band was established, the heat source was translated 500 μm every 3 minutes (this is equivalent to a velocity of ~ 170 μm/min) to generate a quasi-steady moving heat source. As can be seen, the focused band follows the heater image in both directions indicating the successful transport of the focused band from left to right and vice versa. This ability provides the possibility to increase the local concentration of a diluted solution up to a certain level and then transport the concentrated band to, for example, combine with another solution, or to a sensing surface. The optical manipulation of the temperature field would also enable dynamic separation of charged analytes as demonstrated previously with fixed-heater type TGF. This can be done through increasing the local concentration of each analyte by adjusting the light intensity and sequentially separating the focused bands.

4 Conclusions

In this work, an optothermal analyte preconcentration and manipulation method based on temperature gradient focusing (TGF) was introduced for the first time. Optothermal fluid

temperature field control was achieved by means of a commercial digital projector; the concentration of a sample analyte, fluorescein, was locally increased; and the focused band was successfully transported along the microchannel by adjusting the image of the heater in an external computer. The proposed method offers the following unique features in its present format:

1. Flexibility-dynamic control of the heater size, location and power. This ultimately leads to the dynamic control of the focused band location and its on-demand transportation to the point of analysis, for example, a sensor.
2. Noninvasive heating-avoids complex fabrication methods and/or controlling systems as well as predefined focusing geometries.

In addition, the proposed technique enables preconcentration to be performed in short channels, thus smaller footprints may be used. This leads to more compact microdevices and the ability of being integrated with other chemical assays.

Thermal characteristics of the heating system were assessed by using a temperature-dependent fluorescent dye. Up to 20°C temperature rise was obtained within 25 seconds for a heater size of approximately 1.5 mm. The maximum temperature decreases for smaller heater sizes, but the heating rate increases. The preconcentration experiment was performed and up to 500-fold enrichment was obtained within 15 minutes. Optically-controlled transport of the focused band was successfully demonstrated by moving the heater image with a velocity of $\sim 170\ \mu$m/min. Future research will include the implementation of the flexibility offered by the proposed technique to separate and translate various analytes sequentially. In addition, a translating heat source could be applied to remove the requirement for pressure-driven flow.

5 Acknowledgements

The authors gratefully acknowledge the financial support of the Natural Sciences and Engineering Research Council of Canada NSERC through discovery grants to MB and DS, BC Innovation Council (BCIC) through research scholarship to MA, and the Canada Research Chair Program.

References

1. Yager, P, Edwards, T., Fu, E., Helton, K., Nelson, K., Tam, M.R., and Weigl, B.H., Microfluidic diagnostic technologies for global public health, Nature, 442, 412–418 (2006).
2. Dupuy, A., Lehmann, S., and Cristol, J., Protein biochip systems for the clinical laboratory, Clin. Chem. Lab. Med., 43, 1219-1302 (2005)
3. Toner, M. and Irimia, D., Blood-on-a-chip, Annu. Rev. Biomed. Eng., 7, 77-103 (2005).
4. Yager, P. and Domingo, G.J. and Gerdes, J., Point-of-care diagnostics for global health, Annu. Rev. Biomed. Eng., 10, 107-144 (2008).
5. Myers, F.B. and Lee, L.P., Innovations in optical microfluidic technologies for point-of-care diagnostics, Lab Chip, 8, 2015-2031 (2009).
6. Ross, D. and Locascio, L.E., Microfluidic temperature gradient focusing, Anal. Chem., 74, 2556-2564 (2002).
7. Mikkers, F. E. P., Everaerts, F. M., and Verheggen, P. E. M., High-performance zone electrophoresis, J. Chromatgr., 169, 11-20 (1979) .
8. Burgi, D. S. and Chien, R.-L., Optimization in sample stacking for high-performance capillary electrophoresis, Anal. Chem., 63, 2042-2047 (1991).
9. Chien, R.-L., and Burgi, D. S., Sample stacking of an extremely large injection volume in high-performance capillary electrophoresis, Anal. Chem., 64, 1046-1050 (1992).
10. Albert, M., Debusschere, L., Demesmay, C., and Rocca, J. L., Large-volume stacking for quantitative analysis of anions in capillary electrophoresis I. Large-volume stacking with polarity switching , J. Chromatgr.A, 757, 281-289 (1997).
11. Boček, P., Deml, M., and Janák, J., Effect of a concentration cascade of the leading electrolyte on the separation capacity in isotachophoresis, J. Chromatogr., 156, 323–326 (1978).

12. Everaerts, F. M., Verheggen, P. E. M., and Mikkers, F. E. P., Determination of substances at low concentrations in complex mixtures by isotachophoresis with column coupling, J. Chromatogr., 169, 21–38 (1979).
13. Quirino, J. P. and Terabe, S., Exceeding 5000-fold concentration of dilute analytes in micellar electrokinetic chromatography, Science, 282, 465-468 (1998).
14. Quirino, J. P. and Terabe, S., Sweeping of analyte zones in electrokinetic chromatography, Anal. Chem., 71, 1638-1644 (1999).
15. Isoo, K. and Terabe, S., Analysis of metal ions by sweeping via dynamic complexation and cation-selective exhaustive injection in capillary electrophoresis, Anal. Chem., 75, 6789-6798 (2003).
16. Koegler, W. S. and Ivory, C. F., Focusing proteins in an electric field gradient, J. Chromatgr. A, 726, 229-236 (1996).
17. Tolley, H. D., Wang, Q., LeFebre, D. A., and Lee, M. L., Equilibrium gradient methods with nonlinear field intensity gradient: a theoretical approach, Anal. Chem., 74, 4456-4463 (2002).
18. Astroga-Wells, J., Vollmer, S., Tryggvason, S., Bergman, T., and Jőrnvall, H., Microfluidic electrocapture for separation of peptides, Anal. Chem., 77, 7131-7136 (2005).
19. Balss, K.M., Vreeland, W.N., Howell, P.B., Henry, A.C., and Ross, D., Micellar affinity gradient focusing: a new method for electrokinetic focusing, J. Am. Chem. Soc., 126, 1936-1937 (2004).
20. Hoebel, S.J. and Balss, K.M. and Jones, B.J. and Malliaris, C.D. and Munson, M.S. and Vreeland, W.N., and Ross, D., Scanning temperature gradient focusing, Anal. Chem., 78, 7186-7190 (2006).
21. Huber, D. and Santiago, J.G., Taylor–Aris dispersion in temperature gradient focusing, Electrophoresis, 28, 2333-2344 (2007).
22. Kamande, M.W., Ross, D., Locascio, L.E., Lowry, M., and Warner, I.M., Simultaneous concentration and separation of coumarins using a molecular micelle in micellar affinity gradient focusing, Anal. Chem., 79, 1791-1796 (2007).
23. Munson, M.S. and Danger, G. and Shackman, J.G. and Ross, D., Temperature gradient focusing with field-amplified continuous sample injection for dual-stage analyte enrichment and separation, Anal. Chem., 79, 6201-6207 (2007).
24. Shackman, J.G. and Ross, D., Counter-flow gradient electrofocusing, Electrophoresis, 28, 556-571 (2007).
25. Sommer, G.J., Kim, S.M., Littrel, R.J., and Hasselbrink, E.F., Theoretical and numerical analysis of temperature gradient focusing via Joule heating, Lab Chip, 7, 898-907 (2007).

26. Matsui, T., Franzke, J., Manz, A., and Janasek, D., Temperature gradient focusing in a PDMS/glass hybrid microfluidic chip, Electrophoresis, 28, 4606–4611 (2007).

27. Tang, G. and Yang, C., Numerical modeling of Joule heating-induced temperature gradient focusing in microfluidic channels, Electrophoresis, 29, 1006-1012 (2008).

28. Becker, M. and Mansouri, A. and Beilein, C., and Janasek, D., Temperature gradient focusing in miniaturized free-flow electrophoresis devices, Electrophoresis, 30, 4206-4212 (2009).

29. Ge, Z. and Yang, C. and Tang, G., Concentration enhancement of sample solutes in a sudden expansion microchannel with Joule heating, Int. J. Heat and Mass Transfer, 53, 2722-2731 (2010).

30. Watts, P., Chemical synthesis in micro reactors, Chemie Ingenieur Technik, 76, 555–559 (2004).

31. Pennel, T., Suchyna, T., Wang, j., Heo, J., Felske, J., Sachs, F., and Hau, S., Microfluidic microchip to produce temperature jumps for electrophysiology, Anal. Chem., 80, 2447-2451 (2008).

32. Zhang, C., Xu, J., Ma, W., and Zheng, W., PCR microfluidic devices for DNA amplification, Biotechnology Advances, 24, 243-284 (2006).

33. Duhr, S. and Braun, D., Why molecules move along a temperature gradient, PNAS, 103(52), 19678-19682 (2006).

34. Krishnan, M., Oark, J., and Erickson, D., Optothermorheological flow manipulation, Optics Letters, 34 (13), 1976-1978 (2009).

35. Richter, A. and Paschew, G., Optoelectrothermic control of highly integrated polymer-Based MEMS applied in an artificial skin, Advanced Materials, 21, 979-983 (2009).

36. Yang, H., Choi, C.A., Chung, K.H., Jun, C.H., and Kim Y.T., An independent temperature-controllable microelectrode array. Anal. Chem., 76, (5), 1537– 43 (2004).

37. Kaigala, G. V., Hoang, V. N., Stickel, A., Lauzon, J., Manage, D., Pilarski, L. M., and Backhouse, C. J., An inexpensive and portable microchip-based platform for integrated RT–PCR and capillary electrophoresis, Analyst, 133, 331–338 (2008).

38. Liao, C.S., Lee, G.B., Wu, J.J., Chang, C.C., Hsieh, T.M., and Huang, F.C., Micromachined polymerase chain reaction system for multiple DNA amplification of upper respiratory tract infectious diseases, Biosens. Bioelectron., 20, 1341–1348 (2005).

39. Fu, R., Xu, B., and Li, D., Study of the temperature field in microchannels of a PDMS chip with embedded local heater using temperature-dependent fluorescent dye, Int. J. Thermal Science, 45, 841-847 (2006).

40. Vigolo, D., Rusconi, R., Piazzaa, R., and Howard A., Stone, A., Portable device for temperature control along microchannels, Lab Chip, 10, 795-798 (2010).

41. Liu, Y., Rauch, C. B., Stevens, R. L., Lenigk, R., Yang, J., Rhine, D. B. , and Grodzinski, P., DNA Amplification and hybridization assays in integrated plastic monolithic devices, Anal. Chem., 74, 3063–3070 (2002).

42. Lee, D.S., Park, S.H., Yang, H., Chung, K.H,, Yoon, T.H., Kim, S.J., Bulk micromachined submicroliter-volume PCR chip with very rapid thermal response and low power consumption, Lab Chip, 4, 401–407 (2004).

43. Wang, Q., Tan, Y., Gong, H., An integrated system for real-time PCR analysis based on microfluidic biochip, Int. J. Comp. Eng. Sci., 4(2), 285 –288 (2003).

44. Oda, R.P., Strausbauch, M.A., Huhmer, A.F.R., Borson, N., Jurrens, S.R., and Craighead, J., Infrared-mediated thermocycling for ultrafast polymerase chain reaction amplification of DNA, Anal. Chem., 70, 4361– 4368 (1998).

45. Ke, C., Berney, H., Mathewson, A., Sheeshan, M.M., Rapid amplification for the detection of Mycobacterium tuberculosis using a non-contact heating method in a silicon microreactor based thermal cycler, Sensors and Actuators B, 102(2), 308-314 (2004).

46. Issadore, D. , Humphry, K. J., Brown, K. A., Sandberg, L., Weitz, D. A., and Westervelt, R. M., Microwave Dielectric Heating of Drops in Microfluidic Devices, Lab Chip, 9, 1701–1706 (2009).

47. Guijt, R.M., Dodge, A., van Dedem, G.W.K., de Rooij, N.F., and Verpoorte, E., Chemical and physical processes for integrated temperature control in microfluidic devices, Lab Chip, 3, 1–4 (2003).

48. Erickson, D., Sinton, D., Li, D., Joule heating and heat transfer in poly(dimethylsiloxane) microfluidic systems, Lab Chip, 3, 141-149 (2003).

49. Grier, D.G., A revolution in optical manipulation , Nature, 424(6950, 810-816 (2003).

50. Chiou, P.Y., Ohta, A.T., and Wu, M.C., Massively parallel manipulation of single cells and microparticles using optical images , Nature, 436(7049), 370-372 (2005).

51. Chiou, P.Y., Ohta, A.T., Jamshidi, A., Hsu, H.Y., and Wu, M.C., Light-actuated ac electroosmosis for nanoparticle manipulation , J. of Microelectromechanical Systems, 17(3), 525-531 (2008).

52. Kumar, A., Kwon, J.S., Williams, S.J., Green, N.G., Yip, N.K., and Wereley, S.T., Optically modulated electrokinetic manipulation and concentration of colloidal particles near an electrode surface, Langmuir, 26(7), 5262-5272 (2010).

53. Yang, A.H.J., Moore, S.D., Schmidt, B.S., Klug, M., Lipson, M., and Erickson, D., Optical manipulation of nanoparticles and biomolecules in sub-wavelength slot waveguides, Nature, 475(7225), 71-75 (2009).

54. Terray, A. and Oakey, J. and Marr, D.W.M., Microfluidic control using colloidal devices, Science, 296(5574), 1841-1844 (2002).

55. Liu, G.L., Kim, J., Lu, Y., and Lee, L.P., Optofluidic control using photothermal nanoparticles, Nature Materials, 5(1), 27-32 (2005).

56. Krishnan, M., Park, J., and Erickson, D., Optothermorheological flow manipulation, Optics letters, 34(13), 1976-1978 (2009).

57. Psaltis, D. and Quake, S.R. and Yang, C., Developing optofluidic technology through the fusion of microfluidics and optics, Nature, 442(7101), 381-386 (2006).

58. Krishnan, M. and Erickson, D., Creating optically reconfigurable channel based microfluidic systems, IEEE Winter Topicals (WTM), 2011, , 103-104.

59. Arora, A., Simone, G., Salieb-Beugelaar, G.B., Kim, J.T., and Manz, A., Latest developments in micro total analysis systems, Anal. Chem., 82, 4830-4847 (2010).

60. D. Ross, T. J. Johnson and L. E. Locascio, Temperature measurement in microfluidic systems using a temperature dependent fluorescent dye, Anal. Chem., 73, 2509–2515 (2001).

6 List of Figures

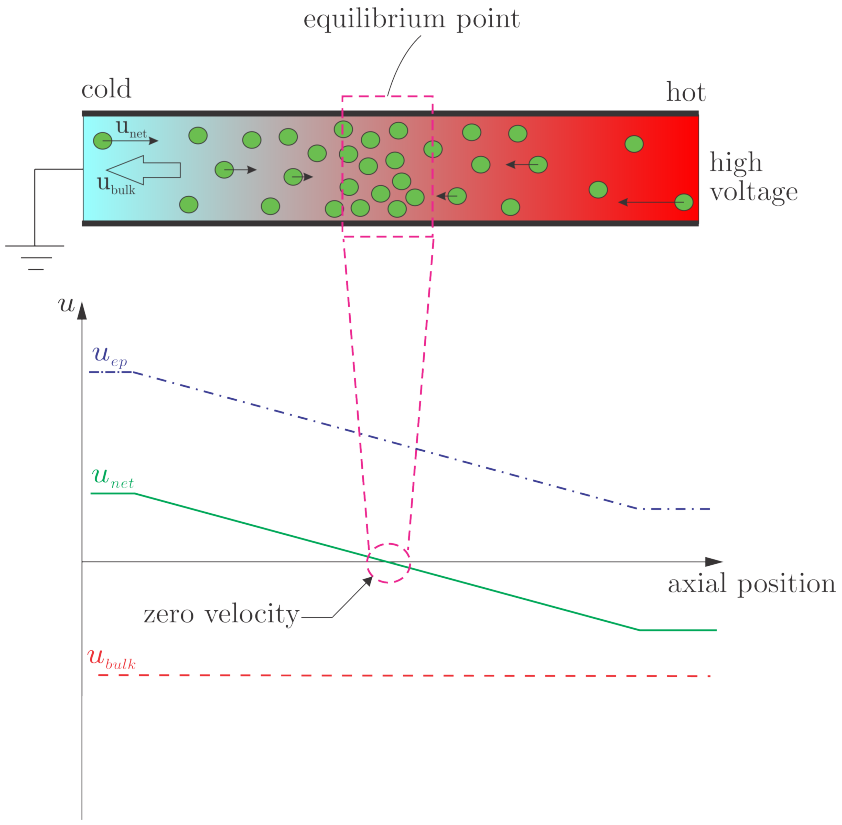

Fig. 1 Schematic illustration of temperature gradient focusing in a straight microchannel. A linear temperature gradient is produced with hot and cold regions on the right and left, respectively. By applying a high voltage, charged particles (depicted by green circles) move away from the ground electrode (to the right) with the electrophoretic velocity of u_{ep} while the bulk velocity is in the opposite direction. The electrophoretic velocity varies along the temperature gradient and is balanced by the constant bulk velocity at an equilibrium point where the net velocity becomes zero.

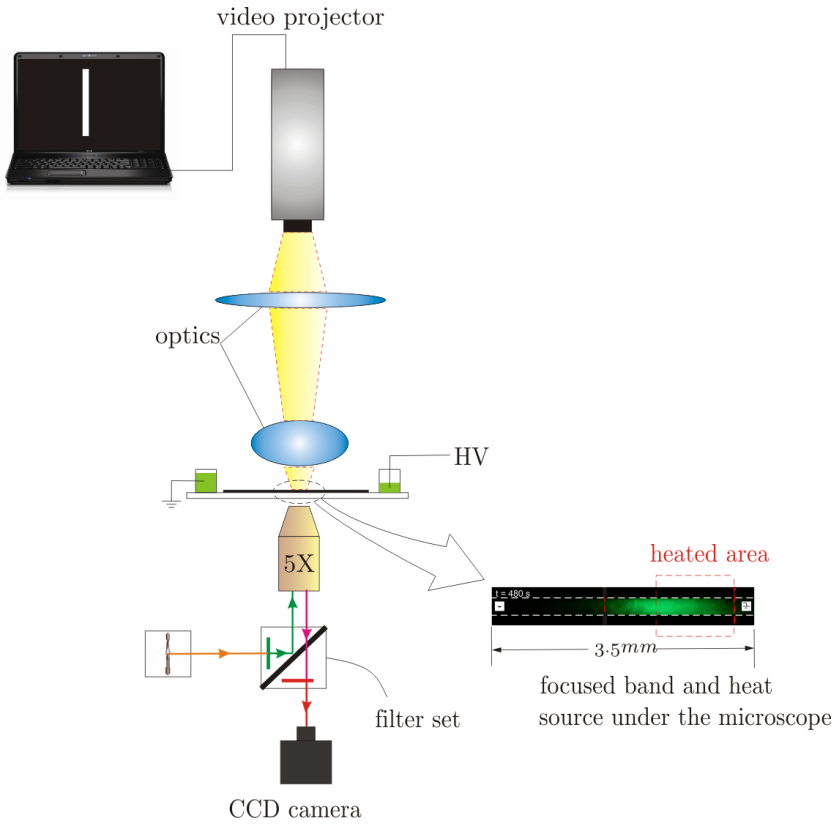

Fig. 2 Schematic of the experimental setup designed to optically control the local fluid temperature. The heater image is projected onto the surface of the microchannel providing a heated area with adjustable width. The temperature profile is used to increase the local concentration of sample analytes. Pressure control is accomplished by adjusting the relative heights of two external reservoirs. High voltage power supply is used to provide the appropriate electromigrative velocities.

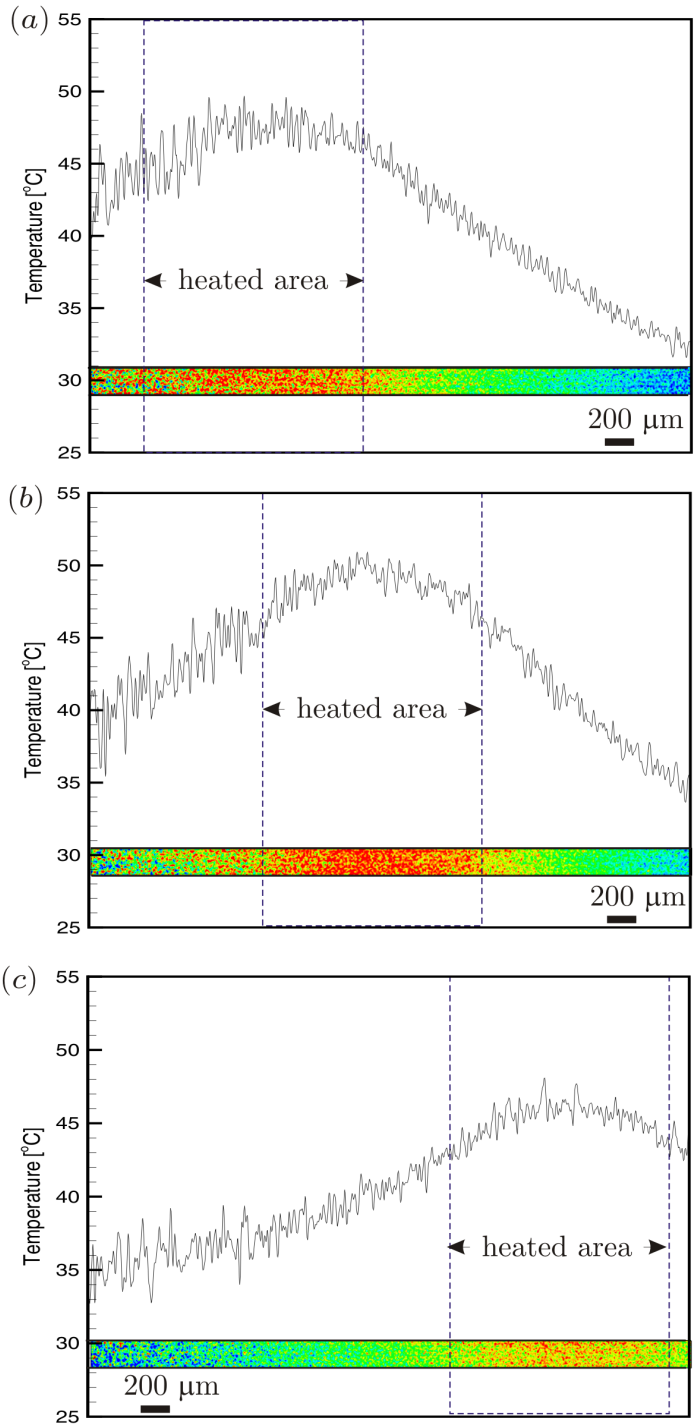

Fig. 3 Demonstration of heater location control and the resulting temperature field. The microchannel was heated at three different locations (a) left edge, (b) middle, and (c) right edge with the heater width of approximately 1.5 mm. The heater location was controlled by an external computer. Images were taken for the no flow condition and processed with the method described in Sec. 2.1. The total field of view for each image was 3.5 mm. Dashed rectangles indicate the location of the heated area. The temperature profile along the channel was obtained by taking the cross-sectional averaging at each axial location.

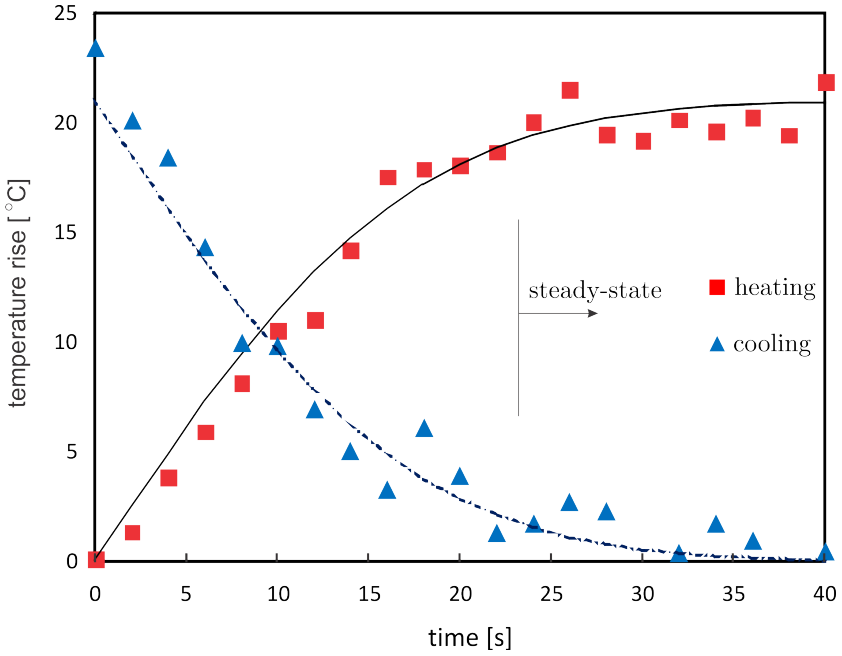

Fig. 4 Variation of maximum temperature, $T - T_{room}$, *vs.* time for a heater width of approximately 1.5 mm. Symbols represent the experimental data and the lines represent fitted curves. Each data point was obtained by finding the maximum temperature along the microchannel. Temperature at each axial location was obtained by taking the cross-sectional average.

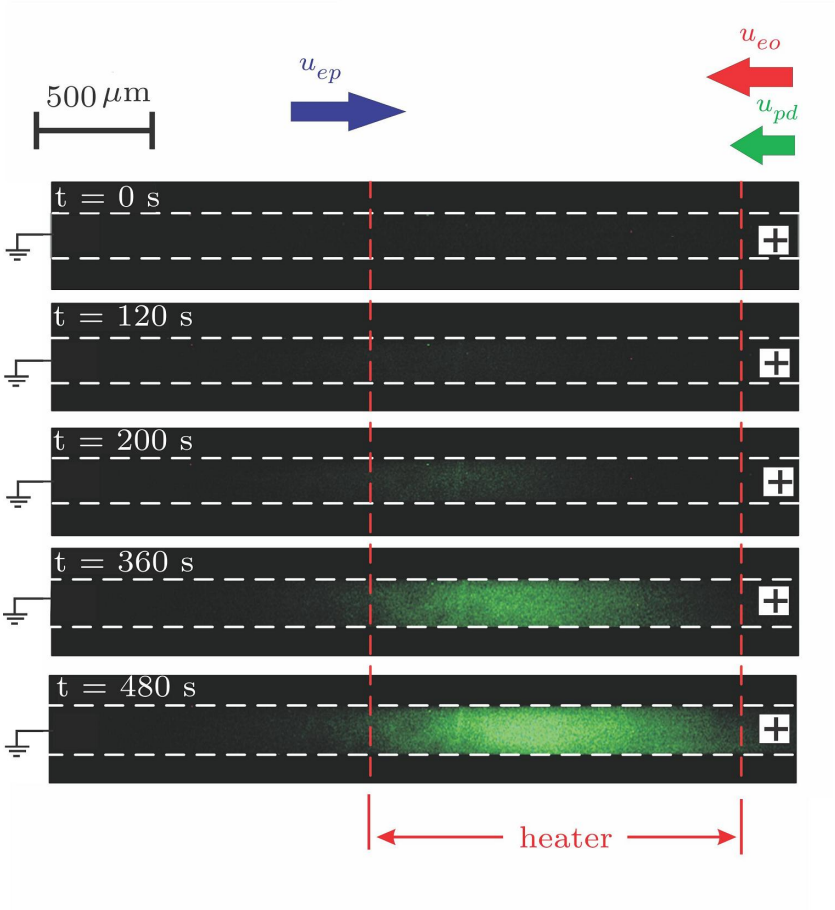

Fig. 5 Image sequence of fluorescein (green dye) focusing using the optothermal heating method. The applied electric field is 200 V/cm with positive polarity on the right and ground on the left. Pressure driven velocity (resulting from 25 mm-water hydrostatic head) is in favour of the electroosmotic flow from right to left. The electrophoretic velocity of fluorescein is from left to right.

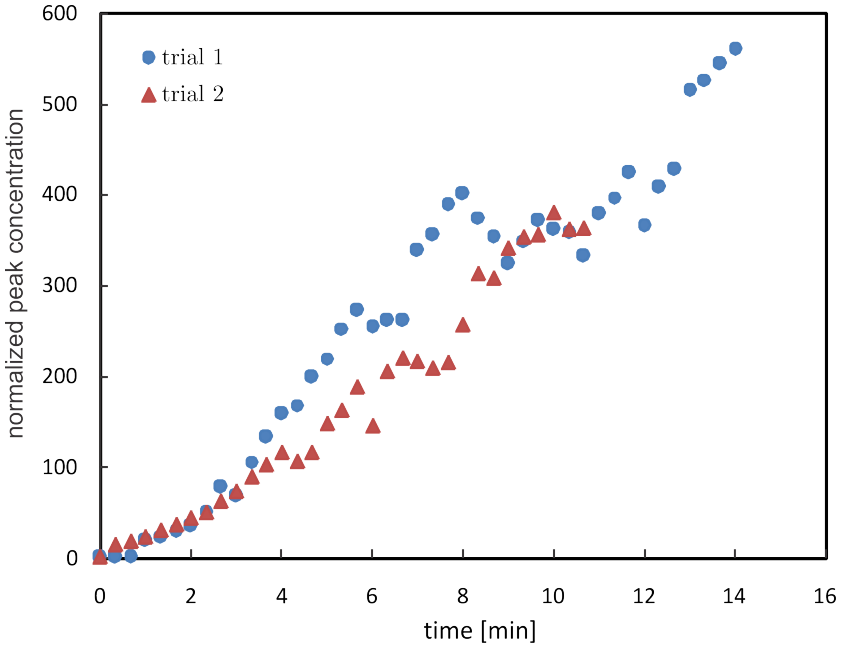

Fig. 6 Peak sample concentration versus time for two different focusing trials. The normalized concentration was calculated from the measured maximum fluorescence intensity at each time over the initial intensity. Almost 500fold enrichment was obtained within 15 minutes.

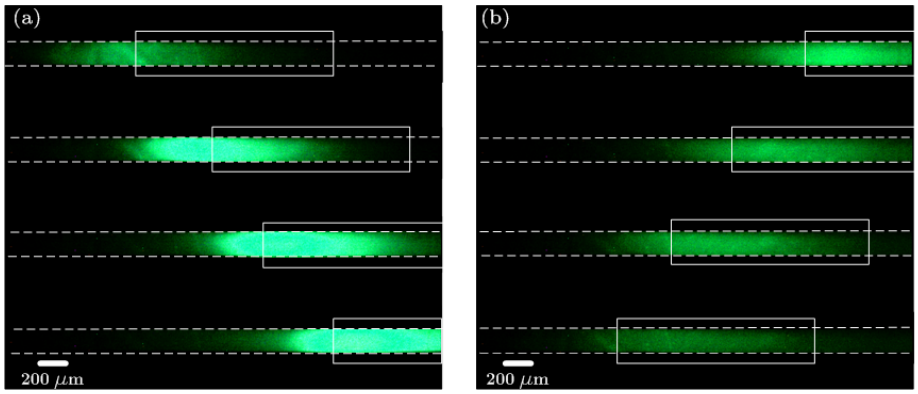

Fig. 7 Image sequence showing the on-demand transport of the focused band of fluorescein by moving the optothermal heater from: (a) left to right and (b) right to left. The heater location is indicated by a white rectangle. The applied electric field is 200 V/cm with positive polarity on the right and ground on the left reservoirs. A stable focused band was first generated at the start point (the stability was examined by processing a sequence of images taken every 2 seconds for 3 minutes) and then transported to the end point by adjusting the heater image. The direction and magnitude of the pressure driven flow was kept constant (pressure was resulting from approximately 25 mm of water hydrostatic head) and from right to left) during the experiment. Movies showing the controlled translation of the analyte band are available in supporting information.

Appendix B

Optothermal control of local fluid temperature in microfluidics

The optothermal heating system utilized in Appendix A is described in more details in this section. Figure B.1 shows the optothermal heating system under process. Main components of the optothermal heating system are listed in Table B.1. Thermal performance of the proposed optothermal heating system has been assessed by performing *in situ* temperature field imaging based upon the temperature-dependent quantum efficiency of rhodamine B. Briefly, 0.1 mM rhodamine B in 900 mM Tris-borate buffer solution was prepared and introduced into the microchannel. A background and an isothermal "cold field"intensity image of the system were taken prior to each experiment. Following the acquisition of the cold field image, the prescribed pressure driven flow was set and a rectangular strip of light was projected on the surface of the black tape to provide a localized heating. The heat source width was measured to be approximately 1.5 mm. Images were taken every 2 seconds with the resolution of 1280×1024 pixels, spanning a length of 5 mm of the channel.

To extract the in-channel temperature profiles, background image was first subtracted from each raw image and the cold field image. The corrected raw images were then normalized with the corrected cold field images. The intensity values of the treated images were then converted to temperature using the intensity vs. temperature calibration using a calibration curve obtained as follows: a PMMA reservoir containing approximately 0.1mL Rhodamine B dye ($100\,\mu$M in Tris-Borate buffer) was fabricated using a laser system

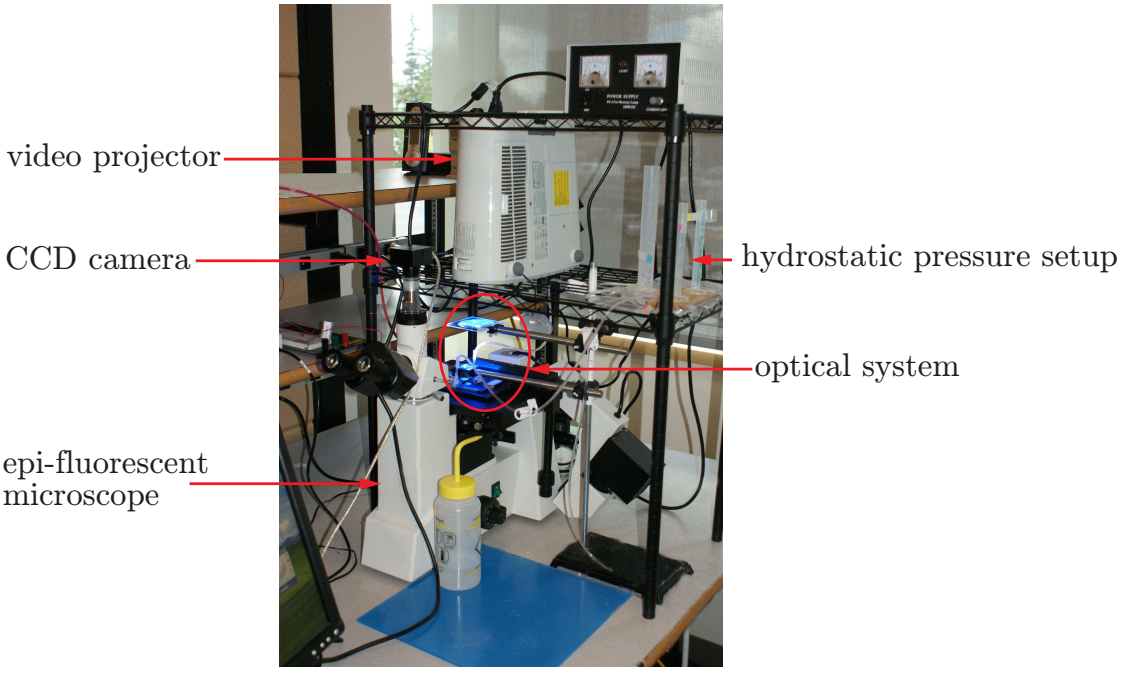

Figure B.1: Optothermal heating and analyte manipulation system under process.

(Universal Laser System's VersaLASER©) with an embedded k-type thermocouple. The voltage read by the thermocouple was then recorded by Labveiw 8.5 software (National Instruments, USA) via a standard data acquisition card (National Instruments, $16-$bit, $250KS/s$). Initially the reservoir was loaded with dye solution at room temperature and the entire system was heated to approximately 70 ° C. The system was allowed to cool in air while intensity images were taken at specified intervals and the data acquisition system recorded the instantaneous thermocouple readings. A low-pass filter was employed to cut off the high frequency noises in the thermocouple readings. Random locations close to the thermocouple in the calibration images were then selected and the intensities at each point were normalized such that an intensity of 1 corresponded to room temperature (i.e., 26°C). The final results are shown in Figure B.2. Since the capillary height is much smaller than other length scales of the system, the temperature difference in the depth direction is small and the monitored two-dimensional fluorescent intensity accurately represents the temperature field of the fluid within the microchannel.

The ability of the system to control the local fluid temperature in the microchannels

Table B.1: Main components of the optothermal heating setup.

component	specifications	comments
video projector	Sony, 3-LDC BrightEra, 190 W Mercury lamp1600/2000 ANSI lumens	• video projector is controlled by an external laptop
epi-fluorescent microscope (Jenco, Oregon)	• illumination: 100 W, mercury lamp • 5X, 0.12 N.A. objective is used in all experiments. • filter sets: Red (Ex. 546 nm/ Em. 600 nm) Green (Ex. 540 nm/ Em. 580 nm) • CCD camera: 5 Mega pixel, 20 frame/s • image acquisition software: Zarbco video (Ver. 1.65)	• microscope is modified for this experimental setup
PD flow control system	• syringe pump (Harvard Apparatus, QC, Canada) • hydrostatic pressure	• syringe pump is only used for thermal measurements • hydrostatic pressure is used for ultra-small • flow rates (i.e. $Q < 10\mu\text{L/hr}$)
high voltage power supply (Spellman, CZE 1000R)	voltage ranging from $0-30$ KV	• DAQ card ($16-$bit, 250 KS/s) is used to collect voltage and current data and to control the output voltage of the power supply • Labview (NI, USA) is used for data recording
optics (Edmund optics, NJ)	Fresnel lens, convex lens	
microchip assembly	glass capillary (Vitrocom), PMMA substrate	-see the text for more details

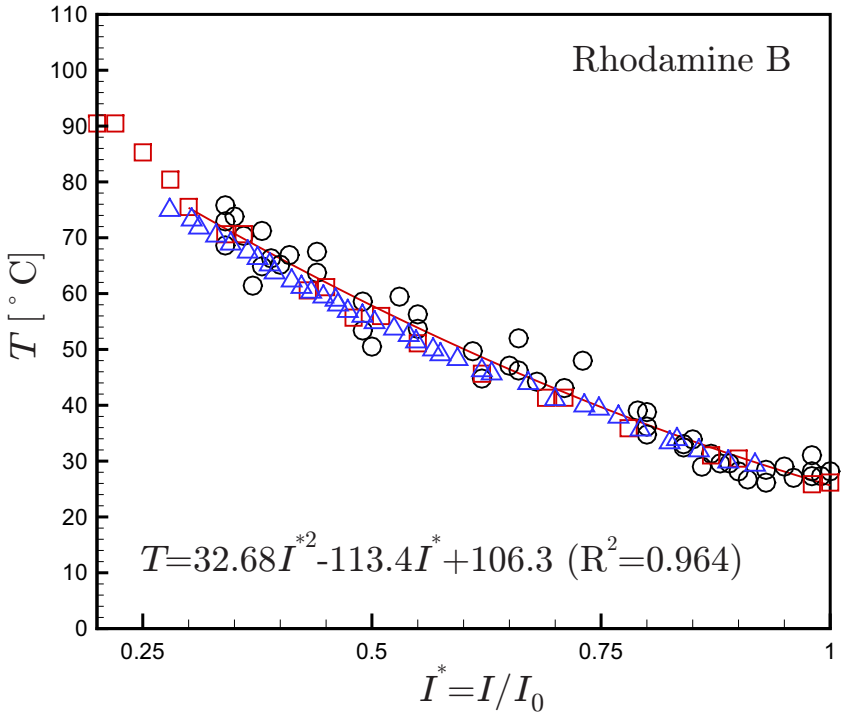

Figure B.2: Measured temperature as a function of normalized fluorescence intensity of rhodamine B dye. Fluorescent intensity is normalized with respect to room temperature (T=26 $^{\circ}C$). Data obtained from present work, circular symbols, are comparred against those of collected from Ross et al. [1], square symbols, and Erickson et al. [2], delta symbols. The Solid line represents a second order polynomial fit to the present data.

and the thermal response of the system are plotted in Appendix A (Figs. 3 and 4). Here the effects of heater width, light intensity and fluid velocity on the temperature distribution are provided. Figure B.3 presents the variation of maximum temperature rise along the microchannel with the heat source width and power. In Figure B.3-a, the source power is kept constant and the effect of source width is investigated. The source width and maximum temperature rise are normalized with respect to those of a heat source with the width of 1.5mm. The results suggest that a the maximum temperature rise varies linearly with the source width. In Figure B.3-(b), the heat source width is kept constant holding the value of 1.5mm and the source power is changed by adjusting the darkness of the image. The results

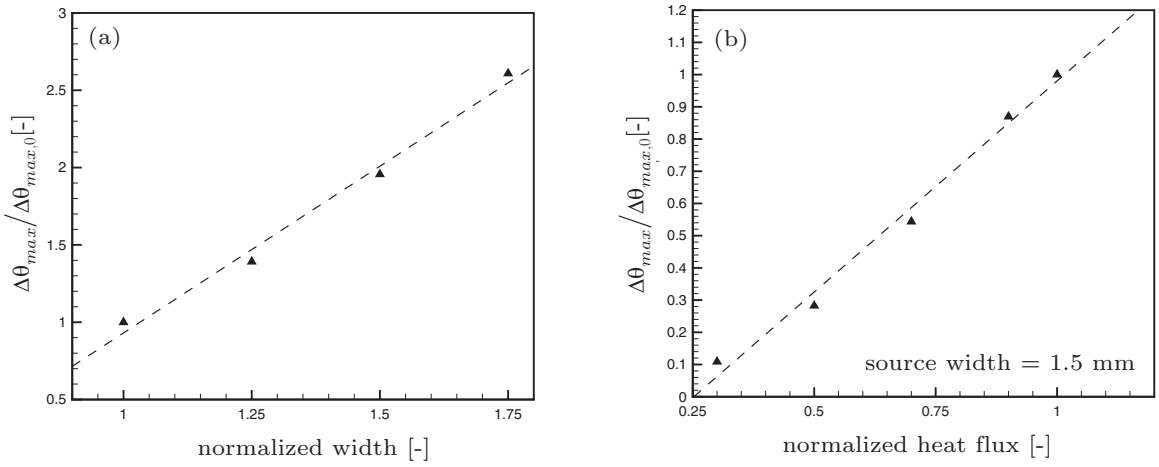

Figure B.3: Effect of the source width and power on the maximum temperature rise within the microchannel for no flow condition; (a) the source power is kept constant and the width and maximum temperature rise are normalized with respect to a heat source with the width of 1.5mm; (b) the heat source width is kept constant holding the value of 1.5mm and the source power is changed by adjusting the darkness of the image. Symbols represent the experimental data and the dashed lines are linear fits.

are obtained for no flow condition. The width and maximum temperature rise are normalized with respect to the width and maximum temperature rise of the heat source of 1.5mm width. As expected, since more heat is transferred to the fluid, maximum temperature increases with the source width in a linear behavior. Fairly linear variation of normalized temperature rise can be observed against the normalized heat flux.

In order to investigate the effects of fluid velocity on the temperature field, the variation of temperature distribution along the microchannel for different Peclet numbers is shown in Figure B.4. The temperature at each axial location is obtained by cross-sectional averaging of the measured temperature. The axial direction is normalized with respect to the heat source width. For the no-flow condition (very small flow rates), conduction makes the major contribution to the heat transfer within the fluid flow and the convective heat transfer is negligible. By increasing the flow rate, cold fluid from the upstream of the flow is pumped into the heated area, thus the overall temperature drops and the location of maximum temperature shifts to the downstream of the heat source. In the specific case shown in Figure

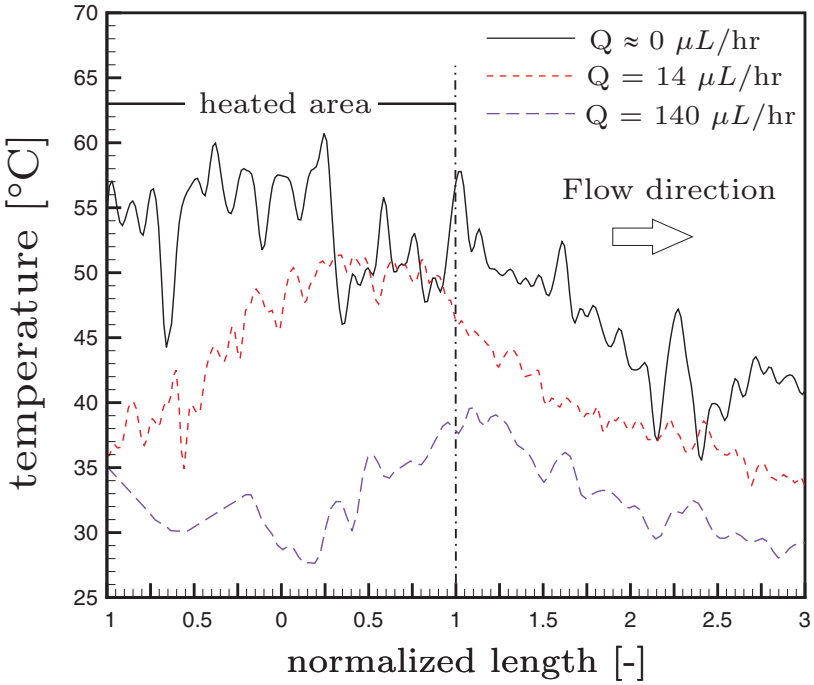

Figure B.4: Variation of temperature distribution along the channel at various flow rates. Temperature at each axial location is obtained by cross-sectional averaging of the temperature. The source width holds the value of 1.5mm. The axial direction is normalized with respect to the heat source width.

B.4, for flow rates as high as of 140μL/hr (which corresponds to the Peclet number of 60), the entire heat that enters the fluid is washed with the cold of fluid through convection.

Bibliography

[1] D. Ross, M. Gaitan, L.E. and Locascio, L.E., Temperature measurement in microfluidic systems using a temperature-dependent fluorescent dye, Anal. Chem. 73 (2001) 4117–4123.

[2] D. Erickson, D. Sinton, and D. Li, Joule heating and heat transfer in poly (dimethylsiloxane) microfluidic systems, Lab on Chip 3 (2003) 141–149.

Appendix C

Geometrical effects on the temperature distribution in a half-space due to a moving heat source

(with permission from ASME)

Geometrical Effects on the Temperature Distribution in a Half-Space Due to a Moving Heat Source

Mohsen Akbari[1]
Mechatronic Systems Engineering,
School of Engineering Science,
Simon Fraser University,
Surrey, BC, V3T 0A3, Canada
e-mail: mohsen_akbari@sfu.ca

David Sinton
Department of Mechanical Engineering,
University of Victoria,
Victoria, BC, V8W 2Y2, Canada

Majid Bahrami
Mechatronic Systems Engineering,
School of Engineering Science,
Simon Fraser University,
Surrey, BC, V3T 0A3, Canada

Fundamental problem of heat transfer within a half-space due to a moving heat source of hyperelliptical geometry is studied in this work. The considered hyperelliptical geometry family covers a wide range of heat source shapes, including star-shaped, rhombic, elliptical, rectangular with round corners, rectangular, circular, and square. The effects of the heat source speed, aspect ratio, corners, and orientation are investigated using the general solution of a moving point source on a half-space and superposition. Selecting the square root of the heat source area as the characteristics length scale, it is shown that the maximum temperature within the half-space is a function of the heat source speed (Peclet number) and its aspect ratio. It is observed that the details of the exact heat source shape have negligible effect on the maximum temperature within the half-space. New general compact relationships are introduced that can predict the maximum temperature within the half-space with reasonable accuracy. The validity of the suggested relationships is examined by available experimental and numerical data for the grinding process, for medium Peclet numbers. For ultrafast heat sources, an independent experimental study is performed using a commercial CO_2 laser system. The measured depth of the engraved grooves is successfully predicted by the proposed relationships.
[DOI: 10.1115/1.4003155]

Keywords: moving heat source, half-space, temperature distribution, arbitrary geometry, modeling

1 Introduction

The problem of stationary and moving heat sources applies to many fields of engineering such as metal cutting, spot welding, laser cutting, laser surface treatment, friction between mechanical parts, and tribological applications including ball bearing and gear design [1–5]. In many circumstances, the size of the heat source compared to the conducting body is small enough that a heat source on a half-space assumption can be made. There are many studies in the literature that focused on finding the transient and quasi-steady temperature distribution within a half-space due to a moving heat source; examples are listed in Table 1.

Among the available references, there are few that deal with various geometric shapes of heat sources [6–8]. Tian and Kennedy, Jr. [6] used a combination of point source solution [9] and the Green's function method to develop accurate correlations for the circular and square heat sources. These correlations were used to formulate models for predicting flash temperatures (i.e., maximum surface temperature) in sliding asperities for any speed. Using the classical point solution, Hou and Komanduri [7] developed a general solution for elliptical and rectangular heat sources with different heat flux intensities of uniform, parabolic, and normal. Their method requires different length scales and constant parameters for different geometries to compute the temperature distribution within a half-space. Muzychka and Yovanovich [10] showed that the thermal resistance of a moving heat source is a weak function of source shape if the square root of the heat source area is selected as a characteristic length scale in all calculations. Based on this argument and using the solutions for stationary and ultrafast heat sources, they [10] proposed a general solution to predict the thermal resistance of a moving heat source of arbitrary shape. Most recently, Laraqi et al. [8] used the Fourier transform to investigate the maximum contact temperature for three configurations: (i) rectangular source on a rectangular prism, (ii) elliptic source on a rectangular prism, and (iii) eccentric circular source on a rotating cylinder. By varying the values of geometric parameters in the provided solutions, they [8] proposed a solution for various particular cases such as strip, rectangular, square, elliptic, and circular moving heat sources.

Present work discusses various aspects of the fundamental problem of heat transfer within a half-space due to a moving heat source of arbitrary shape. This paper has two objectives: (i) perform a systematic study on the relevant geometrical parameter effect on the maximum temperature within a half-space due to a moving heat source of arbitrary but symmetrical shape (this will eventually lead to simplified models for an arbitrarily shaped moving heat source) and (ii) present new compact relationships for the hyperelliptical family of heat sources, which provide analytical-based compact solutions that are essential for basic designs, parametric studies, and optimization analyses required for many engineering applications. The hyperelliptical geometry is considered since it covers a wide variety of symmetrical shapes including the star-shaped, rhombic, elliptical, circular, rectangular, and squared. The proposed model is validated with numerical and experimental data from different studies for rectangular and square geometries. Moreover, a CO_2 laser system is used to engrave grooves on wooden substrates over a wide range of laser power and the beam speed. Measured depth are compared against those predicted by the theory presented in this work with acceptable accuracy.

2 Theory

Figure 1 schematically shows the geometry of a symmetrical moving heat source of arbitrary shape on a half-space. The mathematical problem consists in finding the solution for temperature rise defined as $\theta = T(R,t) - T_0$, where T_0 is a reference temperature, for any point in the moving coordinate of $(X = x - Ut, y, z)$ to the three dimensional diffusion equation with constant thermal properties (see Fig. 1) [11],

$$\nabla^2\theta - \frac{U}{\alpha}\frac{\partial\theta}{\partial X} = \frac{1}{\alpha}\frac{\partial\theta}{\partial t}$$

Initial condition:

$$\theta = 0, \quad t = 0 \quad \text{everywhere}$$

[1]Corresponding author.

Contributed by the Heat Transfer Division of ASME for publication in the JOURNAL OF HEAT TRANSFER. Manuscript received February 26, 2010; final manuscript received November 24, 2010; published online March 2, 2011. Assoc. Editor: Oronzio Manca.

Table 1 Summary of previous studies on moving heat source in the literature

Author	Year	Method	Source shape	Heat flux	Comments
Carslaw and Jeager [9]	1959	A	Point, line, and infinite strip	Uniform	- Introduced the heat source approach.
Takazawa [26]	1966	N	Infinite strip	Uniform	- Approximate relationship for the maximum temperature rise within a half-space as a function of Peclet number. - Width of the source in the moving direction as a length scale.
Paek and Gagliano [27]	1972	A/E	Circle	Uniform	- Half-space and finite body. - Instantaneous point source method. - Transient solution in the form of the modified Bessel function of first kind. - Integral over the surface of the heat source is numerically solved.
Weichert and Schonert [12]	1978	A	Line, plane, and cube	Uniform	- Exponential transformation is used. - Effect of aspect ratio and source speed are numerically investigated.
Eager and Tsai [28]	1983	A/E	Circle	Gaussian	- Superposition of instantaneous point sources with different powers. - Single integral that is solved numerically. - Heat source radius as the length scale.
Terauchi et al. [13]	1985	A	Rectangle, square, and circle	Uniform/parabolic	- Single and double heat sources. - Effect of the aspect ratio is investigated. - Width of the source in the moving direction and source radius as the length scale for rectangular and circular heat sources, respectively.
Zhang [29]	1990	A	Thin rod and infinite plane	Uniform	- Transient solutions for 1D problem in an infinite body.
Tian and Kennedy, Jr. [6]	1995	A	Ellipse/rectangle	Uniform/parabolic	- Green's function method and point source method are used. - Maximum and average surface temperatures are obtained for the entire range of Peclet numbers. - Length scale is the diameter/width of the circular/square source.
Manca et al. [30]	1995	A	Circle	Gaussian	- Three dimensional problem in a finite body is solved using Green's function method. - Source radius as the length scale.
Yevtushenko et al. [31]	1997	A	Circle	Uniform	- Transient problem is solved using a finite Fourier transform. - Final solution is in the form of an infinite integral of the Bessel functions of first and second kinds. - Source diameter as the length scale.
Zeng et al. [32]	1997	A	Cylinder (thin rod)	General	- General transient solutions in the form of an infinite series.
Zubair and Chaudhry [33,34]	1996/1998	A	Point source and infinite plane	Uniform but time dependent	- Transient problem is solved.
Kato and Fujii [35]	1997	E	Infinite strip	Uniform	- Temperature measurement using PVD films. - Maximum temperature rise for different grinding wheel materials is reported at different locations within the workpiece. - Source width as the length scale.
Kaebernick et al. [36]	1999	A/E	Circle	Gaussian	- Pulsed laser is considered. - Proposed models are in the form of double integrals.
Neder et al.[37]	1999	N	Circle	Uniform	- Finite element method is used. - Source diameter as the length scale and entire range of Peclet numbers are investigated.

Table 1 (***Continued.***)

Author	Year	Method	Source shape	Heat flux	Comments
Hou and Komanduri [7]	2000	A	Ellipse/rectangle	Parabolic, uniform, and normal	- General solution based on the point source method is proposed. - Final solution in the form of triple integrals. - Different length scales are used for different source shapes. - Approximate relationship is proposed elliptical heat source and uniform and normal flux.
Xu and Malkin [25]	2001	E	Infinite strip	Uniform	- Comparison between three different grinding temperature measurement techniques.
Muzychka and Yovanovich [10]	2001	A	Arbitrary shape	Uniform, parabolic, isothermal	- Thermal resistance for arbitrary shape contacts is investigated. - Approximate relationship is proposed for uniform and parabolic distribution square root of source area as the length scale.
Vick and Furey [24]	2003	A	Square	Uniform	- Single and multiple heat sources are considered. - Surface temperature distribution is reported for 20 different materials. - Width of the source as a length scale.
Baïri [38]	2003	A	Circle	Uniform	- Thermal resistance due to moving multiple sources. - Two layer half-space is studied. - Models are in the form of double series. - Source diameter as the length scale.
Laraqi et al. [8]	2004	A	Ellipse/rectangle	Uniform	- Three configurations are investigated: (i) rectangular source on a rectangular prism, (ii) elliptic source on a rectangular prism, and (iii) eccentric circular source on a rotating cylinder. - Fourier transform is used. - Square root of the source area as a length scale for the dimensionless temperature and source major axis/width along the moving direction for Peclet number.
Li et al. [39]	2004	A/N/E	Circle	Gaussian	- Volumetric and surface heating are compared for quasi-steady solution. - Green's function method is used. - Source diameter as the length scale.
Kuo and Lin [40]	2006	A	Rectangle	Uniform	- Temperature distribution due to the grinding process is investigated.
Bianco et al. [41]	2006	N	Circle	Gaussian	- Transient temperature distribution is solved using the FE method.
Wen and Khonsari [42]	2007	A	Infinite strip	Uniform/ oscillatory	- 2D temperature distribution due to an oscillatory heat flux is obtained using Duhamel's theorem and finite element method.
Levin [43]	2008	A	Line/circle	Uniform, Gaussian	- General solution using the method of images is obtained for quasi-steady solution. - Trailing temperature is well captured by this method. - Final solution in the form of the green function and double integrals.
Laraqi et al. [44]	2009	A	Circle	Uniform	- Governing equations are solved for both a circular pin and a rotating disk. - Fourier and finite Henkel integral transforms are used. - Source diameter as the length scale.
Xu et al. [45]	2010	A/N/E	Square	Uniform	- Laser quenching of cylindrical workpiece is investigated based on the point source method is proposed. - FE numerical validation is performed followed by experiments using a CO_2 laser system.

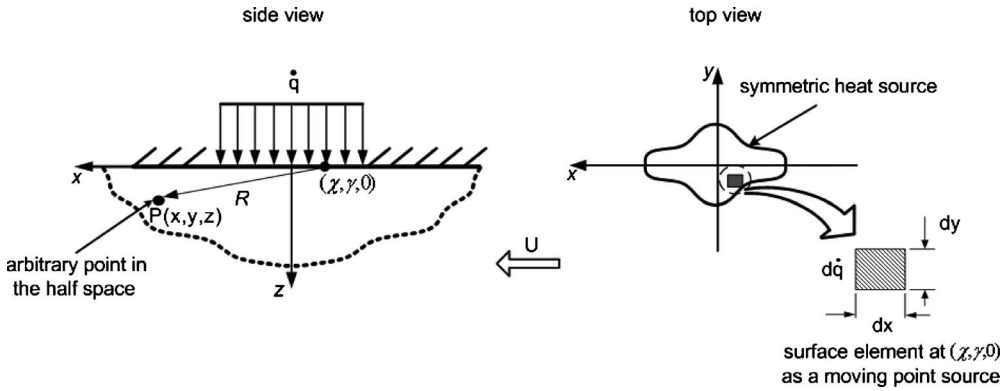

Fig. 1 Schematic of a symmetrical moving plane heat source with arbitrary shape

Boundary conditions:

$$-k\left(\frac{\partial\theta}{\partial z}\right)_{z=0} = \dot{q} \quad \text{(on the heat source)}$$

$$-k\left(\frac{\partial\theta}{\partial z}\right)_{z=0} = 0 \quad \text{(elsewhere)}$$

$$T_{x,y,z\to\infty} = 0 \tag{1}$$

The solution to Eq. (1) for a hyperelliptical heat source defined as $(X^*/\alpha^*)^n+(y^*/b^*)^n=1$, can be obtained by superposition of point sources [7,12] over the heat source area in the dimensionless moving coordinate of $(X^*=X/\mathcal{L}, y^*=y/\mathcal{L}, z^*=z/\mathcal{L})$

$$\theta^* = \int_{-a^*}^{a^*} \int_{-\varepsilon_m a^*[1-(\chi/a^*)^n]^{1/n}}^{\varepsilon_m a^*[1-(\chi/a^*)^n]^{1/n}} \frac{e^{-\mathrm{Pe}(X^*-\chi^*)}}{4\pi R^*} \left\{ e^{\mathrm{Pe}R^*}\,\mathrm{erfc}\left(\frac{R^*}{2\sqrt{\mathrm{Fo}}} + \mathrm{Pe}\sqrt{\mathrm{Fo}}\right) + e^{-\mathrm{Pe}R^*}\,\mathrm{erfc}\left(\frac{R^*}{2\sqrt{\mathrm{Fo}}} - \mathrm{Pe}\sqrt{\mathrm{Fo}}\right)\right\} d\gamma^* d\chi^* \tag{2}$$

where a^* and b^* are the dimensionless major and minor axes, n determines the shape of the geometry (see Fig. 2), $\theta^*=\theta k/\dot{q}\mathcal{L}$, $\mathrm{Pe}=U\mathcal{L}/2\alpha$, $\mathrm{Fo}=\alpha t/\mathcal{L}^2$, $\mathcal{L}$ is the characteristic length, and $R^*=\sqrt{(X^*-\chi^*)^2+(y^*-\gamma^*)^2+z^{*2}}$. The hyperellipse yields many special cases by setting the values of n and the aspect ratio $\varepsilon_m=b/a$. Therefore, the solution developed for the hyperellipse can be used to analyze a variety of geometries, including star shapes, ellipses, circles, rectangles, squares, diamondlike geometries, and line sources. Note that ε_m accounts for the effect of the heat source orientation and can have any value in the range of $0<\varepsilon_m<\infty$.

Selection of the characteristic length, $\mathcal{L}$, is an arbitrary choice and can be defined for each geometry individually. For instance, for a circular or square source, the best choices are the source diameter and width, respectively [6]. For an elliptical or rectangular source, on the other hand, the axis of the source in the moving direction can be selected as the length scale [7,13]. When dealing with an arbitrary geometry, it is essential to select an appropriate length scale to obtain more consistent results. It is demonstrated [14,15] that for stationary heat sources when the square root of the heat source area, $\sqrt{A}$, is chosen as the characteristic length scale, similar trends for various heat source shapes are obtained. We examined this length scale (i.e., $\sqrt{A}$) for moving heat sources later by using $\mathcal{L}=\sqrt{A}$, consistently throughout the present analysis.

A closed form solution for Eq. (2) cannot be found even for simple geometries such as ellipse or rectangle; thus, we solved it numerically. An in-house computational code is developed in MAPLE 11 [16] to solve the double integral in Eq. (2). To ensure that the same heat flow rate enters the half-space for different geometries, the total source area is kept constant throughout the

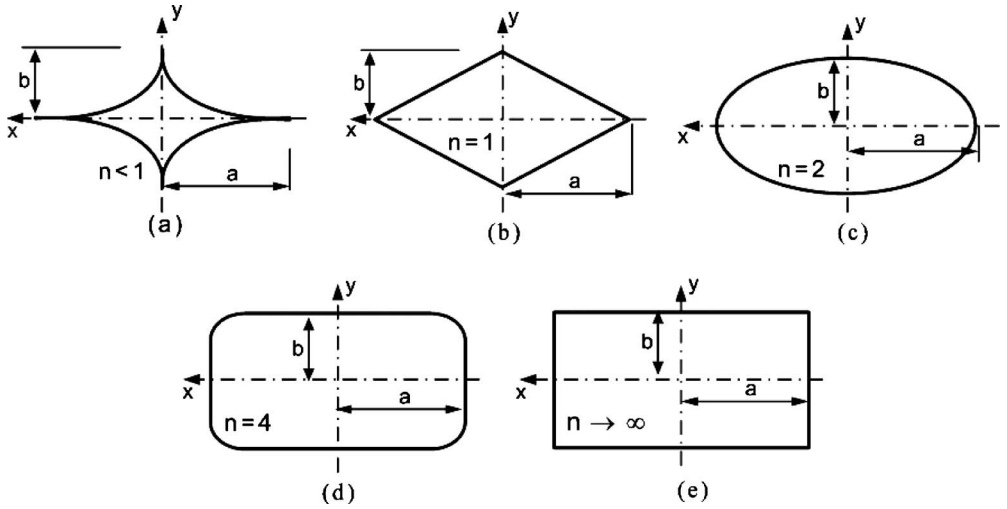

Fig. 2 Hyperellipse as a general symmetric geometry covers an array of source geometries: (*a*) star shape (n<1), (*b*) rhombic (n=1), (*c*) elliptical (n=2), (*d*) rectangular with round corners (n=4), and (*e*) rectangular (n→∞)

entire analysis. It should be noted that in Eq. (2), quasi-steady condition is achieved very fast (e.g., for a typical value of Pe $=10$, the transition times for the steady-state condition for a 1×1 mm^2 square heat source are 20 ms and 400 ms for stainless steel and wood, respectively). Hence, in most applications, it can be assumed that the quasi-steady condition is reached very fast; thus, only steady-state condition is considered though this work.

3 Experimental Study

3.1 Test Procedure. Grooves were ablated in wooden (red oak) surfaces using a CO_2 laser system (Universal Laser system, model VSL 3.60, Scottsdale). The system has a CO_2 laser cartridge rated at a maximum power of $60 \pm 10\%$ W that produces an invisible continuous infrared beam at a wavelength of 10.6 μm. The movement of the mirrors and lens assembly is achieved by a motor and controlled by an operating software. The laser system works with vector and raster modes to produce lines and filled shapes, respectively. The system was set to vector mode for single pass ablation in this work. Laser power and speed were set as a percentage of maximum using the laser control software. The system was rated to run at the maximum raster beam speed of 255 mm/s $\pm 2\%$ (45 in./s) according to the manufacturer. Since the maximum vector mode speed was lower than the raster mode, the beam speed in the vector mode was determined by measuring the amount of time required for the beam to engrave a straight line with a specific length. The focal length of the lens was 50.8 mm $\pm 4\%$ (2 in.), which according to the manufacturer specifications generated a circular spot size of 127 μm $\pm 4\%$ (0.005 in.). The laser was focused by controlling the "z" position of the workstation for different material thicknesses. The measurement showed that the percentage system changed the beam speed proportionally with respect to the maximum speed, which corresponds to the Peclet number of Pe $=130 \pm 12\%$.

Commercial red oak was purchased with the thickness of 7 mm $\pm 8\%$ and was cut to form rectangular 30×60 mm^2 substrates. Red oak was used because of its opacity, with an absorption coefficient of $0.91 \pm 5\%$ [17] at the wavelength of 10.6 μm. Moreover, red oak does not melt during the pre-ignition process, and its radiative ignition temperature is available in the literature [17–20]. The opacity of the material helps to assume that the external radiation is absorbed at the surface of the substrate. The substrate width and height were large enough to ensure the half-space assumption. Following the laser exposure, the channel depth was determined by taking the images of channel cross-section using a charge coupled device (CCD) camera mounted on an inverted microscope (Unitron, Commack, NY) at the magnification of 10×. Figure 3 shows the schematic diagram of the laser beam, the engraved groove, and the cross-sectional image of the wooden substrate (red oak) following laser exposure at the typical relative beam speed of $U^*=U/U_{\max}=0.6$ and relative power of $P^*=P/P_{\max.}=0.4$. Images were analyzed in the image processing software (ScopePhoto 2.0) in which each pixel is calibrated using a 20 line/mm optical ruler (Edmund Optics, Barrington, NJ). Laser ablation of red oak is a complicated process that includes production of char and endothermic decomposition [19,21]. However, these effects are not considered in this work, and the surface of each channel is assumed to be an isotherm with the red oak burning temperature of θ_b. This simplification is shown to be valid for a wide range of beam speed and laser power.

3.2 Uncertainty Analysis. The groove depth, d_g, is a complex function of laser power, $\dot{q}$, beam speed, U, spot size, d_s, thermal diffusivity, α, and absorption coefficient, ω. The maximum uncertainty for the groove depth measurements can be calculated from [22]

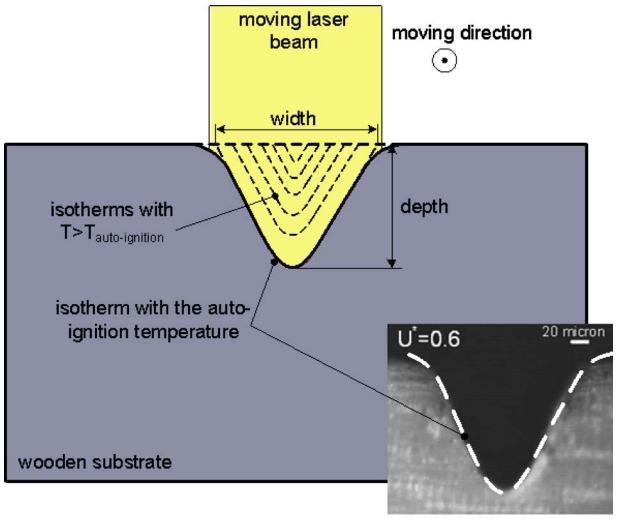

Fig. 3 Schematic diagram of the laser beam, the engraved groove, and cross-sectional image of the wooden substrate (red oak) following laser exposure at the typical relative beam speed of $U^*=U/U_{max}=0.6$ and relative power of $P^*=P/P_{max.}=0.4$. Image is taken by an inverted microscope (Unitron, Commack, NY) with a 10× magnification.

$$\frac{\delta d_g}{d_g} = \sqrt{\left(\frac{\delta \dot{q}}{\dot{q}}\right)^2 + \left(\frac{\delta U}{U}\right)^2 + \left(\frac{\delta d_s}{d_s}\right)^2 + \left(\frac{\delta \alpha}{\alpha}\right)^2 + \left(\frac{\delta \omega}{\omega}\right)^2} \quad (3)$$

With the maximum estimated uncertainties of the relevant parameters listed in Table 2, the maximum uncertainty is estimated to be $\pm 13.9\%$.

4 Parametric Study and Approximate Models

The influence of the relevant important parameters on the temperature distribution due to a moving plane source is investigated. The effects of the shape parameter, n, the heat source aspect ratio, ε_m, and the source speed (Peclet number, Pe), on the temperature field within the half-space at quasi-steady condition are discussed in detail in the following subsections. The trends of the results are studied for a range of each parameter, while the remaining parameters are held constant. The heat source area is kept constant through the entire study to ensure that the same heat flow enters the half-space.

4.1 Shape Parameter, n. The variation in the maximum temperature, $\theta^*_{\max}$, within the half-space with respect to the shape parameter, n, is plotted in Fig. 4 for two typical values of aspect ratios: $\varepsilon_m=0.1$ and 0.5 and Peclet number of Pe $=10$. The solid lines represent the mean values of calculated results. As can be seen, the effect of the heat source corners on the maximum temperature is small (within $\pm 2\%$ of the average value) and thus can be neglected.

4.2 Aspect Ratio, ε_m. Figure 5 shows the variation in the maximum temperature, $\theta^*_{\max}$, with aspect ratio on the surface of a rectangular heat source for different values of Peclet number. For

Table 2 Estimated uncertainty of involving parameters in the analysis

$\delta\dot{q}/\dot{q}$	$\delta U/U$	$\delta d_s/d_s$	$\delta\alpha/\alpha$	$\delta\omega/\omega$
11.1%	2%	3.9%	5%	5%

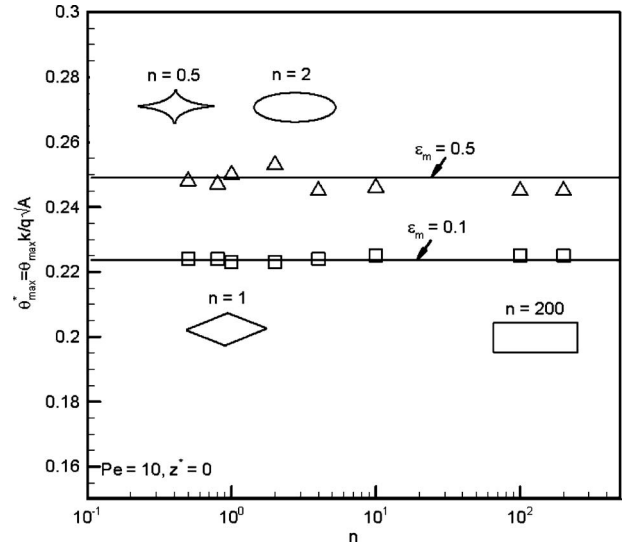

Fig. 4 Effect of heat source shape on the quasi-steady maximum temperature for two typical aspect ratios, 0.1 and 0.5, and Peclet number of Pe=10

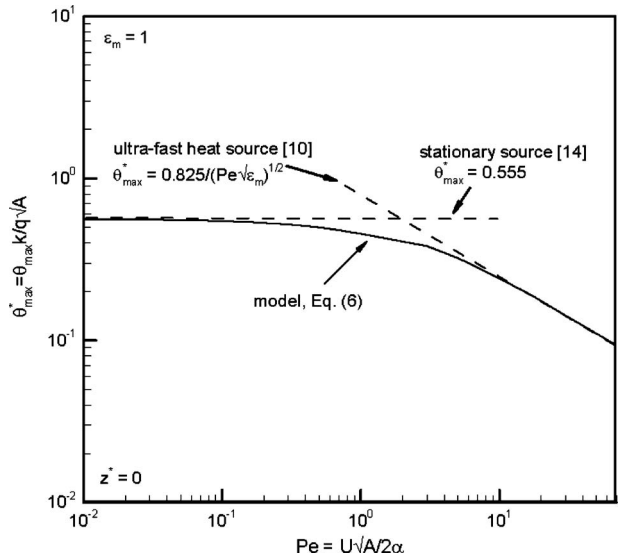

Fig. 6 Maximum temperature as a function of Peclet number for aspect ratio of ε_m=1, a typical value. Note that two asymptotes for stationary, Pe→0, and fast moving heat source, Pe →∞, can be recognized in the present plot.

very slow heat sources, (i.e., Pe→0), the maximum temperature within a half-space can be obtained from the stationary heat source solution [14],

$$\theta^*_{\max,s} = \sqrt{\frac{\varepsilon_s}{\pi}}\left[\frac{\sinh^{-1}(\varepsilon_s)}{\varepsilon_s} + \sinh^{-1}\left(\frac{1}{\varepsilon_s}\right)\right] \tag{4}$$

where $\theta^*_{\max,s}$ is the maximum temperature due to a stationary heat source. The aspect ratio of a stationary heat source is denoted by $\varepsilon_s = b/a$ such that $0 < \varepsilon_s \leq 1$. Equation (4) shows that for a stationary heat source, the highest maximum temperature occurs at the aspect ratio of 1 (e.g., square or circle). For a moving heat source, as the source speed increases, (i.e., Peclet number increases), the maximum temperature drops, the peak in the plot occurs to the lower aspect ratios, and the effect of the source orientation becomes less significant (see Fig. 5). This means that for heat sources with similar speed and areas, those which are elongated in the direction of motion have higher temperatures. For very high Peclet numbers, i.e., Pe~$0(10^2)$, it can be shown that $\theta^*_{\max} \propto \mathrm{Pe}^{-1.2}\varepsilon_m^{-1/4}$ [10].

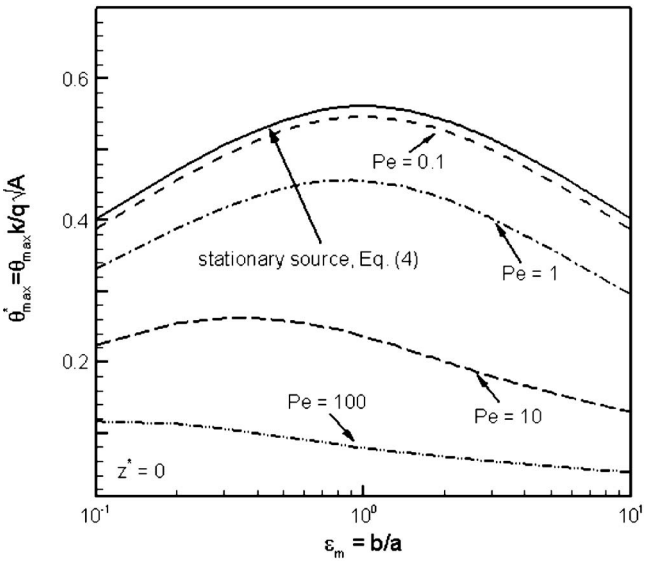

Fig. 5 Effect of the aspect ratio on the maximum temperature of a plane moving heat source at various source speeds (Peclet number)

4.3 Source Speed, Pe. Variation in the maximum surface temperature as a function of Peclet number for a typical aspect ratio of ε_m=1 is plotted in Fig. 6. When a heat source moves at higher speeds, it spends shorter time at each spot; thus, less heat is transferred to the half-space and the maximum temperature decreases. Two asymptotes can be recognized for each aspect ratio: (a) very slow (Pe→0) and (b) ultrafast moving heat source (Pe →∞). The maximum surface temperature for low Peclet numbers (i.e., Pe<0.1) can be obtained from Eq. (4). Since the source corners have negligible effect on the maximum temperature [14,15], Eq. (4) can be applied to other geometries such as ellipse, rhombic, star-shape, and rectangle with rounded corners with reasonable accuracy. For ultrafast moving heat sources (i.e., Pe→∞), Muzychka and Yovanovich [10] used the same approach of Jaeger [23] to obtain the maximum temperature due to an elliptical heat source as a function of Peclet number and aspect ratio. Comparing to the relationship provided by Jaeger [23] for a rectangular shape, it can be observed that the maximum temperature of an elliptical heat source ($n \to 2$) is 6.25% higher than that of a rectangular heat source ($n \to \infty$) with the same area. Following the approach of Muzychka and Yovanovich [10], Eq. (5) is developed for ultrafast finite moving heat sources of hyperelliptical shapes,

$$\theta^*_{\max,f} = \frac{0.825}{(\mathrm{Pe}\sqrt{\varepsilon_m})^{1/2}} \tag{5}$$

where $\theta^*_{\max,f}$ is the maximum temperature rise due to a fast moving heat source. Equation (5) accurately predicts the maximum surface temperature over the range of $0.5 \leq \varepsilon_m \leq 1$.

4.4 Distance From the Source Surface, z^*. In Fig. 7, the maximum temperature at different z-planes, $\theta^*_{\max}(z^*)$, is nondimensionalized with respect to the maximum temperature at the surface of the half-space, $\theta^*_{\max,0}$, and plotted against the dimensionless depth for three typical aspect ratios of 0.1, 0.5, and 1. Two geometries are considered: rectangle with a typical Peclet number of Pe=10 and stationary elliptical source. It can be seen that the temperature decreases rapidly at points near the heat

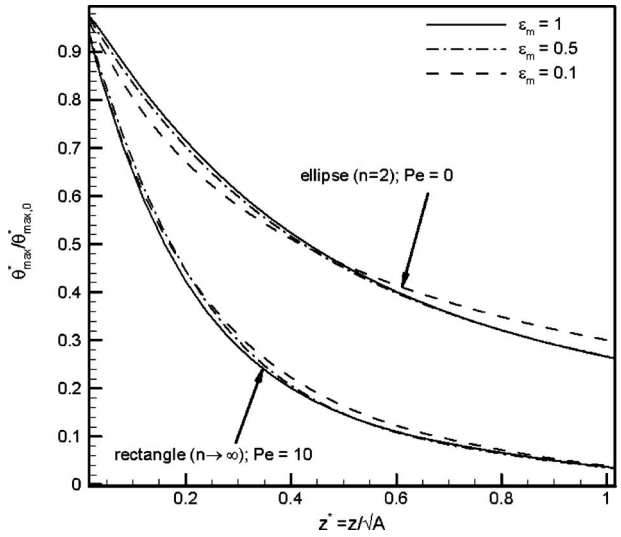

Fig. 7 Variation in $\theta^*_{max}/\theta^*_{max,0}$ as a function of dimensionless depth for elliptical (n→2) and rectangular (n→∞) heat sources with Pe=10 and various aspect ratios

source surface followed by a gradual change with increasing depth. Interestingly, although $\theta^*_{max}/\theta^*_{max,0}$ changes with the Peclet number, it is independent of both the corners (n) and the aspect ratio (ε_m).

4.5 Approximate Model. To develop a general compact relationship for the maximum temperature, we use the asymptotic blending method of Churchill and Usagi [36]. This method allows the combination of asymptotic solutions to generate a model that is valid for all values of the dependent parameter as follows:

$$\theta^*_{max,0} = \left[\frac{1}{(\theta^*_{max,s})^m} + \frac{1}{(\theta^*_{max,f})^m}\right]^{-1/m} \quad (6)$$

where $\theta^*_{max,s}$ and $\theta^*_{max,f}$ are obtained from Eqs. (4) and (5), respectively, and m is a correlation parameter. A single value of $m=2$ was found to give excellent agreement between the model and the solution of Eq. (2). Note that variation in $\theta^*_{max,s}$ with respect to the heat source aspect ratio is negligible for $0.5 \le \varepsilon_s \le 1$, and the average value of $\theta^*_{max,s}=0.555$ can be used instead of Eq. (4). Therefore, Eq. (6) reduces to

$$\theta^*_{max,0} = [3.240 + 1.474\mathrm{Pe}\sqrt{\varepsilon_m}]^{-1/2}, \quad 0.5 \le \varepsilon_m < \infty \quad (7)$$

Knowing that the ratio of $\theta^*_{max}/\theta^*_{max,0}$ is a weak function of the heat source aspect ratio (see Fig. 7), the following relationship is proposed for $\theta^*_{max}/\theta^*_{max,0}$ by curve fitting:

$$\frac{\theta^*_{max}}{\theta^*_{max,0}} = \frac{9e^{-z^*}}{(3 + z^*\sqrt{\pi\mathrm{Pe}})^2}, \quad z^* \le 1 \quad (8)$$

The proposed relationship is found to be accurate within 16% when compared against the full analytical results for $z^* \le 1$.

5 Comparison With Experimental and Numerical Data

Vick and Furey [24] computed the maximum temperature due to frictional heat generation between two sliding surfaces of square shape for the Peclet number range of $0.2 < \mathrm{Pe} < 14$. Table 3 shows the comparison between their results and those obtained from Eq. (7) with good agreement. Xu and Malkin [25] performed an experimental study to measure the temperature distribution within the workpiece of a grinding machine by using embedded thermocouples. The contact area in their work [25] is a rectangle that is elongated in the perpendicular direction of motion. The corresponding Peclet number and source aspect ratio for the experimental data are Pe=2.85 and ε_m=4.39, respectively. Other experimental conditions are listed in Table 4. Figure 8 shows that the experimental data are well predicted by Eqs. (7) and (8) with the accuracy of ±10%.

In an independent experiment, we used the proposed relationships to estimate the depth of channels engraved by a CO_2 laser system in wooden (red oak) substrates. The channel depth for a specific power and speed is estimated using Eqs. (7) and (8) by letting the maximum temperature to hold the value of autoignition temperature of red oak (i.e., the burning temperature of a material heated via radiation without any additional high-temperature heat source [20]). A value of $\alpha = 1.53 \times 10^{-7}$ $\mathrm{m}^2/\mathrm{s} \pm 5\%$ is taken as the red oak thermal diffusivity [20]

Table 3 Computed flash temperature at the surface of various sliding materials

Material	$\sqrt{A}$ (μm)	k (W/m K)	Pe	q_{mv}/q_f	$\theta_{num.}$ [24]	θ_{model}	Diff. %[a]
Al	194.4	237	1	0.57	56	56.98	−1.75
Si	28.2	148	0.2	0.51	625	649.95	−3.99
Ti	125.2	21.9	6.7	0.71	719	715.01	0.55
V	93.4	30.7	4.5	0.68	753	754.74	−0.23
Cr	90.4	93.7	1.6	0.59	296	294.38	0.55
Mn	58.2	7.8	13.4	0.77	3519	3537.44	−0.52
Fe	111.4	80	2.5	0.63	267	268.63	−0.61
Co	90.4	99.2	1.7	0.6	277	279.12	−0.77
Ni	69.6	90.7	1.5	0.59	397	400.31	−0.83
Cu	112.8	401	0.5	0.54	59	59.86	−1.46
Zn	163.8	116	2	0.61	129	129.06	−0.04
Zr	83.8	22.7	3.4	0.65	1195	1189.53	0.46
Mo	65.2	138	0.6	0.54	295	295.52	−0.18
Rh	91.4	150	0.9	0.56	189	191.14	−1.13
Pd	96.2	71.8	2	0.61	354	355.02	−0.29
Ag	112.8	429	0.3	0.53	56	57.08	−1.92
Hf	75.4	230	0.3	0.52	157	156.26	0.47
W	48.4	174	0.4	0.53	322	321.59	0.13
Pt	101	71	2	0.61	337	341.96	−1.47
Au	132.6	317	0.5	0.54	64	6.44	−0.65

[a]Diff. $\% = \theta_{num.[31]} - \theta_{model}/\theta_{num.[31]} \times 100$.

Table 4 Grinding conditions for experimental study of Xu and Malkin [25]

Parameter	Value
Wheel diameter	406 mm
Wheel width	12.5 mm
Depth of cutting	20 μm
Workpiece dimension	$44\times19\times25$ mm^3
Wheel velocity	58 m/s
Workpiece moving velocity	0.018 m/s
Temperature measurement methods	Embedded thermocouple Two color infrared detector Foil workpiece thermocouple

to compute the Peclet number. The reported auto-ignition temperature for the red oak is in the range of 420–500°C when it is irradiated by a CO_2 laser [20]. The maximum and minimum values of this range are used to compute the upper and lower bounds for the channel depth. In our calculations, the reference temperature, T_0, is assumed to hold the value of room temperature (i.e., 20°C). Figures 9 and 10 show the measured and estimated values of the channel depth as a function of the beam speed and power, respectively. Each data point in Figs. 9 and 10 is the average of at least five measured values. The error associated with the averaging method and the accuracy of the depth measurement method (±5 μm) are reported as error bars in Figs. 9 and 10. Good agreement between the estimated and measured values can be observed.

6 Summary and Conclusion

A comprehensive study on the effect of relevant geometrical parameters on the maximum temperature within a half-space due to a symmetrical moving heat source of arbitrary shape is performed in this work. The following summarizes the results of the present study.

- The heat source exact shape (e.g., corners) has a minimal effect on the maximum temperature within a half-space if the square root of source area is selected as a characteristic length throughout the analysis.
- Maximum temperature within a half-space decreases when the source speed increases. This is due to the fact that the heat source spends shorter time at each spot in higher speeds; thus, less heat is transferred to the half-space.
- For very low heat source speeds, i.e., Pe$\rightarrow$0, the effect of source orientation on the maximum temperature becomes insignificant, and the highest temperature occurs at the aspect ratio of 1 (e.g., square or circle). However, when the source speed increases, the effect of source orientation becomes significant, and the highest temperature occurs for the sources that are elongated in the direction of motion.
- The normalized maximum temperature within the half-

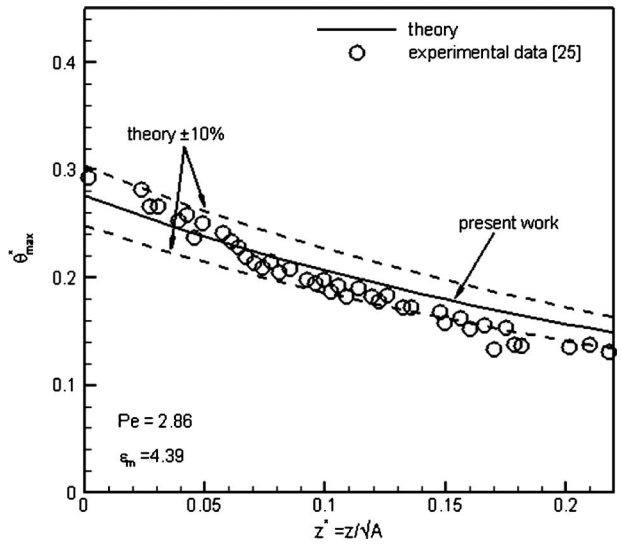

Fig. 8 Maximum dimensionless temperature in a half-space. Rectangular heat source with Pe=2.86 and aspect ratio of ε_m =4.39; experimental data from Ref. [25]; see Table 4 for the experiment parameters.

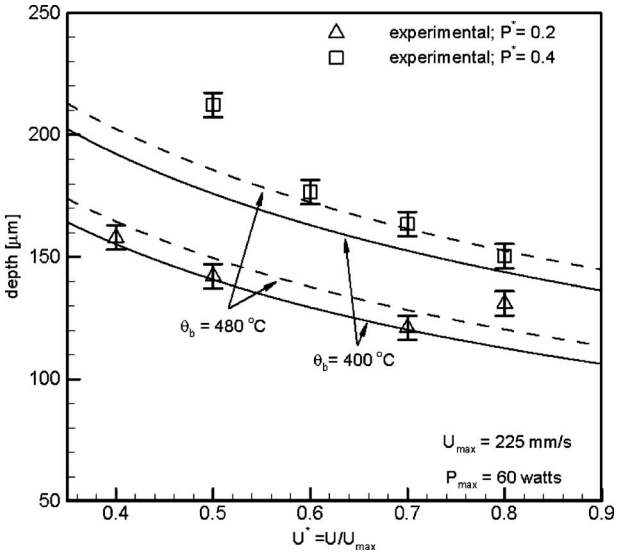

Fig. 9 Effect of laser beam speed on the depth of engraved channels using single pass ablation. Square (□) and delta (△) symbols are the present experimental measurements for percentage powers of 20% and 40%, respectively. Two limits of the reported ignition temperature are shown as the dashed line for 500°C and solid line for 420°C.

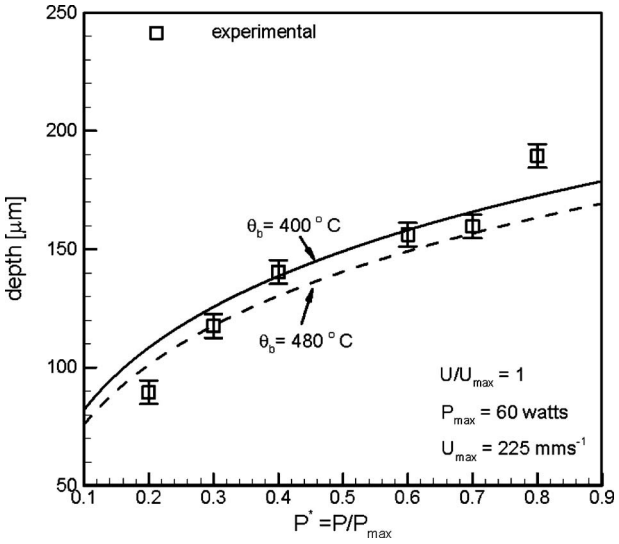

Fig. 10 Effect of laser power on the depth of engraved channels using single pass ablation at maximum beam speed. Square (□) symbols are the present experimental measurements maximum beam speed. Two limits of the reported ignition temperature are shown as the dashed line for 500°C and solid line for 420°C.

space, $\theta^*_{max}/\theta^*_{max,0}$, is found to be only a function of source speed (i.e., Peclet number). This is valid when the depth is up to the order of the length scale.

Based on the abovementioned observations, new compact relationships are proposed to predict the maximum temperature within the half-space over the entire range of Peclet numbers. In contrast to the available studies in the literature, the proposed relationship covers a wide range of symmetrical geometries and accounts for the effect of the heat source shape and orientation. The validity of the suggested relationships are examined by available experimental and numerical data for the grinding process for medium Peclet numbers, $0<\mathrm{Pe}<14$. For ultrafast heat sources ($50<\mathrm{Pe}<130$), an experimental study is performed using a commercial CO_2 laser system.

Acknowledgment

The authors gratefully acknowledge the financial support of the Natural Sciences and Engineering Research Council of Canada (NSERC), BC Innovation Council (BCIC), Canada Research Chair Program, and N. Alavi's assistance in the experimental measurements.

Nomenclature

A = heat source surface area, m^2
a = hyperellipse major axis, m
a^* = dimensionless major axis of hyperellipse
b = hyperellipse minor axis, m
b^* = dimensionless minor axis of hyperellipse
d_g = groove depth, m
d_s = laser beam size, m
F_o = Fourier number, $\alpha t/\mathcal{L}^2$
k = thermal conductivity, W/m K
n = shape parameter for hyperellipse
Pe = Peclet number, $U\mathcal{L}/2\alpha$
P^* = laser beam relative power
$\dot{q}$ = released energy per unit time per unit area, W/m^2
R^* = dimensionless distance from the origin in the moving coordinate, m
U = heat source speed, m/s
U^* = laser beam relative speed
T = temperature at any arbitrary point, K or °C
T_o = initial temperature, K or °C

Greek

α = thermal diffusivity, m^2/s
ε_m = moving source aspect ratio, b/a
ε_s = stationary source aspect ratio, b/a
$\mathcal{L}$ = characteristic length, m
θ = temperature rise $(T-T_o)$, K or °C
θ^* = dimensionless temperature rise, $\theta k/\dot{q}\mathcal{L}^2$
$\theta^*_{max,0}$ = dimensionless maximum temperature rise within a half-space due to a moving source
$\theta^*_{max,s}$ = dimensionless maximum temperature rise within a half-space due to a stationary source
$\theta^*_{max,f}$ = dimensionless maximum temperature rise of a very fast heat source
ω = absorption coefficient

References

[1] Sun, Y., Kwok, Y. C., and Nguyen, N. T., 2006, "Low-Pressure, High-Temperature Thermal Bonding of Polymeric Microfluidic Devices and Their Applications for Electrophoretic Separation," J. Micromech. Microeng., **16**, pp. 1681–1688.
[2] Kricka, L. J., Fortina, P., Panaro, N. J., Wilding, P., Alonso-Amigo, G., and Becker, H., 2002, "Fabrication of Plastic Microchips by Hot Embossing," Lab Chip, **2**(1), pp. 1–4.
[3] Halling, J., 1975, *Principles of Tribology*, Macmillan, London.
[4] Williams, J. A., 2005, *Engineering Tribology*, Cambridge University Press, Cambridge, UK.
[5] Winer, W. O., and Cheng, H. S., 1980, "Film Thickness, Contact Stress and Surface Temperatures," *Wear Control Handbook*, ASME, New York, pp. 81–141.
[6] Tian, X., and Kennedy, F. E., Jr., 1994, "Maximum and Average Flash Temperatures in Sliding Contacts," ASME J. Tribol., **116**, pp. 167–174.
[7] Hou, Z. B., and Komanduri, R., 2000, "General Solutions for Stationary/Moving Plane Heat Source Problems in Manufacturing and Tribology," Int. J. Heat Mass Transfer, **43**(10), pp. 1679–1698.
[8] Laraqi, N., Baïri, A., and Segui, L., 2004, "Temperature and Thermal Resistance in Frictional Devices," Appl. Therm. Eng., **24**(17–18), pp. 2567–2581.
[9] Carslaw, H. S., and Jaeger, J. C., 1959, *Conduction of Heat in Solids*, Oxford University Press, New York.
[10] Muzychka, Y. S., and Yovanovich, M. M., 2001, "Thermal Resistance Models for Non-Circular Moving Heat Sources on a Half Space," ASME J. Heat Transfer, **123**(4), pp. 624–632.
[11] Rosenthal, D., 1946, "The Theory of Moving Sources of Heat and Its Application to Metal Treatments," Trans. ASME, **68**(11), pp. 849–866.
[12] Weichert, R., and Schonert, K., 1978, "Temperature Distribution Produced by a Moving Heat Source," Q. J. Mech. Appl. Math., **31**(3), pp. 363–379.
[13] Terauchi, Y., Nadano, H., and Kohno, M., 1985, "On the Temperature Rise Caused by Moving Heat Sources. II: Calculation of Temperature Considering Heat Radiation From Surface," Bull. JSME, **28**(245), pp. 2789–2795.
[14] Yovanovich, M. M., 1997, "Transient spreading resistance of arbitrary isoflux contact areas-development of a universal time function," presented at the 32nd AIAA Thermophysics Conference, Atlanta, GA.
[15] Yovanovich, M. M., Negus, K. J., and Thompson, J. C., 1984, "Transient Temperature Rise of Arbitrary Contacts With Uniform Flux by Surface Element Methods," presented at the 22nd AIAA Aerospace Sciences Meeting, Reno, NV, Jan. 9–12.
[16] www.maplesoft.com
[17] Simms, D. L., 1960, "Ignition of Cellulosic Materials by Radiation," Combust. Flame, **4**, pp. 293–300.
[18] Koohyar, A. N., 1967, *Ignition of Wood by Flame Radiation*, University of Oklahoma, Norman, OK.
[19] Kashiwagi, T., 1979, "Experimental Observation of Radiative Ignition Mechanisms," Combust. Flame, **34**, pp. 231–244.
[20] Kashiwagi, T., 1979, "Effects of Attenuation of Radiation on Surface Temperature for Radiative Ignition," Combust. Sci. Technol., **20**(5), pp. 225–234.
[21] Wesson, H. R., 1970, *The Piloted Ignition of Wood by Radiant Heat*, University of Oklahoma, Norman, OK.
[22] Taylor, J. R., 1997, *An Introduction to Error Analysis: The Study of Uncertainties in Physical Measurements*, University Science Books, Herndon, VA.
[23] Jaeger, J. C., 1942, "Moving Sources of Heat and the Temperature at Sliding Contacts," J. Proc. R. Soc. N. S. W., **76**, pp. 203–224.
[24] Vick, B., and Furey, M. J., 2003, "An Investigation Into the Influence of Frictionally Generated Surface Temperatures on Thermionic Emission," Wear, **254**(11), pp. 1155–1161.
[25] Xu, X., and Malkin, S., 2001, "Comparison of Methods to Measure Grinding Temperatures," ASME J. Manuf. Sci. Eng., **123**, pp. 191–195.
[26] Takazawa, K., 1966, "Effects of Grinding Variables on Surface Structure of Hardened Steel," Bull. Jap. Soc. Grind Eng., **6**, pp. 14–19.
[27] Paek, U.-C., and Gagliano, F., 1972, "Thermal Analysis of Laser Drilling Processes," IEEE J. Quantum Electron., **8**(2), pp. 112–119.
[28] Eagar, T. W., and Tsai, N. S., 1983, "Temperature Fields Produced by Traveling Distributed Heat Sources," Weld. J. (Miami, FL, U.S.), **62**(12), pp. 346–355.
[29] Zhang, H. J., 1990, "Non-Quasi-Steady Analysis of Heat Conduction From a Moving Heat Source," ASME Trans. J. Heat Transfer, **112**, pp. 777–779.
[30] Manca, O., Morrone, B., and Naso, V., 1995, "Quasi-Steady-State Three-Dimensional Temperature Distribution Induced by a Moving Circular Gaussian Heat Source in a Finite Depth Solid," Int. J. Heat Mass Transfer, **38**(7), pp. 1305–1315.
[31] Yevtushenko, A. A., Ivanyk, E. G., and Ukhanska, O. M., 1997, "Transient Temperature of Local Moving Areas of Sliding Contact," Tribol. Int., **30**(3), pp. 209–214.
[32] Zeng, Z., Brown, J. M. B., and Vardy, A. E., 1997, "On Moving Heat Sources," Heat Mass Transfer, **33**(1–2), pp. 41–49.
[33] Zubair, S. M., and Chaudhry, M. A., 1998, "A Unified Approach to Closed-Form Solutions of Moving Heat-Source Problems," Heat Mass Transfer, **33**(5–6), pp. 415–424.
[34] Zubair, S. M., and Chaudhry, M. A., 1996, "Temperature Solutions Due to Time-Dependent Moving-Line-Heat Sources," Heat Mass Transfer, **31**(3), pp. 185–189.
[35] Kato, T., and Fujii, H., 1997, "Temperature Measurement of Workpiece in Surface Grinding by PVD Film Method," ASME J. Manuf. Sci. Eng., **119**, pp. 689–694.
[36] Kaebernick, H., Bicleanu, D., and Brandt, M., 1999, "Theoretical and Experimental Investigation of Pulsed Laser Cutting," CIRP Ann., **48**(1), pp. 163–166.
[37] Neder, Z., Varadi, K., Man, L., and Friedrich, K., 1999, "Numerical and Finite Element Contact Temperature Analysis of Steel-Bronze Real Surfaces in Dry Sliding Contact," Tribol. Trans., **42**(3), pp. 453–462.
[38] Baïri, A., 2003, "Analytical Model for Thermal Resistance Due to Multiple Moving Circular Contacts on a Coated Body," C. R. Mec., **331**(8), pp. 557–562.

[39] Li, J. F., Li, L., and Stott, F. H., 2004, "Comparison of Volumetric and Surface Heating Sources in the Modeling of Laser Melting of Ceramic Materials," Int. J. Heat Mass Transfer, **47**(6–7), pp. 1159–1174.
[40] Kuo, W. L., and Lin, J. F., 2006, "General Temperature Rise Solution for a Moving Plane Heat Source Problem in Surface Grinding," Int. J. Adv. Manuf. Technol., **31**(3–4), pp. 268–277.
[41] Bianco, N., Manca, O., Nardini, S., and Tamburrino, S., 2006, "Transient Heat Conduction in Solids Irradiated by a Moving Heat Source," presented at the Proceedings of COMSOL Users Conference, Milan.
[42] Wen, J., and Khonsari, M. M., 2007, "Analytical Formulation for the Temperature Profile by Duhamel's Theorem in Bodies Subjected to an Oscillatory Heat Source," ASME J. Heat Transfer, **129**, pp. 236–240.
[43] Levin, P., 2008, "A General Solution of 3-D Quasi-Steady-State Problem of a Moving Heat Source on a Semi-Infinite Solid," Mech. Res. Commun., **35**(3), pp. 151–157.
[44] Laraqi, N., Alilat, N., de Maria, J. M., and Bāīri, A., 2009, "Temperature and Division of Heat in a Pin-on-Disc Frictional Device—Exact Analytical Solution," Wear, **266**(7–8), pp. 765–770.
[45] Xu, H., Chen, W. W., Zhou, K., Huang, Y., and Wang, Q. J., 2010, "Temperature Field Computation for a Rotating Cylindrical Workpiece Under Laser Quenching," Int. J. Adv. Manuf. Technol., **47**(5–8), pp. 679–686.

Appendix D

Pressure drop in microchannels as compared to theory based on arbitrary cross-section

(with permission from ASME)

Mohsen Akbari[1]
Ph.D. Candidate
Mechatronic System Engineering,
School of Engineering Science,
Simon Fraser University,
Surrey, BC, V3T 0A3, Canada
e-mail: maa59@sfu.ca

David Sinton
Associate Professor
Department of Mechanical Engineering,
University of Victoria,
Victoria, BC, V8W 2Y2, Canada

Majid Bahrami
Assistant Professor
Mem. ASME
Mechatronic System Engineering,
School of Engineering Science,
Simon Fraser University,
Surrey, BC, V3T 0A3, Canada

Pressure Drop in Rectangular Microchannels as Compared With Theory Based on Arbitrary Cross Section

Pressure driven liquid flow through rectangular cross-section microchannels is investigated experimentally. Polydimethylsiloxane microchannels are fabricated using soft lithography. Pressure drop data are used to characterize the friction factor over a range of aspect ratios from 0.13 to 0.76 and Reynolds number from 1 to 35 with distilled water as working fluid. Results are compared with the general model developed to predict the fully developed pressure drop in arbitrary cross-section microchannels. Using available theories, effects of different losses, such as developing region, minor flow contraction and expansion, and streaming potential on the measured pressure drop, are investigated. Experimental results compare well with the theory based on the presure drop in channels of arbitrary cross section. [DOI: 10.1115/1.3077143]

1 Introduction

Advances in microfabrication make it possible to build microchannels with micrometer dimensions. Micro- and minichannels show potential and have been incorporated in a wide variety of unique, compact, and efficient cooling applications in microelectronic devices [1]. These microheat exchangers or heat sinks feature extremely high heat transfer surface area per unit volume ratios, high heat transfer coefficients, and low thermal resistances. In biological and life sciences, microchannels are used widely for analyzing biological materials such as proteins, DNA, cells, embryos, and chemical reagents [2]. Various microsystems, such as microheat sinks, microbiochips, microreactors, and micronozzles have been developed in recent years [3–6]. Since microchannels are usually integrated into these microsystems, it is important to determine the characteristics of the fluid flow in microchannels for better design of various microflow devices.

In parallel to the recent advances in microfluidic devices, microfabrication techniques have evolved. Some of the important fabrication techniques include lithography (soft and photolithography), lamination, injection molding, hot embossing, laser micromachining, and electrochemical or ultrasonic technologies [2,7–10]. Together with new methods of fabrication, it is possible to exploit certain fundamental differences between the physical properties of fluids moving in large channels and those traveling through micrometer-scale channels [2]. In recent years, a large number of papers have reported pressure drop data for laminar fully developed flow of liquids in microchannels with various cross sections [11–32]. Rectangular cross sections have been extensively studied as they are employed in many applications [11–16]. However, published results are often inconsistent. Some authors reported a huge deviation from the conventional theories and attributed it to an early onset of laminar to turbulent flow transition or surface phenomena such as surface roughness, electrokinetic forces, viscous heating effects, and microcirculation near the wall [12–26].

Jiang et al. [28] conducted an experimental investigation of water flow through different microchannel cross sections including circular, rectangular, trapezoidal, and triangular. The hydraulic diameter of microchannels varied from 8 μm to 42 μm. They collected experimental data with the Reynolds number ranging from 0.1 to 2, and concluded that there was less influence of the cross-sectional shape on the microflow in the microchannel and that the experimental data agreed well with the prediction of the conventional theory. Baviere et al. [29] performed an experimental study on the water flow through smooth rectangular microchannels. Their channels were made of a silicon engraved substrate anodically bonded to a Pyrex cover. Their results showed that in smooth microchannels, the friction law is correctly predicted by conventional theories. Judy et al. [15] and Bucci et al. [30] showed that their experimental results were in good agreement with conventional theories in the laminar regime. Also Wu and Cheng [31], Liu and Garimella [32], and Gao et al. [33] reported good agreement between experimental data with conventional theories.

Low Reynolds numbers characterize many microscale liquid flows [34]. Hence, nonlinear terms in the Navier–Stokes equation disappear for fully developed flow, resulting in Poisson's equation

$$\nabla^2 u = \frac{1}{\mu}\frac{dp}{dz}, \quad u = 0 \text{ on } \Gamma \tag{1}$$

where u is the fluid velocity, z is the flow direction, and Γ is the perimeter of the channel. Exact solution for Eq. (1) in rectangular cross-section channels can be found in fluid mechanics textbooks such as Ref. [35]. The original analytical solution for the mean velocity in rectangular channels is in the form of a series, but it has been shown that using the first term of the series results in errors less than 0.7%.

Recently, Bahrami et al. [1,36] developed a general model for prediction of pressure drop in microchannels of arbitrary cross section. Using the analytical solution of elliptical duct and the concept of Saint-Venant principal in torsion [37], they showed that the Poiseuille number, $f\ \mathrm{Re}_{\sqrt{A}}$, is a function of the polar moment of inertia, I_P, area, A, and perimeter of the cross section of the channel, Γ. Their model showed good agreement with experimental and numerical data for a wide variety of channel cross sections such as rectangular, trapezoidal, triangular, circular, and moon shaped.

[1]Corresponding author.

Contributed by the Fluids Engineering Division of ASME for publication in the JOURNAL OF FLUIDS ENGINEERING. Manuscript received June 11, 2008; final manuscript received December 5, 2008; published online March 6, 2009. Assoc. Editor: James A. Liburdy. Paper presented at the ECI International Conference on Heat Transfer and Fluid Flow in Microscale III, Whistler, BC, Canada, September 21–26, 2008.

However, they [1,36] did not perform any experiment to verify this model, thus they could not investigate all issues and effects of different parameters. As a result the goal of the present work is to independently validate the general model of Bahrami et al. [1,36]. Moreover, effects of different parameters, including microchannel dimensions, minor and developing region losses, viscous heating, electroviscous phenomena, and channel deformation on the measured pressure drop, have been discussed. By successfully validating the model, it will be used in more complicated channel geometries such as variable cross-section microchannels.

2 Theory

Selection of the characteristic length is an arbitrary choice and will not affect the final solution. However, an appropriate length scale leads to more consistent results, especially when a general cross section is considered. A circular duct is fully described with its diameter, thus the obvious length scale is the diameter (or radius). For noncircular cross sections, the selection is not as clear; many textbooks and researchers have conventionally chosen the hydraulic diameter as the characteristic length. Yovanovich [38] introduced the square root of area as a characteristic length scale for heat conduction and convection problems. Later, Muzychka and Yovanovich [39] proposed the use of $\sqrt{A}$ for the fully developed flow in noncircular ducts. Bahrami et al. [1,37] showed that the square root of area appears in the solution of fully developed flow in noncircular ducts. They also compared both D_h and $\sqrt{A}$ and observed that using $\sqrt{A}$ as the characteristic length scale results in similar trends in Poiseuille number for microchannels with a wide variety of cross sections. Therefore, in this study, $\sqrt{A}$ is selected consistently as the length scale throughout the analysis.

According to the model of Bahrami et al. [1], pressure drop of laminar fully developed flow in arbitrary cross-section microchannels can be obtained from

$$\Delta P = 16\pi^2 \mu Q I_p^* \frac{L}{A^2} \tag{2}$$

where $I_p^* = I_p/A$ is the specific polar momentum of inertia of the microchannel cross section, $\Gamma = 4(W+H)$ is the microchannel cross-section perimeter, L is the fully developed length, and Q is the the volumetric flow rate. Substituting for the geometrical parameters in Eq. (2) for microchannels of rectangular cross section and the definition of the Poiseuille number yields [1]

$$f\ \mathrm{Re}_{\sqrt{A}} = \frac{4\pi^2(1+\varepsilon^2)}{3\sqrt{\varepsilon}(1+\varepsilon)} \tag{3}$$

As can be seen the only parameter effects the Poiseuille number in rectangular channels is the cross-section aspect ratio, consistent with previous works [35,40]. For rectangular microchannels, two asymptotes can be recognized, i.e., very narrow rectangular and square channels

$$f\ \mathrm{Re}_{\sqrt{A}} = \frac{4\pi^2}{3\sqrt{\varepsilon}}; \quad \varepsilon \to 0$$

$$f\ \mathrm{Re}_{\sqrt{A}} = 13.16; \quad \varepsilon = 1 \tag{4}$$

3 Experimental Setup

3.1 Chemicals and Materials. De-ionized water was used as the testing liquid. SU-8 photoresist (Microchem, Newton, MA) and diacetone-alcohol developer solution (Sigma-Aldrich, St. Louis, MO) were used in the making of the positive relief masters by the procedure outlined below. Polydimethylsiloxane (PDMS) casts were prepared by thoroughly mixing the base and curing agent at a 10:1 ratio as per the manufacturer's instructions for the Sylgard 184 silicon elastomer kit (Dow Corning, Midland, MI). Caution was used to avoid contact between the liquid PDMS and latex rubber (gloves), as this was found to inhibit curing [41].

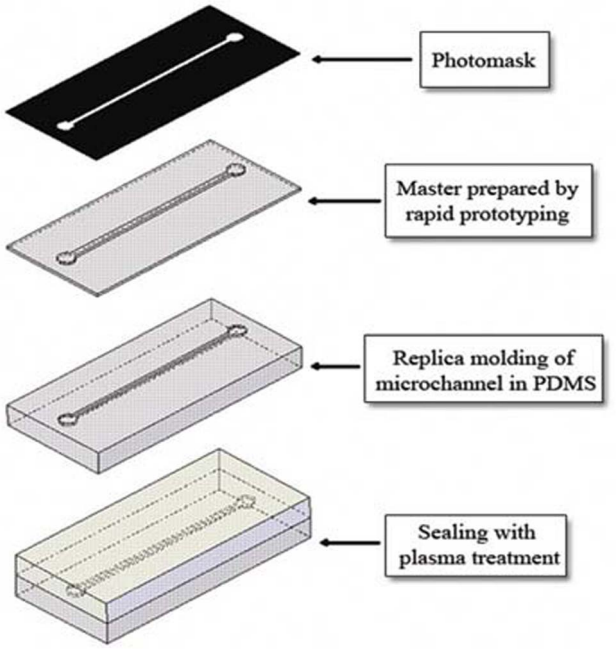

Fig. 1 Schematic of the soft lithography technique

3.2 Microfabrication. The PDMS/PDMS microchannels used in this study have been manufactured using the soft lithography technique [42] described by Erickson et al. [41]. A schematic of the process is provided in Fig. 1. Photomasks were designed by AUTOCAD software[2] and printed with a 3500DPI printer (Island Graphics Ltd., Victoria, BC, Canada). Masters containing the desired microchannel pattern have been made by spin coating of SU-8 negative photoresist on a glass slide to the desired thickness. The photoresist film was then hardened through a two-stage direct contact pre-exposure bake procedure (65 °C for 5 min and 95 °C for 30 min) and exposed to UV light for 100 s through the mask containing the channel pattern. A two-stage postexposure bake procedure (65 °C for 5 min and 95 °C for 30 min) was then used to enhance cross linking in the exposed portion of the film. The slide was then placed in quiescent developer solution for 10 min to dissolve the unexposed photoresist, leaving a positive relief containing the microchannel pattern.

Liquid PDMS was then poured over the master and exposed to vacuum condition (1 h) to extract all the bubbles in it and cured at 85 °C for 15–20 min yielding a negative cast of the microchannel pattern. An enclosed microchannel was then formed by bonding the PDMS cast with another piece of PDMS via plasma treatment.

Five microchannels were made with a range of aspect ratios, $0.13 < \varepsilon < 0.76$, and tested in this study. Dimensions of the microchannels are shown in Table 1. The channels' names in the table indicate the channel material, cross-sectional shape, and the aspect ratio (i.e., PPR-0.13 corresponds to the PDMS/PDMS chip with rectangular cross section and the aspect ratio of 0.13). As can be seen, channels were designed long enough so that fully developed flow is dominant. Since the microchannel dimensions have a major effect on the friction factor calculation [13,15,33], a destructive careful measurement was performed after the experiments. Channels were cut carefully at three random cross sections. The cutting lines were perpendicular to the channel to ensure a 90 deg viewing angle. Dimensions of the channel were measured by an image processing method. To do so, a Leica DMI 6000B (Leica Microsystems, Richmond Hill, ON, Canada) microscope with a 10×, 0.4 N.A. objective was used. Images of the channel cross

[2] www.usa.autodesk.com.

Table 1 Dimensions of the fabricated microchannels

Channel	Width, $2W$ (μm)	Depth, $2H$ (μm)	Length, L (mm)	$\varepsilon = H/W$	$L_{D,\max}/L$ (%)
PPR-0.13	780	110	50	0.13	3.47
PPR-0.17	581	101	50	0.17	4.03
PPR-0.4	480	192	58.8	0.4	5.55
PPR-0.6	189	113	55.5	0.6	6.75
PPR-0.76	134	103	50	0.76	7.86

section were captured by a high resolution high sensitivity CCD camera (Hamamatsu Orca AG, NJ) and imported into a photo editing software, ADOBE PHOTOSHOP 8.0. Dimensions of the channel were then measured by pixel counting. Size of each pixel was calibrated using a known dimension provided by the microscope image acquisition software. Accuracy of this method was found to be ± 3.6 μm. Due to the microfabrication process, the microchannel cross section has some deviations from the rectangular shape. Height and width measurements were conducted at different random positions for each cross section and the average value was determined. This measurement was also performed at several cross sections. Mean values are reported in Table 1. It was observed that both microchannel depth and width were different from the expected values in the fabrication process. From our measurements, channel height, and width deviated less than 4% and 3% from the designed sizes, respectively. Since smooth surfaces were observed by the image processing technique described above, the roughness of the channels was estimated to be less than the accuracy of the image processing method. Hence, the relative channel roughness (channel roughness/channel length scale) was found to be less than 3%. As a result the effect of roughness on the pressure drop of the fully developed flow can be neglected [27].

3.3 Experimental Procedure. An open loop syringe pump system, as illustrated in Fig. 2, was designed for this work. A syringe pump (Harvard Apparatus, QC, Canada) provided constant flow rate with $\pm 0.5\%$ accuracy. A range of Reynolds numbers was covered by changing the volumetric flow rate from 40 μl/min to 240 μl/min. Water was forced to flow through a submicron filter (Aktreingeselchaf Co., Germany) before entering the channel. To measure the pressure drop, a gauge pressure transducer (Omega Inc., Laval, QC, Canada) was fixed at the channel inlet while the channel outlet was opened to the atmosphere. Teflon tubing (Scientific Products And Equipment, North York, ON, Canada) was employed to connect the pressure transducer to the syringe pump and the microchannel. Measured pressure was then monitored and recorded with a computerized data acquisition system (LABVIEW 8.5, National Instruments, USA[3]). The flow was considered to have reached a steady state condition when the readings of the pressure drop did not change with time. For a given channel, the measurement of pressure drop was repeated three times for each flow rate. An arithmetic averaging method [43] was performed to determine the final results.

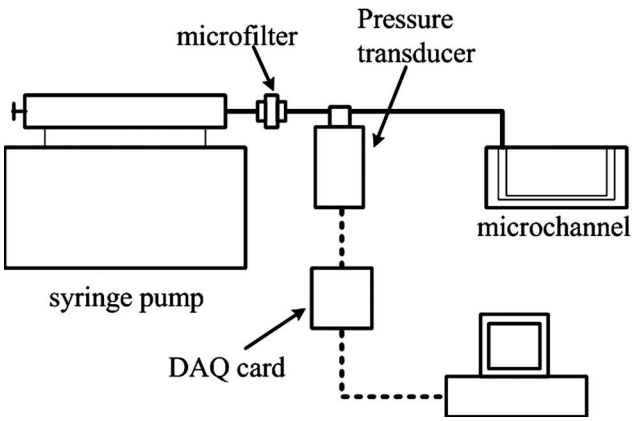

Fig. 2 Schematic of the test section

4 Analysis of Experimental Data

Reynolds number was calculated knowing the volumetric flow rate, Q, and the cross-sectional area, A, from

$$\mathrm{Re}_{\sqrt{A}} = \frac{\rho Q}{\mu \sqrt{A}} \tag{5}$$

Viscous dissipation effect was neglected since the dimensionless number $4\ \mathrm{Ec}[L^* f\ \mathrm{Re}_{\sqrt{A}}]/\mathrm{Re}_{\sqrt{A}} = 0.006$ is much smaller than 1. The value of $\Delta T_{\mathrm{ref}} = 1\,^\circ\mathrm{C}$ was used to calculate the Eckert number, Ec, for water as a working fluid [26]. Hence, the properties of the water was assumed to be constant.

Total measured pressure drop during the experiment, $\Delta P_{\mathrm{measured}}$ is

$$\Delta P_{\mathrm{measured}} = \Delta P_c + \Delta P_{\mathrm{in}} + \Delta P_D + \Delta P_{\mathrm{FD}} + \Delta P_{\mathrm{ex}} + 2\Delta P_b + \Delta P_{\mathrm{ev}} \tag{6}$$

where ΔP_c is the pressure loss due to the flow in the connecting tubes, ΔP_{in} and ΔP_{ex} are the inlet and exit losses, ΔP_D is the developing region loss, ΔP_{FD} is the pressure drop in the fully developed region, ΔP_b is the pressure drop due to 90 deg bends, and ΔP_{ev} is the pressure drop corresponds to the electroviscous effect. Since fully developed pressure drop is the focus of this study, right hand side losses except ΔP_{FD} must be subtracted from the measured pressure drop.

4.1 Connecting Tube Pressure Loss, ΔP_c. The connecting tube pressure drop includes the losses due to all fittings and the capillary tube from the transducer to the microchannel inlet. We measured this loss directly at each flow rate when there was no microchannel at the end of the tubing. The measurements were carefully conducted with the conditions identical to the case when a microchannel was added to the end of the connecting tube to avoid the effects of hydrostatic pressure.

4.2 Developing Region, ΔP_D. Since the viscous boundary layer inherently grows faster in microchannels than in macroscales, the developing region in most cases is negligible. There are few references that can be found in literature, in which the effect of inlet region was considered [40,44,45]. Phillips [44] showed that the length of the hydrodynamic developing region, L_D, depends on the aspect ratio of rectangular cross-section microchannels; the higher the aspect ratio, the longer the developing length. Maximum value of L_D can be obtained from Eq. (7)

$$L_D = \frac{4\varepsilon}{(1+\varepsilon)^2}\frac{\rho Q}{\mu} \tag{7}$$

This equation shows that the developing length depends on the flow rate and the channel aspect ratio. The higher the aspect ratio and/or flow rate, the higher the developing length. Ratio of the maximum developing length over the total length of the microchannel is listed in Table 1 for different channels. Obviously this length occurs in the maximum flow rate. Pressure drop associated with the entrance region after changing the length scale to $\sqrt{A}$ is [46]

$$\Delta P_D = \frac{(f\ \mathrm{Re}_{\sqrt{A}})\mu Q \Gamma}{2A\sqrt{A}} L_D + K\frac{\rho Q^2}{2A^2} \tag{8}$$

where $K = 0.6796 + 1.2197\varepsilon + 3.3089\varepsilon^2 - 9.5921\varepsilon^3 + 8.9089\varepsilon^4$

[3] www.ni.com.

Table 2 Ratio of the developing region pressure drop over the measured pressure drop of the microchannel

	$\Delta P_D/\Delta P_{\text{measured}}$ (%)				
Q (μl/min)	ε=0.13	ε=0.17	ε=0.4	ε=0.6	ε=0.76
40	0.01	0.01	0.04	0.03	0.04
60	0.01	0.02	0.03	0.04	0.06
80	0.01	0.02	0.04	0.06	0.08
100	0.02	0.01	0.06	0.07	0.10
120	0.02	0.02	0.06	0.08	0.11
240	0.03	0.05	0.10	0.20	0.24

$-2.9959\varepsilon^5$.

In Eq. (8), $f\ \mathrm{Re}_{\sqrt{A}}$ was calculated based on the measured pressure drop. Table 2 lists the relative pressure loss of the developing region with respect to the measured pressure drop. As can be seen, the values are small, less than 0.3%, and can be neglected for the range of Reynolds numbers studied in this work ($1<\mathrm{Re}_{\sqrt{A}}<35$). For the higher Reynolds numbers ($\mathrm{Re}\sim 100$), the developing pressure drop, ΔP_D, was found to be less than 2% of the fully developed pressure drop obtained from Eq. (3).

4.3 Minor Losses, ΔP_{min}. Other pressure losses associated with the measured pressure drop are inlet, exit, and bend losses. These losses are usually obtained from the traditional relationships used in macroscale [15,44,46,47]. Phillips [44] showed that the minor pressure losses can be obtained from

$$\Delta P_{\text{min}} = \Delta P_{\text{in}} + \Delta P_{\text{ex}} + 2\Delta P_b = \frac{\rho Q^2}{2A}\left[K_c + K_e + 2K_b\left(\frac{A}{A_t}\right)^2\right] \tag{9}$$

where A and A_t are the channel and connecting tube cross-sectional areas, respectively. K_b is the loss coefficient for the bend, and K_c and K_e represent the contraction and expansion loss coefficients due to area changes. Phillips [44] recommended K_b to be approximately 1.2 for a 90 deg bend. Assuming equal cross-sectional areas for the channel and connecting tubes and also maximum possible values for K_c and K_e [48], relative minor losses with respect to the measured pressure drop are listed in Table 3. As can be seen, these losses are negligible compared with the measured pressure drop. For higher Reynolds numbers ($\mathrm{Re}\sim 100$), minor pressure drop, ΔP_{min}, was found to be less than 5% of the fully developed pressure drop obtained from Eq. (3).

4.4 Electroviscous Effect, ΔP_{ev}. When a liquid is forced through a narrow channel under an applied pressure gradient, the counterions in the diffusive layer of EDL (electric double layer) are moving toward the downstream end and a potential gradient is induced in the flow [49]. This so called streaming potential acts to drive the counterions in the diffuse layer of the EDL to move in the direction opposite to the pressure-driven flow. The overall result is a reduced flow rate for a constant pressure gradient or increase in pressure drop for a given flow rate. This phenomenon, which gives the appearance of an increased viscosity, μ_a, is called the electroviscous effect [50]. The ratio of this apparent viscosity to the actual fluid viscosity for circular cross-section capillaries can be found from [50]

$$\frac{\mu_a}{\mu} \approx 1 + \frac{32\mu}{\sigma_b D^2}\mu_{\text{eo}}^2 \tag{10}$$

where D is the capillary diameter, μ is the fluid viscosity, σ_b is the liquid electrical conductivity, and a is the radius of the capillary. $\mu_{\text{eo}}=\varepsilon_0\varepsilon_r\zeta/\mu$ is the electro-osmotic mobility, where $\varepsilon_0=8.854\times10^{-12}$ $\mathrm{C^2\ V^{-1}\ m^{-1}}$ is the permittivity of vacuum, $\varepsilon_r=78.3$ is the relative permittivity for water at 25°C [49], and ζ is the zeta potential of the surface. Approximating the rectangular cross-section microchannel with a capillary of the same cross-sectional area, $\sigma_b=5.6\times10^{-6}$ $\mathrm{S\ m^{-1}}$ [51] and $\mu_{\text{eo}}=5.9\times10^{-8}$ $\mathrm{m^2\ V^{-1}\ s^{-1}}$ [52] for PDMS, value of μ_a/μ was found to be less than 1.03 for the channel sizes in this study.

Table 3 Ratio of the minor pressure loss over the measured pressure drop of the microchannel

	$\Delta P_{\text{min}}/\Delta P_{\text{measured}}$ (%)				
Q (μl/min)	ε=0.13	ε=0.17	ε=0.4	ε=0.6	ε=0.76
40	0.04	0.04	0.12	0.09	0.11
60	0.05	0.07	0.10	0.13	0.17
80	0.07	0.10	0.14	0.17	0.23
100	0.08	0.07	0.21	0.22	0.28
120	0.09	0.10	0.19	0.25	0.35
240	0.16	0.24	0.35	0.51	0.70

4.5 Effect of Channel Deformation Under Pressure-Driven Flow. Effect of channel deformation becomes important since it can change the microchannel cross-sectional area and as a result the pressure drop. In all equations used in Secs. 1–3, we assumed that the channel cross section did not change under pressure-driven flow. Few works have discussed the importance of bulk deformation in rectangular microchannels. Holden et al. [53] measured the PDMS bulk deformation under high pressure drops ($\sim$1 bar) using the change in fluorescence intensity. Gervais et al. [54] studied the elastic deformation of PDMS microchannels under imposed flow rates. They demonstrated that the channel deformation can effect the the laminar flow profile and pressure distribution within the channels with low aspect ratios and high pressure drops. In a bulged microchannel, measured pressure drop no longer changes linearly with the flow rate [53]. This is because the microchannel cross section varies due to deformation, and for a constant flow rate, pressure drop changes. Figure 3 shows the variation in the channel pressure drop with flow rate for present work. Experimental results properly follow the linear behavior of theoretical profiles. Thus one can conclude that the channel deformation has negligible effect on the results in this work. However, a careful experimental and theoretical investigation is required to study the effect of the channel deformation on the pressure drop of moderate and high aspect ratio rectangular cross-section microchannels.

4.6 Uncertainty Analysis. A careful analysis of the experimental uncertainty in this study is critical to the interpretation of experimental data of Poiseuille number, Po, and exploration of deviations from the macroscale theory. Neglecting the developing region, minor losses, electroviscous effects, and considering that the channel deformation is not significant, the experimental Poiseuille number can be obtained from

$$\mathrm{Po}_{\text{exp}} = \frac{4}{\mu Q}\left(\frac{A^2\sqrt{A}}{L\Gamma}\right)\Delta P_{\text{FD}} \tag{11}$$

where $\Delta P_{\text{FD}}=\Delta P_{\text{measured}}-\Delta P_c$. The uncertainty associated with Po_{exp} based on the measured variables, and the method provided in Ref. [43] is then given by

$$\frac{\omega_{\mathrm{Po}_{\text{exp}}}}{\mathrm{Po}_{\text{exp}}} = \left[\left(\frac{\omega_{\Delta P}}{\Delta P}\right)^2 + \left(\frac{\omega_L}{L}\right)^2 + \left(\frac{\omega_\Gamma}{\Gamma}\right)^2 + \frac{25}{4}\left(\frac{\omega_A}{A}\right)^2 + \left(\frac{\omega_Q}{Q}\right)^2\right]^{1/2} \tag{12}$$

where ω values indicate uncertainty associated with each variable as subscribed, $\omega_A=4[(H\omega_W)^2+(W\omega_H)^2]^{1/2}$ and $\omega_\Gamma=4[\omega_W^2+\omega_H^2]^{1/2}$ (see Appendix for details of calculations). In this equation we

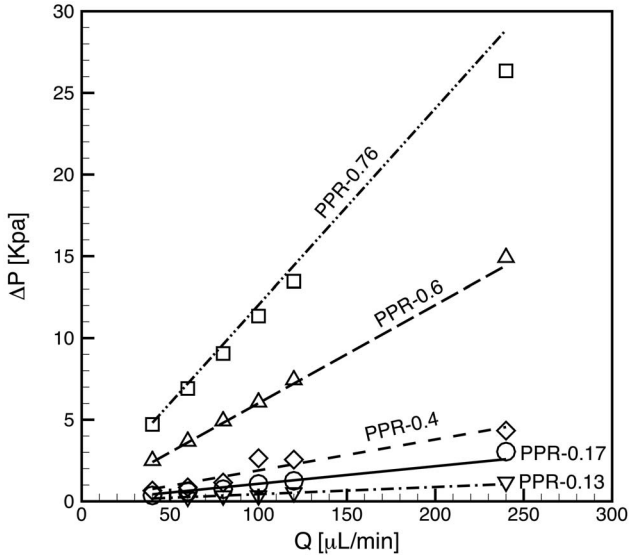

Fig. 3 Channel pressure drop as a function of flow rate. Lines show the theoretical prediction of pressure drop using Eq. (3) and symbols show the experimental data.

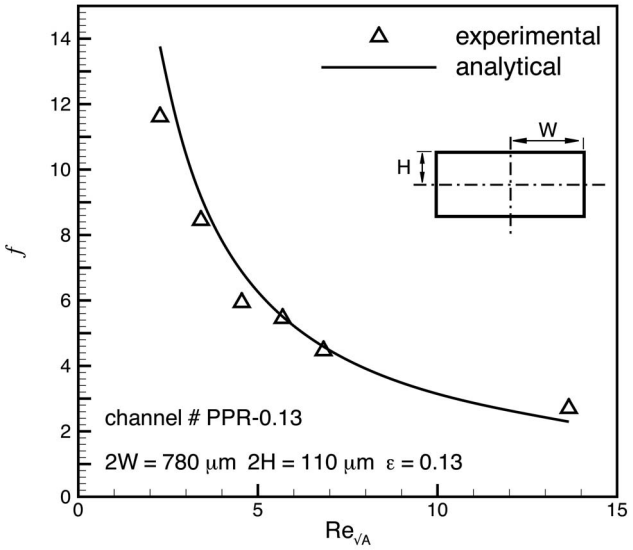

Fig. 4 Variation in friction factor with Reynolds number for sample no. PPR-0.13

assumed that the fluid properties remained constant. Equation (12) shows that the channel dimensions play an important role in determination of uncertainty by effecting three terms. Also for small Reynolds numbers, the accuracy of the flow rate becomes more significant. The uncertainty in the measurement of each parameter is listed in Table 4. Using Eq. (12) minimum uncertainties for the samples of PPR-0.13, PPR-0.17, PPR-0.4, PPR-0.6, and PPR-0.76 are 8.7%, 9.3%, 8.9%, 9.3%, and 11.1%, respectively.

5 Results and Discussion

Figures 4 and 5 show the comparison between friction factor obtained from Eq. (3), the solid line, and experimental data for two typical samples of PPR-0.13 and PPR-0.76, respectively. As shown, the trend and the values of experimental data are well predicted by the theoretical model. Consistent with the laminar flow in channels friction factor decreases with the Reynolds number.

Variation in the Poiseuille number, $f\ \mathrm{Re}_{\sqrt{A}}$, with the Reynolds number for different channels is shown in Fig. 6. Experimental data are normalized by the analytical model obtained from Eq. (3). The solid line shows the analytical model. From Eq. (3), it is clear that the Poiseuille number does not depend on the Reynolds number and it only varies with the aspect ratio of the channel cross section. The same trend can be observed in the experimental data. Large deviations from this trend in the very low Reynolds numbers attributed to the large uncertainties occur due to small flow rates and pressure drops. The Reynolds number can be a result of the small cross-sectional area and/or flow rate, with both parameters increasing the uncertainty in the value of the Poiseuille number, see Eq. (12). As can be seen, most of the experimental points fall within ±10% bounds of the analytical model.

Table 4 Uncertainty values for measured parameters

Parameter	Uncertainty
ΔP	±0.25% of full scale
L	±0.02 mm
W	±3.6 μm
H	±3.6 μm
Q	±0.5%

Another comparison of the present experimental work with analytical model is illustrated in Fig. 7. Since the Poiseuille number, $f\ \mathrm{Re}_{\sqrt{A}}$, remains constant for the laminar regime as the Reynolds number varies, the experimental data for each set were averaged over the laminar region. The ±10% bounds of the model are also shown in the plot to better demonstrate the agreement between the data and the model.

As shown in Eq. (3), the Poiseuille number, $f\ \mathrm{Re}_{\sqrt{A}}$, is only a function of the aspect ratio, which is a geometrical parameter. This dependency is plotted in Fig. 8. Averaged values over the studied range of the Reynolds number were used in this plot. It can be observed that for smaller aspect ratios, the Poiseuille number, $f\ \mathrm{Re}_{\sqrt{A}}$, increases sharply. To better show the trend of the analytical model, two asymptotes of very narrow and square cross sections are also included in Fig. 8. As can be seen, when $\varepsilon \to 0$, parallel plate, the Poiseuille number asymptotically approaches $4\pi^2/3\sqrt{\varepsilon}$.

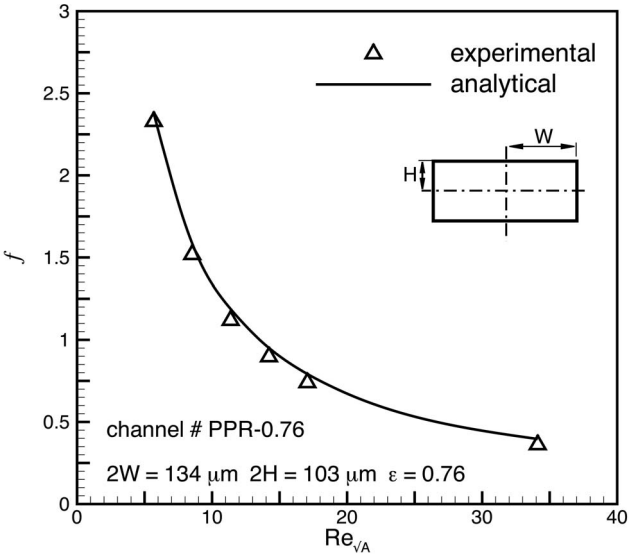

Fig. 5 Variation in friction factor with Reynolds number for sample no. PPR-0.76

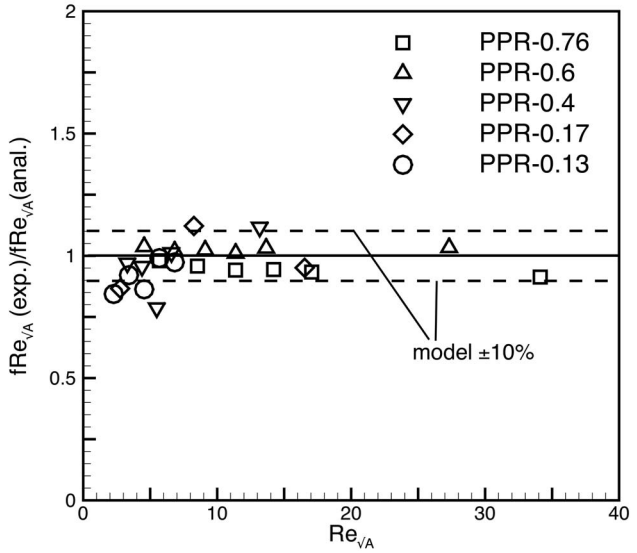

Fig. 6 Variation in Poiseuille number, $f\ \mathrm{Re}_{\sqrt{A}}$, with Reynolds number

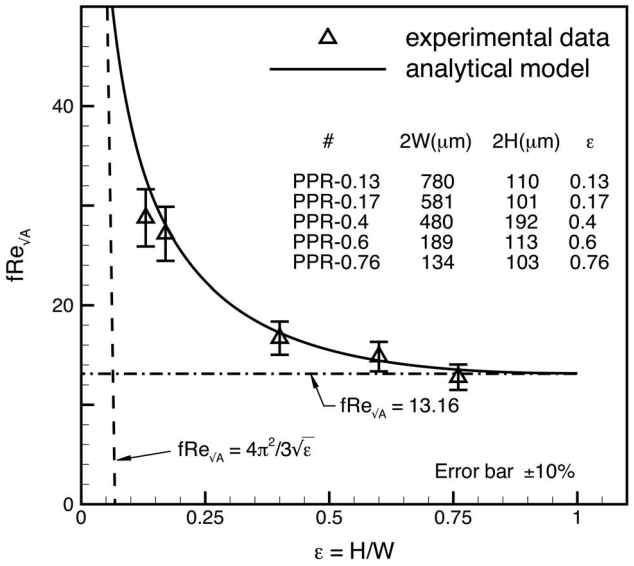

Fig. 8 Variation in Poiseuille number, $f\ \mathrm{Re}_{\sqrt{A}}$, with Reynolds number

It is beneficial to compare the results of present work with the existing data of rectangular microchannels. Data were collected from the works of Wu and Cheng [31], Lu and Garimella [32], and Gao et al. [33]. As shown in Fig. 9, the collected data cover a wide range of the aspect ratio for almost three decades. The solid line represents the analytical model of Bahrami et al. [1]. As can be seen, the analytical model agrees well with the experimental data over the wide range of microchannel cross-section aspect ratio.

6 Summary and Conclusions

The general model developed by Bahrami et al. [1,36] was experimentally validated for the case of rectangular cross-section microchannels. Frictional pressure drop measurements were conducted over a range of Reynolds numbers from 1 to 35 for rectangular cross-section microchannels fabricated with soft lithography method in the aspect ratio range of $0.13 < \varepsilon < 0.76$. A careful measurement of pressure drop and channel dimensions was conducted, and the pressure drops due to the developing region, minor losses, and electroviscous effect were estimated using available models in literature. Channel deformation due to the pressure inside the microchannel was found to be negligible since the pressure drop changes linearly with the flow rate. Comparing the results with the general theoretical model shows good agreement between the model and experimental data.

Uncertainty analysis showed that the measurement of channel dimensions and flow rate is critical in microscales. Here, microchannel cross-section geometry was determined through processing high quality images of the channel cross section.

According to the analytical model and experimental data of present work, the Poiseuille number, $f\ \mathrm{Re}_{\sqrt{A}}$, was found to be only a function of microchannel geometry in the range of Reynolds numbers studied in this work. For rectangular cross sections, the channel aspect ratio is the only parameter that affects the Poi-

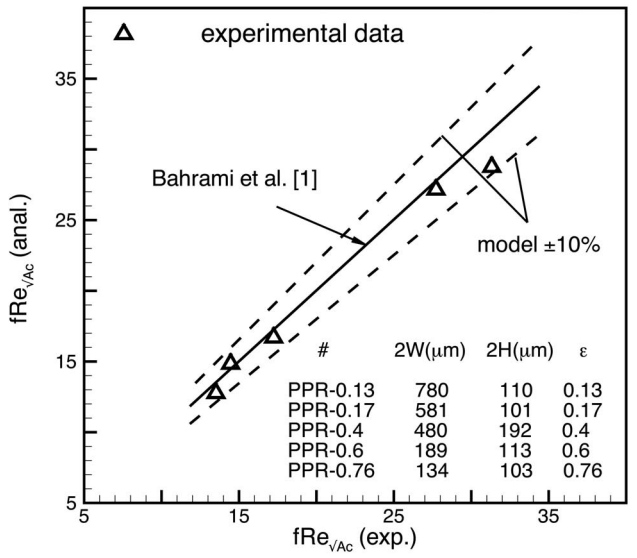

Fig. 7 Comparison of experimental data of present work with analytical model of Bahrami et al. [1]

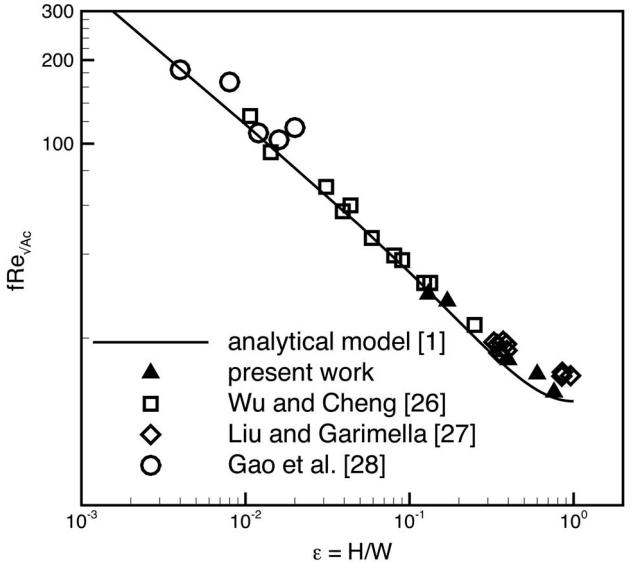

Fig. 9 Comparison between experimental data of present study and previous works

seuille number. The analytical model employed in this work will be applied to other channel geometries such as variable cross-section microchannels in our future work.

Acknowledgment

The authors gratefully acknowledge the financial support of the Natural Sciences and Engineering Research Council of Canada (NSERC). Also they thank Dr. Viatcheslav Berejnov and Mr. Ali K. Oskooi for their assistance.

Nomenclature

A = microchannel cross-sectional area, m^2
A_t = tubing cross-sectional area, m^2
c_p = fluid specific heat, J/kg K
Ec = Eckert number, $W^2/(2c_p\Delta T_{\text{ref}})$
f = Fanning friction factor
H = channel half height, m
I_p = polar momentum of inertia, m^4
I_p^* = specific polar momentum of inertia, I_p/A^2
K_b = loss coefficient for bend
K_c = flow contraction loss coefficient
K_e = flow expansion loss coefficient
L = channel length, m
L_D = developing region length, m
L^* = dimensionless length $L/\sqrt{A}$
Po = Poiseuille number, $f\ \text{Re}_{\sqrt{A}}$
Q = volumetric flow rate, m^3/s
$\text{Re}_{\sqrt{A}}$ = Reynolds number, $\rho Q/\mu\sqrt{A}$
W = channel half width, m

Greek

ΔP_b = bend pressure loss, Pa
ΔP_c = connecting tube pressure loss, Pa
ΔP_D = developing region pressure loss, Pa
ΔP_{ex} = exit pressure loss, Pa
ΔP_{FD} = fully developed pressure loss, Pa
ΔP_{ev} = pressure loss due to electroviscous effect, Pa
ΔP_{in} = inlet pressure loss, Pa
ε = channel aspect ratio, $2H/2W$
Γ = channel cross-section perimeter, m
μ = fluid viscosity, kg/m s
μ_a = apparent viscosity, kg/m s
μ_{eo} = electro-osmotic mobility, m^2/V s
ρ = fluid density, kg/m^3
σ_b = fluid electrical conductivity, S/m
ω = uncertainty

Appendix: Uncertainty Formulation

To calculate the uncertainty associated with the experimental measurements the following relation is used [43]:

$$\omega_R = \left[\sum \left(\frac{\partial R}{\partial x_i}\omega_i\right)^2\right]^{1/2} \tag{A1}$$

where ω_R is the uncertainty in results, $R(x_1, x_2, \ldots, x_n)$, and ω_i is the uncertainty of the independent variable x_i. If the results function, $R(x_1, x_2, \ldots, x_n)$, takes the form of a product of the independent variables, $R = x_1^{a_1} x_2^{a_2}, \ldots, x_n^{a_n}$, Eq. (A1) can be rewritten as

$$\frac{\omega_R}{R} = \left[\sum \left(\frac{a_i}{x_i}\omega_i\right)^2\right]^{1/2} \tag{A2}$$

The final form of the uncertainty of the Poiseuille number, Eq. (12), is obtained using Eqs. (10) and (A2).

To calculate the uncertainty of the channel cross section, $A = 4W \times H$, and perimeter, $\Gamma = 4(W+H)$, Eq. (A1) is employed

$$\omega_A = \left[\left(\frac{\partial A}{\partial W}\omega_W\right)^2 + \left(\frac{\partial A}{\partial H}\omega_H\right)^2\right]^{1/2} \tag{A3}$$

$$\omega_\Gamma = \left[\left(\frac{\partial \Gamma}{\partial W}\omega_W\right)^2 + \left(\frac{\partial \Gamma}{\partial H}\omega_H\right)^2\right]^{1/2} \tag{A4}$$

where $\partial A/\partial W = 4H$, $\partial A/\partial H = 4W$, $\partial \Gamma/\partial W = 4$, and $\partial \Gamma/\partial H = 4$.

References

[1] Bahrami, M., Yovanovich, M. M., and Culham, J. R., 2006, "Pressure Drop of Laminar, Fully Developed Flow in Microchannels of Arbitrary Cross-Section," ASME J. Fluids Eng., **128**, pp. 1036–1044.
[2] Whitesides, G. M., 2006, "The Origins and the Future of Microfluidics," Nature (London), **442**, pp. 368–372.
[3] Grushka, E., McCormick, R. M., and Kirkland, J. J., 1989, "Effect of Temperature Gradients on the Efficiency of Capillary Zone Electrophoresis Separations," Anal. Chem., **61**, pp. 241–246.
[4] Fletcher, P. D. I., Haswell, S. J., Pombo-Villar, E., Warrington, B. H., Watts, P., Wong, S., and Zhang, X., 2002, "Micro Reactors: Principles and Applications in Synthesis," Tetrahedron, **58**, pp. 4735–4757.
[5] DeWitt, S., 1999, "Microreactors for Chemical Synthesis," Curr. Opin. Chem. Biol., **3**(3), pp. 350–356.
[6] Miyake, R., Lammerink, S. J., Elwenspoek, M., and Fluitman, H. J., 1993, "Micro Mixer With Fast Diffusion," MEMS '93, Fort Lauderdale, FL, pp. 248–253.
[7] Weigl, B. H., Bardell, R. L., and Cabrera, C. R., 2003, "Lab-on-a-Chip for Drug Development," Adv. Drug Delivery Rev., **55**, pp. 349–377.
[8] Becker, H., and Locascio, L. E., 2002, "Polymer Microfluidic Devices," Talanta, **56**, pp. 267–287.
[9] Chovan, T., and Guttman, A., 2002, "Microfabricated Devices in Biotechnology and Biochemical Processing," Trends Biotechnol., **20**(3), pp. 116–122.
[10] Ehrfeld, W., 2003, "Electrochemistry and Microsystems," Electrochim. Acta, **48**, pp. 2857–2868.
[11] Bayraktar, T., and Pidugu, S. B., 2006, "Characterization of Liquid Flows in Microfluidic Systems," Int. J. Heat Mass Transfer, **49**, pp. 815–824.
[12] Peng, X. F., Peterson, G. P., and Wang, B. X., 1994, "Frictional Flow Characteristics of Water Flowing Through Rectangular Microchannels," Exp. Heat Transfer, **7**, pp. 249–64.
[13] Xu, B., Ooi, K. T., and Wong, N. T., 2000, "Experimental Investigation of Flow Friction for Liquid Flow in Microchannels," Int. Commun. Heat Mass Transfer, **27**, pp. 1165–1176.
[14] Ren, C. L., and Li, D., 2004, "Electroviscous Effects on Pressure-Driven Flow of Dilute Electrolyte Solutions in Small Microchannels," J. Colloid Interface Sci., **274**, pp. 319–330.
[15] Judy, J., Maynes, D., and Webb, B. W., 2002, "Characterization of Frictional Pressure Drop for Liquid Flows Through Microchannels," Int. J. Heat Mass Transfer, **45**, pp. 3477–3489.
[16] Tuckerman, D. B., and Peace, R. F. W., 1981, "High-Performance Heat Sinking for VLSI," IEEE Electron Device Lett., **2**, pp. 126–129.
[17] Mala, G. M., and Li, D., 1999, "Flow Characteristics of Water in Microtubes," Int. J. Heat Mass Transfer, **20**, pp. 142–148.
[18] Pfhaler, J., Harley, J., and Bau, H., 1990, "Liquid Transport in Micron and Submicron Channels," Sens. Actuators, A, **A21–A23**, pp. 431–434.
[19] Pfhaler, J., Harley, J., Bau, H., and Zemel, J. N., 1991, "Gas and Liquid Flow in Small Channels Micromechanical Sensors, Actuators, and Systems," ASME Dyn. Syst. Control Div., **32**, pp. 49–60.
[20] Urbanek, W., Zemel, J. N., and Bau, H. H., 1993, "An Investigation of the Temperature Dependence of Poiseuille Numbers in Microchannel Flow," J. Micromech. Microeng., **3**, pp. 206–208.
[21] Qu, W., Mala, G. M., and Li, D., 2000, "Pressure-Driven Water Flows in trapezoidal Silicon Microchannels," Int. J. Heat Mass Transfer, **43**, pp. 3925–3936.
[22] Papautsky, I., Brazzle, J., Ameel, T., and Frazier, A. B., 1999, "Laminar Fluid Behavior in Microchannels Using Micropolar Fluid Theory," Sens. Actuators, A, **73**, pp. 101–108.
[23] Ren, C. L., and Li, D., 2005, "Improved Understanding of the Effect of Electrical Double Layer on Pressure-Driven Flow in Microchannels," Anal. Chim. Acta, **531**, pp. 15–23.
[24] Weilin, Q., Mala, H. M., and Li, D., 2000, "Pressure-Driven Water Flows in Trapezoidal Silicon Microchannels," Int. J. Heat Mass Transfer, **43**, pp. 353–364.
[25] Guo, Z., and Li, Z., 2003, "Size Effect on Microscale Single-Phase Flow and Heat Transfer," Int. J. Heat Mass Transfer, **46**, pp. 149–159.
[26] Morini, G. L., 2005, "Viscous Heating in Liquid Flows in Microchannels," Int. J. Heat Mass Transfer, **48**, pp. 3637–3647.
[27] Bahrami, M., Yovanovich, M. M., and Culham, J. R., 2006, "Pressure Drop of Laminar, Fully Developed Flow in Rough Microtubes," ASME J. Fluids Eng., **128**, pp. 632–637.
[28] Jiang, X. N., Zhou, Z. Y., Huang, X. Y., and Liu, C. Y., 1997, "Laminar Flow Through Microchannels Used for Microscale Cooling Systems," IEEE/CPMT Electronic Packaging Technology Conference, pp. 119–122.
[29] Baviere, R., Ayela, F., Le Person, S., and Favre-Marinet, M., 2005, "Experimental Characterization of Water Flow Through Smooth Rectangular Microchannels," Phys. Fluids, **17**, p. 098105.
[30] Bucci, A., Celata, G. P., Cumo, M., Serra, E., and Zummo, G., 2003, "Water Single-Phase Fluid Flow and Heat Transfer in Capillary Tubes," International Conference on Microchannels and Minichannels, Vol. 1, pp. 319–326, ASME Paper No. 1037.

[31] Wu, H. Y., and Cheng, P., 2003, "Friction Factors in Smooth Trapezoidal Silicon Microchannels With Different Aspect Ratios," Int. J. Heat Mass Transfer, **46**, pp. 2519–2525.
[32] Liu, D., and Garimella, S., 2004, "Investigation of Liquid Flow in Microchannels," J. Thermophys. Heat Transfer, **18**, pp. 65–72.
[33] Gao, P., Le Person, S., and Favre-Marinet, M., 2002, "Scale Effects on Hydrodynamics and Heat Transfer in Two-Dimensional Mini and Microchannels," Int. J. Therm. Sci., **41**, pp. 1017–1027.
[34] Squires, T. M., and Quake, S. R., 2005, "Micro Fluidics: Fluid Physics at Nanoliter Scale," Rev. Mod. Phys., **77**, pp. 977–1026.
[35] White, F. M., 1974, *Viscous Fluid Flow*, McGraw-Hill, New York, Chap. 3.
[36] Bahrami, M., Yovanovich, M. M., and Culham, J. R., 2007, "A Novel Solution for Pressure Drop in Singly Connected Microchannels," Int. J. Heat Mass Transfer, **50**, pp. 2492–2502.
[37] Timoshenko, S. P., and Goodier, J. N., 1970, *Theory of Elasticity*, McGraw-Hill, New York, Chap. 10.
[38] Yovanovich, M. M., 1974, "A General Expression for Predicting Conduction Shape Factors," *AIAA Prog. in Astro. and Aeronautics: Thermophysics and Space Craft Control*, Vol. 35, R. G. Hering, ed., MIT Press, Cambridge, MA, pp. 265–291.
[39] Muzychka, Y. S., and Yovanovich, M. M., 2002, "Laminar Flow Friction and Heat Transfer in Non-Circular Ducts and Channels Part 1: Hydrodynamic Problem," Proceedings of Compact Heat Exchangers, A Festschrift on the 60th Birthday of Ramesh K. Shah, Grenoble, France, pp. 123–130.
[40] Shah, R. K., and London, A. L., 1978, *Laminar Flow Forced Convection in Ducts, Supplement to Advances in Heat Transfer*, Academic, New York.
[41] Erickson, D., Sinton, D., and Li, D., 2003, "Joule Heating and Heat Transfer in Poly(dimethylsiloxane) Microfluidic Systems," Lab Chip, **3**, pp. 141–149.
[42] McDonald, J. C., Duffy, D. C., Anderson, J. R., Chiu, D. T., Wu, H., Schueller, O. J. A., and Whiteside, G., 2000, "Fabrication of Microfluidic Systems in Poly(dimethylsiloxane)," Electrophoresis, **21**, pp. 27–40.
[43] Holman, J. P., 2001, *Experimental Methods for Engineering*, 7th ed., McGraw-Hill, New York, Chap. 3.
[44] Phillips, R. J., 1990, *Microchannel Heat Sinks, Advances in Thermal Modeling of Electronic Components and Systems*, Hemisphere, New York, Chap. 3.
[45] Sharp, K. V., Adrian, R. J., Santiago, J. G., and Molho, J. I., 2005, *Liquid Flows in Microchannels, MEMS Hand Book: Introduction and Fundamentals*, 2nd ed., Taylor & Francis, New York.
[46] Kandlikar, S. G., Garimella, S., Li, D., Colin, S., and King, M. R., 2006, *Heat Transfer and Fluid Flow in Minichannels and Microchannels*, Elsevier, Oxford.
[47] Steinke, M. E., and Kandlikar, S. G., 2006, "Single-Phase Liquid Friction Factors in Microchannels," Int. J. Therm. Sci., **45**, pp. 1073–1083.
[48] Kays, W. M., and London, A. L., 1984, *Compact Heat Exchangers*, McGraw-Hill, New York.
[49] Probstein, R. F., 1994, *Physicochemical Hydrodynamics*, 2nd ed., Wiley, New York.
[50] Masliyah, J. H., and Bhattacharjee, S., 2006, *Electrokinetic and Colloid Transport Phenomena*, Wiley, Englewood Cliffs, NJ.
[51] Lide, D., and Kehiaian, H. V., 1994, *CRC Handbook of Thermophysical and Thermochemical Data*, 1st ed., CRC Press, Florida.
[52] Lee, J. S. H., Hu, Y., and Li, D., 2005, "Electrokinetic Concentration Gradient Generation Using a Converging-Diverging Microchannel," Anal. Chim. Acta, **543**, pp. 99–108.
[53] Holden, M. A., Kumar, S., Beskok, A., and Cremer, P. S., 2003, "Microfluidic Diffusion Diluter: Bulging of PDMS Microchannels Under Pressure Driven Flow," J. Micromech. Microeng., **13**, pp. 412–418.
[54] Gervais, T., El-Ali, J., Gunther, A., and Jensen, K., 2006, "Flow-Induced Deformation of Shallow Microfluidic Channels," Lab Chip, **6**, pp. 500–507.

Appendix E

Laminar flow pressure drop in converging-diverging microtubes

(with permission from Taylor Francis)

Heat Transfer Engineering
Publication details, including instructions for authors and subscription information:
http://www.informaworld.com/smpp/title~content=t713723051

Laminar Fully Developed Flow in Periodically Converging-Diverging Microtubes

Mohsen Akbari[a]; David Sinton[b]; Majid Bahrami[a]
[a] Mechatronic Systems Engineering, School of Engineering Science, Simon Fraser University, Surrey, British Columbia, Canada [b] Department of Mechanical Engineering, University of Victoria, Victoria, British Columbia, Canada

Online publication date: 01 February 2010

To cite this Article Akbari, Mohsen , Sinton, David and Bahrami, Majid(2010) 'Laminar Fully Developed Flow in Periodically Converging-Diverging Microtubes', Heat Transfer Engineering, 31: 8, 628 — 634
To link to this Article: DOI: 10.1080/01457630903463404
URL: http://dx.doi.org/10.1080/01457630903463404

Heat Transfer Engineering, 31(8):628–634, 2010

ISSN: 0145-7632 print / 1521-0537 online
DOI: 10.1080/01457630903463404

Taylor & Francis
Taylor & Francis Group

Laminar Fully Developed Flow in Periodically Converging–Diverging Microtubes

MOHSEN AKBARI,[1] DAVID SINTON,[2] and MAJID BAHRAMI[1]

[1]Mechatronic Systems Engineering, School of Engineering Science, Simon Fraser University, Surrey, British Columbia, Canada
[2]Department of Mechanical Engineering, University of Victoria, Victoria, British Columbia, Canada

Laminar fully developed flow and pressure drop in linearly varying cross-sectional converging–diverging microtubes have been investigated in this work. These microtubes are formed from a series of converging–diverging modules. An analytical model is developed for frictional flow resistance assuming parabolic axial velocity profile in the diverging and converging sections. The flow resistance is found to be only a function of geometrical parameters. To validate the model, a numerical study is conducted for the Reynolds number ranging from 0.01 to 100, for various taper angles, from 2 to 15 degrees, and for maximum–minimum radius ratios ranging from 0.5 to 1. Comparisons between the model and the numerical results show that the proposed model predicts the axial velocity and the flow resistance accurately. As expected, the flow resistance is found to be effectively independent of the Reynolds number from the numerical results. Parametric study shows that the effect of radius ratio is more significant than the taper angle. It is also observed that for small taper angles, flow resistance can be determined accurately by applying the locally Poiseuille flow approximation.

INTRODUCTION

There are numerous instances of channels that have streamwise-periodic cross sections. It has been experimentally and numerically observed that the entrance lengths of fluid flow and heat transfer for such streamwise-periodic ducts are much shorter than those of plain ducts, and quite often, three to five cycles can make both the flow and heat transfer fully developed [1]. In engineering practice the streamwise length of such ducts is usually much longer than several cycles; therefore, theoretical works for such ducts often focus on the periodically fully developed fluid flow and heat transfer. Rough tubes or channels with ribs on their surfaces are examples of streamwise-periodic ducts that are widely used in the cooling of electronic equipment and gas turbine blades, as well as in high-performance heat exchangers.

The authors are grateful for the financial support of the Natural Sciences and Engineering Research Council (NSERC) of Canada and the Canada Research Chairs Program.

Address correspondence to Mohsen Akbari, Mechatronic Systems Engineering, School of Engineering Science, Simon Fraser University, Surrey, BC, V3T 0A3, Canada. E-mail: maa59@sfu.ca

Many researchers have conducted experimental or numerical investigations on the flow and heat transfer in streamwise-periodic wavy channels. Most of these works are based on numerical methods. Sparrow and Prata [1] performed a numerical and experimental investigation for laminar flow and heat transfer in a periodically converging–diverging conical section for the Reynolds number range from 100 to 1000. They showed that the pressure drop for the periodic converging–diverging tube is considerably greater than for the straight tube, while Nusselt number depends on the Prandtl number. For $Pr < 1$, the periodic tube Nu is generally lower than the straight tube, but for $Pr > 1$, Nu is slightly greater than for a straight tube. Wang and Vanka [2] used a numerical scheme to study the flow and heat transfer in periodic sinusoidal passages. Their results revealed that for steady laminar flow, pressure drop increases more significantly than heat transfer. The same result is reported in Niceno and Nobile [3] and Wang and Chen [4] numerical works for the Reynolds number range from 50 to 500. Hydrodynamic and thermal characteristics of a pipe with periodically converging–diverging cross section were investigated by Mahmud et al. [5], using a finite-volume method. A correlation was proposed for calculating the friction factor, in sinusoidal wavy tubes for Reynolds number ranging from 50 to 2,000. Stalio

and Piller [6], Bahaidarah [7], and Naphon [8] also studied the flow and heat transfer of periodically varying cross-section channels. An experimental investigation on the laminar flow and mass transfer characteristics in an axisymmetric sinusoidal wavy-walled tube was carried out by Nishimura et al. [9]. They focused on the transitional flow at moderate Reynolds numbers (50 to 1,000). Russ and Beer [10] also studied heat transfer and flow in a pipe with sinusoidal wavy surface. They used both numerical and experimental methods in their work for the Reynolds number range of 400 to 2,000, where the flow regime is turbulent.

For low Reynolds numbers, Re $\sim$ 0(1), some analytical and approximation methods have been carried out in the case of gradually varying cross section. In particular, Burns and Parkes [11] developed a perturbation solution for the flow of viscous fluid through axially symmetric pipes and symmetrical channels with sinusoidal walls. They assumed that the Reynolds number is small enough for the Stokes flow approximation to be made and found stream functions in the form of Fourier series. Manton [12] proposed the same method for arbitrary shapes. Langlois [13] analyzed creeping viscous flow through a circular tube of arbitrary varying cross section. Three approximate methods were developed with no constriction on the variation of the wall. MacDonald [14] and more recently Brod [15] have also studied the flow and heat transfer through tubes of nonuniform cross section.

The low Reynolds number flow regime is the characteristic of flows in microchannels [16]. Microchannels with converging–diverging sections maybe fabricated to influence cross-stream mixing [17–20] or result from fabrication processes such as micromachining or soft lithography [21].

Existing analytical models provide solutions in a complex format, generally in a form of series, and are not amicable to engineering or design. Also, existing model studies did not include direct comparison with numerical or experimental data. In this study, an approximate analytical solution has been developed for velocity profile and pressure drop of laminar, fully developed, periodic flow in a converging–diverging microtube, and results of the model are compared with those of an independent numerical method. Results of this work can be then applied to more complex wall geometries.

PROBLEM STATEMENT

Consider an incompressible, constant property, Newtonian fluid which flows in steady, fully developed, pressure-driven laminar regime in a fixed cross section tube of radius a_0. At the origin of the axial coordinate, $z = 0$, the fluid has reached a fully developed Poiseuille velocity profile, $u(r) = 2u_{m,0}[1 - (\frac{r}{a_0})^2]$, where $u_{m,0}$ is the average velocity. The cross-sectional area for flow varies linearly with the distance z in the direction of flow, but retains axisymmetric about the z-axis. Figure 1 illustrates the geometry and the coordinates for a converging tube; one may similarly envision a diverging tube.

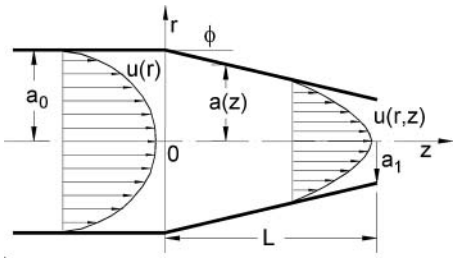

Figure 1 Geometry of slowly varying cross-section microtube.

The governing equations for this two-dimensional (2-D) flow are:

$$\frac{1}{r}\frac{\partial}{\partial r}(rv) + \frac{\partial u}{\partial z} = 0 \tag{1}$$

$$\rho\left(v\frac{\partial u}{\partial r} + u\frac{\partial u}{\partial z}\right) = -\frac{\partial P}{\partial z} + \mu\left\{\frac{1}{r}\frac{\partial}{\partial r}\left[r\frac{\partial u}{\partial r}\right] + \frac{\partial^z u}{\partial z^2}\right\} \tag{2}$$

$$\rho\left(v\frac{\partial v}{\partial r} + u\frac{\partial v}{\partial z}\right) = -\frac{\partial P}{\partial r} + \mu\left\{\frac{\partial}{\partial r}\left[\frac{1}{r}\frac{\partial}{\partial r}(rv)\right] + \frac{\partial^2 v}{\partial z^2}\right\} \tag{3}$$

with boundary conditions

$$u(r, z) = 0,\ v(r, z) = 0; \quad r = a(z) \tag{4}$$

$$u(r, 0) = 2u_{m,0}\left[1 - \left(\frac{r}{a_0}\right)^2\right]; \quad z = 0$$

$$P(r, 0) = P_0$$

In this work we seek an approximate method to solve this problem.

MODEL DEVELOPMENT

The premise of the present model is that the variation of the duct cross section with the distance along the direction of the flow is sufficiently gradual that the axial component of the velocity profile $u(r, z)$ remains parabolic. To satisfy the requirements of the continuity equation, the magnitude of the axial velocity must change, i.e.,

$$u(r, z) = 2u_m(z)\left[1 - \left(\frac{r}{a(z)}\right)^2\right] \tag{5}$$

where $u_m(z)$ is the mean velocity at the axial location z and can be related to the mean velocity $u_{m,0}$ at the origin $z = 0$, and using conservation of mass as

$$u_m(z) = \left[\frac{a_0}{a(z)}\right]^2 u_{m,0} \tag{6}$$

Then the axial velocity profile $u(r, z)$ becomes

$$u(r, z) = 2u_{m,0}\left[\frac{a_0}{a(z)}\right]^2\left[1 - \left(\frac{r}{a\,(z)}\right)^2\right] \tag{7}$$

Substituting Eq. (7) into the continuity equation, Eq. (1), and integrating leads to

$$v(r,z) = 2m\eta u_{m,0}\left[\frac{a_0}{a(z)}\right]^2\left[1-\left(\frac{r}{a(z)}\right)^2\right] \tag{8}$$

where $m = \frac{da(z)}{dz}$ is the wall slope and $\eta = \frac{r}{a(z)}$.

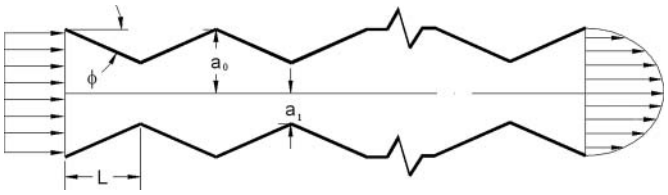

Figure 2 Schematic of the periodic converging–diverging microtube.

PRESSURE DROP AND FLOW RESISTANCE

Comparing Eqs. (7) and (8) reveals that $\frac{v}{u} = m\eta$; thus, one can conclude that if m is small enough, v will be small and the pressure gradient in the r direction can be neglected with respect to pressure gradient in the z direction.

Knowing both velocities and neglecting $\frac{\partial P}{\partial r}$, pressure drop in a converging–diverging module can be obtained by integrating Eq. (2). The final result after simplification is

$$\Delta P = \frac{16\mu u_{m,0}L}{a_0^2}\left[\frac{\varepsilon^2+\varepsilon+1}{3\varepsilon^2}+\frac{m^2(1+\varepsilon)}{2\varepsilon^5}\right] \tag{9}$$

where ΔP is the difference of average pressure at the module inlet and outlet, a_0 and a_1 are the maximum and minimum radiuses of the tube, respectively, $m = \tan\phi$ is the slope of the tube wall, and $\varepsilon = \frac{a_1}{a_0}$ is the minimum–maximum radius ratio.

Defining flow resistance with an electrical network analogy in mind [22],

$$R_f = \frac{\Delta P}{Q} \tag{10}$$

where $Q = \pi a_0^2 u_{m,0}$, the flow resistance of a converging–diverging module becoms

$$R_f = \frac{16\mu L}{\pi a_0^4}\left[\frac{\varepsilon^2+\varepsilon+1}{3\varepsilon^2}+\frac{m^2(1+\varepsilon)}{2\varepsilon^5}\right] \tag{11}$$

At the limit when $m = 0$, Eq. (11) recovers the flow resistance of a fixed-cross-section tube of radius a_0, i.e.

$$R_{f,0} = \frac{16\mu L}{\pi a_0^4} \tag{12}$$

In dimensionless form,

$$R_f^* = \left[\frac{\varepsilon^2+\varepsilon+1}{3\varepsilon^2}+\frac{m^2(1+\varepsilon)}{2\varepsilon^5}\right] \tag{13}$$

The concept of flow resistance, Eq. (10), can be applied to complex geometries by constructing resistance networks to analyze the pressure drop.

For small taper angles ($\phi \le 10^\circ$), the term containing m^2 becomes small, and thus Eq. (13) reduces to

$$R_f^* = \frac{\varepsilon^2+\varepsilon+1}{3\varepsilon^2} \tag{14}$$

The maximum difference between the dimensionless flow resistance, R_f^*, obtained from Eq. (13) and that from Eq. (14) is 6% for $\phi = 1^\circ$. Equation (14) can also be derived from the locally Poiseuille approximation. With this approximation, the frictional resistance of an infinitesimal element in a gradually varying cross-section microtube is assumed to be equal to the flow resistance of that element with a straight wall. Equation (14) is used for comparisons with numerical data.

NUMERICAL ANALYSIS

To validate the present analytical model, 15 modules of converging–diverging tubes in a series were created in a finite-element-based commercial code, COMSOL 3.2 (www.comsol.com). Figure 2 shows the schematic of the modules considered in the numerical study. Two geometrical parameters, taper angle, ϕ, and minimum–maximum radius ratio, $\varepsilon = \frac{a_1}{a_0}$, were varied from 0 to 15° and 0.5 to 1, respectively. The working fluid was considered to be Newtonian with constant fluid properties. A Reynolds number range from 0.01 to 100 was considered. Despite the model is developed based on the low Reynolds numbers, higher Reynolds numbers (Re $\sim$ 100) were also investigated to evaluate the limitations of the model with respect to the flow condition. A structured, mapped mesh was used to discretize the numerical domain. Equations (1)–(3) were solved as the governing equations for the flow for steady-state condition. A uniform velocity boundary condition was applied to the flow inlet. Since the flow reaches streamwise fully developed condition in a small distance from the inlet, the same boundary conditions as Eq. (4) can be found at each module inlet. A fully developed boundary condition was assumed for the outlet, $\frac{\partial}{\partial z} = 0$. A grid refinement study was conducted to ensure accuracy of the numerical results. Calculations were performed with grids of 3 × 6, 6 × 12, 12 × 24, and 24 × 48 for each module for various Reynolds numbers and geometrical configurations. The value of dimensionless flow resistance, R_f^*, was monitored since the velocity profile in any cross section remained almost unchanged with the mesh refinement. Figure 3 shows the effect of mesh resolution on R_f^* for $\phi = 10^\circ$, $\varepsilon = \frac{a_1}{a_0} = 0.95$, and Re = 10. As can be seen, the value of R_f^* changes slower when the mesh resolution increases. The fourth mesh, i.e., 24 × 48, was considered in this study for all calculations to optimize computation cost and the solution accuracy.

The effect of the streamwise length on the flow has been shown in Figures 4 and 5. Dimensionless velocity profile, $u^* = \frac{u}{u_{\max(z)}}$, is plotted at $\beta = \frac{a_0}{a(z)} = 1.025$ for the second to fifth

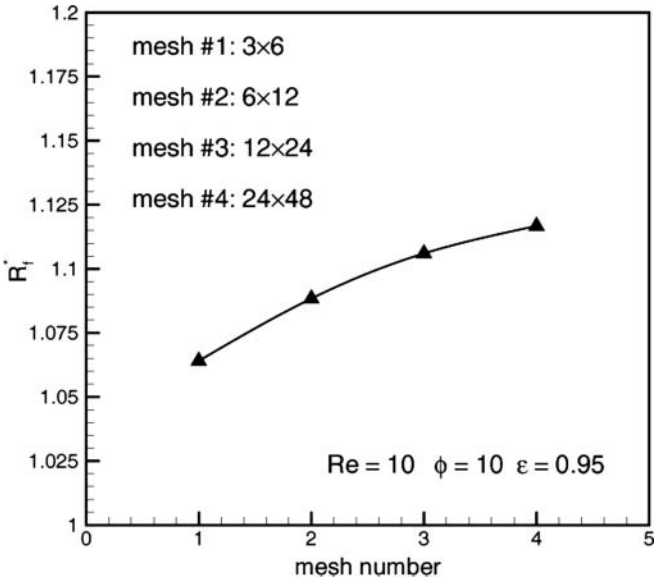

Figure 3 Mesh independency analysis.

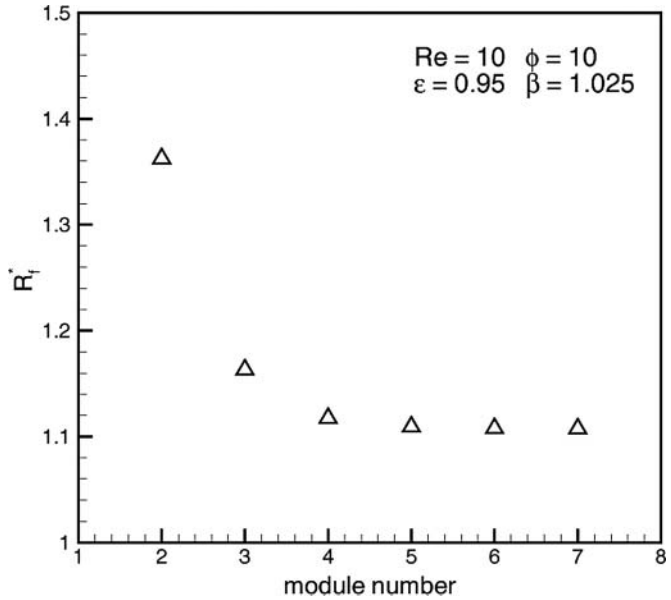

Figure 5 Effect of module number on the dimensionless flow resistance.

modules as well as the dimensionless flow resistance, R_f^* for the second to seventh modules for the typical values of $\phi = 10^\circ$, $\varepsilon = \frac{a_1}{a_0} = 0.95$, and $\mathrm{Re} = 10$. Both velocity profile and dimensionless flow resistance do not change after the forth module, which indicates that the flow after the fourth module is fully developed. The same behavior was observed for the geometrical parameters and Reynolds numbers considered in this work. Values of the modules in the fully developed region were used in this work.

Good agreement between the numerical and analytical model can be seen in Figure 6, where the dimensionless frictional flow resistance, R_f^*, is plotted over a wide range of the Reynolds number, $Re = \frac{2\rho u_{m,0} a_0}{\mu}$. The upper and lower dashed lines represent the bounds of nondimensional flow resistance for the investigated microtube. $R_{f,0}^*$ is the flow resistance of a uniform cross-sectional tube with the radius of a_0, and as expected its value is unity. $R_{f,1}^*$ stands for the flow resistance of a tube with the radius of a_1. Since the average velocity is higher for the tube of radius a_1, the value of $R_{f,1}^*$ is higher than the value of $R_{f,0}^*$. Both numerical and analytical results show the flow resistance to be effectively independent of Reynolds number, in keeping with low Reynolds number theory. For low Reynolds numbers, in the absence of instabilities, flow resistance is independent of the Reynolds number.

Table 1 lists the comparison between the present model, Eq. (14), and the numerical results over the wide range of minimum–maximum radius ratio, $0.5 \leq \varepsilon \leq 1$, three typical Reynolds numbers of $\mathrm{Re} = 1$, 10, and 100, and taper angles of $\phi = 2.7^\circ$ and 15°. The model is originally developed for small wall taper angles, $\phi \leq 10$, and low Reynolds numbers, $\mathrm{Re} \sim 0(1)$; however,

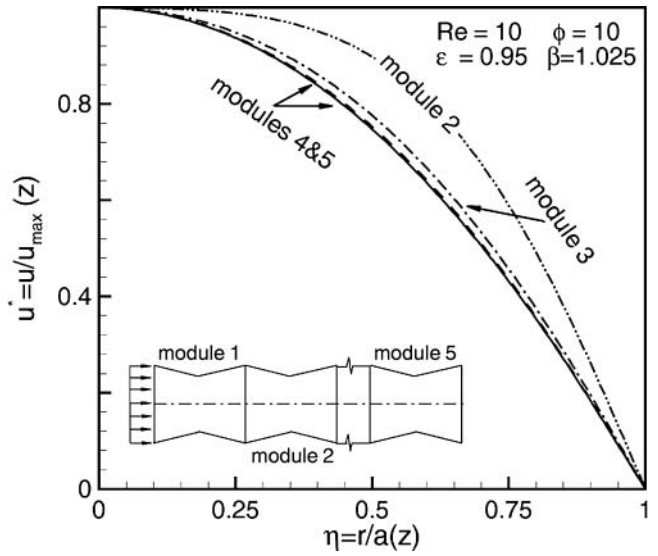

Figure 4 Effect of the streamwise length.

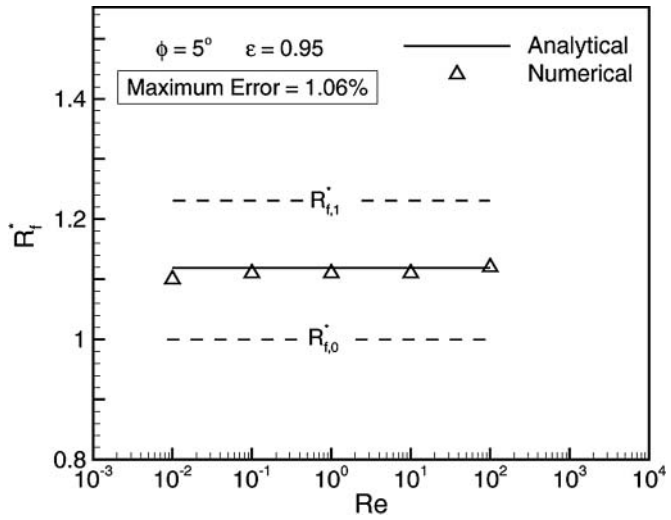

Figure 6 Variation of R_f^* with the Reynolds number, $\phi = 10$, and $\varepsilon = 0.95$.

Table 1 Comparison of the proposed model and the numerical results

				$\phi = 2$			
		Re = 1		Re = 10		Re = 100	
ε	Model	Numerical	Error (%)	Numerical	Error (%)	Numerical	Error (%)
0.5	4.67	4.59	–1.7	4.59	–1.7	4.96	+6.2
0.6	3.02	2.97	–1.7	2.98	–1.7	3.14	+3.7
0.7	2.13	2.09	–1.7	2.09	–1.7	2.17	+1.9
0.8	1.59	1.56	–1.8	1.56	–1.8	1.59	+0.0
0.9	1.24	1.21	–2.2	1.22	–1.6	1.23	–0.8
1	1	1	0.0	1	0.0	1	0.0
				$\phi = 7$			
0.5	4.67	4.67	0.0	4.72	+1.2	6.00	+28.6
0.6	3.02	3.02	0.0	3.05	+0.9	3.55	+17.2
0.7	2.13	2.13	–0.2	2.14	+0.7	2.33	+9.7
0.8	1.59	1.59	–0.6	1.60	+0.7	1.66	+4.5
0.9	1.24	1.24	0.0	1.24	0.0	1.25	+0.6
1	1	1	1.0	1	0.0	1	0.0
				$\phi = 15$			
0.5	4.67	5.01	+7.3	5.25	+12.4	7.33	+57.0
0.6	3.02	3.24	+7.3	3.33	+10.0	4.11	+36.0
0.7	2.13	2.26	+6.2	2.32	+8.9	2.57	+20.7
0.8	1.59	1.67	+5.4	1.70	+6.7	1.76	+10.7
0.9	1.24	1.28	+3.4	1.29	+3.7	1.32	+6.8
1	1	1	0.0	1	0.0	1	0.0

$Re = \frac{2\rho u_{m,0} a_0}{\mu}$ $Error\% = \frac{R^*_{f,\,model} - R^*_{f,\,numerical}}{R^*_{f,\,model}}$

as can be seen in Table 1, the proposed model can be used for wall taper angles up to 15°, when Re < 10, with acceptable accuracy. Note that the model shows good agreement with the numerical data for higher Reynolds numbers, up to 100, when $\varepsilon > 0.8$. Instabilities in the laminar flow due to high Reynolds numbers and/or large variations in the microchannel cross section result in the deviations of the analytical model from the numerical data.

PARAMETRIC STUDIES

Effects of two geometrical parameters—minimum–maximum radius ratio, ε, and taper angle, ϕ—are investigated and shown in Figures 7 and 8. Input parameters of two typical converging–diverging microtube modules are shown in Table 2. In the first case, the effect of $\varepsilon = \frac{a_1}{a_0}$ on the flow resistance was studied when taper angle, $\phi = 7$, was kept constant. As shown in Figure 7, both numerical and analytical results indicate that the frictional flow resistance, R_f, decreases by increasing of the minimum–maximum radius ratio, ε. For a constant taper angle, increase of $\varepsilon = \frac{a_1}{a_0}$ increases the module length as well as the average fluid velocity. Hence, higher flow resistance can be observed in Figure 7 for smaller values of ε. For better physical interpretation, flow resistances of two straight microtubes

Table 2 Input parameters for two typical microtubes

Parameter	Value
a_0	500 μm
Re	10
Case 1	
$\phi = 7$	
$0.5 < \varepsilon < 1$	
Case 2	
$\varepsilon = 0.8$	
$2 \le \phi \le 15$	

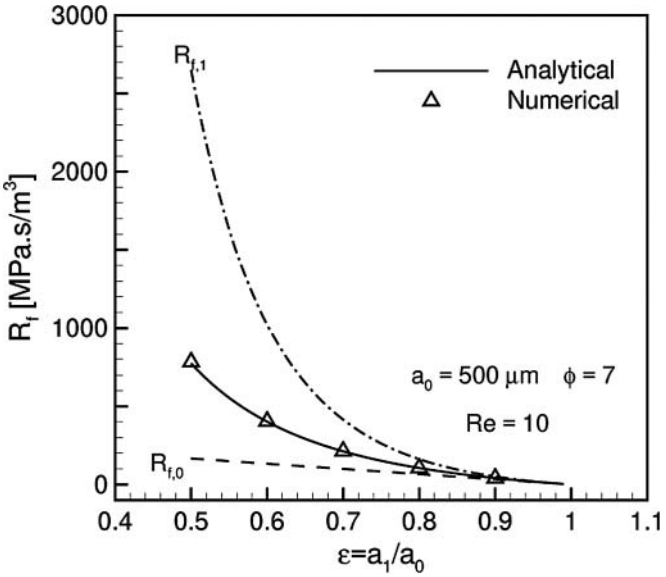

Figure 7 Effect of ε on the flow resistance, $\phi = 7$, and Re = 10.

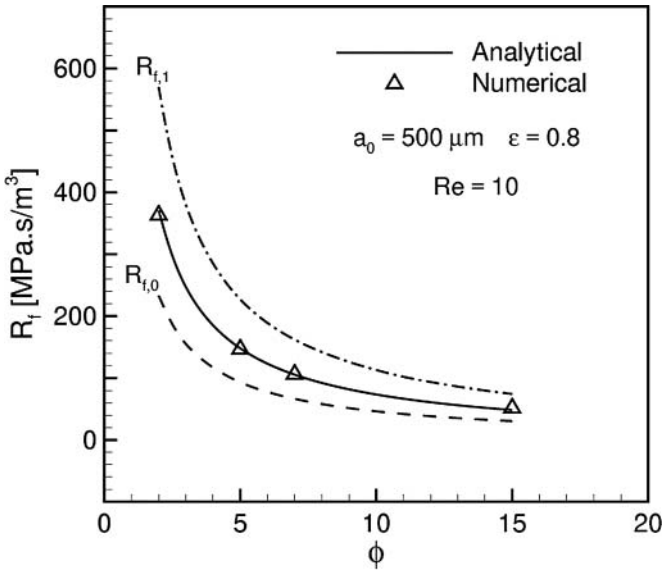

Figure 8 Effect of ϕ on the flow resistance, $\varepsilon = 0.8$, and $\mathrm{Re} = 10$.

with the maximum and minimum module radiuses are plotted in Figure 7. Since the total length of the module increases inversely with ε, a slight increase in $R_{f,0}$ can be observed. On the other hand, the flow resistance of the microtube with the minimum radius of the module $R_{f,1}$ increases sharply when ε becomes smaller. Keeping in mind that the flow resistance is inversely related to the fourth power of the radius, Eq. (12), and a_1 changes with ε, sharp variation of $R_{f,1}$ can be observed in Figure 7.

Variation of the flow resistance with respect to the taper angle when the minimum–maximum radius ratio, $\varepsilon = \frac{a_1}{a_0}$, was kept constant is plotted in Figure 8. Since a_1 remains constant in this case, the only parameter that has an effect on the flow resistance is the variation of the module length with respect to the taper angle. Both $R_{f,0}$ and $R_{f,1}$ increase inversely with the taper angle ϕ in a similar manner.

The effect of the module length can be eliminated by nondimensionalizing the module flow resistance with respect to the flow resistance of a straight microtube. Dimensionless flow resistance with the definition of Eq. (12) was used in Figure 9. As can be seen, the taper angle ϕ effect is negligible while the controlling parameter is the minimum–maximum radius ratio, ε.

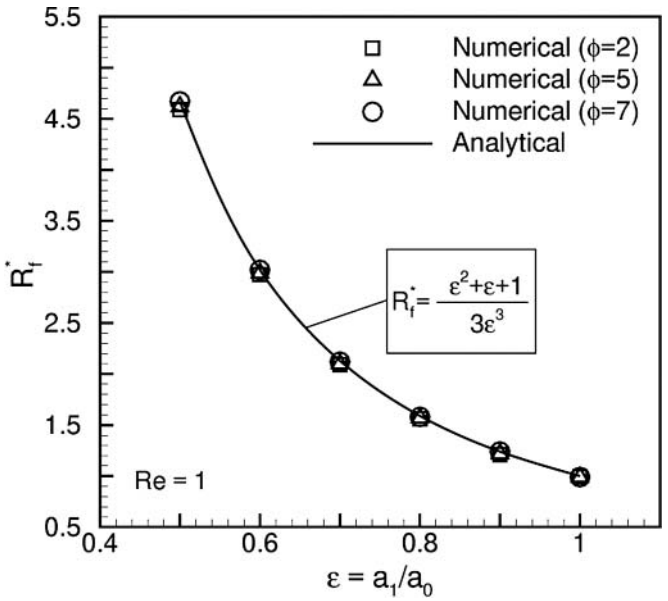

Figure 9 Effect of ϕ and ε on R_f^*, $\mathrm{Re} = 1$.

SUMMARY AND CONCLUSIONS

Laminar fully developed flow and pressure drop in gradually varying cross-sectional converging–diverging microtubes have been investigated in this work. A compact analytical model has been developed by assuming that the axial velocity profile remains parabolic in the diverging and converging sections. To validate the model, a numerical study has been performed. For the range of Reynolds number and geometrical parameters considered in this work, numerical observations show that the parabolic assumption of the axial velocity is valid. The following results are also found through analysis:

- For small taper angles ($\phi \leq 10$), effect of the taper angle on the dimensionless flow resistance, R_f^* can be neglected with less than 6% error and the local Poiseuille approximation can be used to predict the flow resistance.
- It has been observed through the numerical analysis that the flow becomes fully developed after less than five modules of length.
- Comparing the present analytical model with the numerical data shows good accuracy of the model to predict the flow resistance for $\mathrm{Re} < 10$, $\phi \leq 10$, and $0.5 \leq \varepsilon \leq 1$. See Table 1 for more details.
- The effect of minimum–maximum radius ratio, ε, is found to be more significant than taper angle, ϕ on the frictional flow resistance.

As an extension of this work, an experimental investigation to validate the present model and numerical analysis is in progress.

NOMENCLATURE

$a(z)$	=	radius of tube, m
a_0	=	maximum radius of tube, m
a_1	=	minimum radius of tube, m
L	=	half of module length, m
m	=	slope of tube wall, [—]
Q	=	volumetric flow rate, m^3/s
r, z	=	cylindrical coordinate, m
Re	=	Reynolds number, $\frac{2\rho u_{m,0} a_0}{\mu}$
R_f	=	frictional resistance, $pa\frac{s}{m^3}$
R_f^*	=	normalized flow resistance, $\frac{R_f}{R_{f,0}}$
u_m	=	mean fluid axial velocity, m/s
u, v	=	velocity in z and r directions, m/s

Greek Symbols

β = $\frac{a_0}{a(z)}$
η = $\frac{r}{a(z)}$
ε = $\frac{a_1}{a_0}$
ρ = fluid density, kg/m^3
μ = fluid viscosity, kg/m-s
ϕ = angle of tube wall, [—]
ΔP = pressure drop, Pa

REFERENCES

[1] Sparrow, E. M., and Prata, A. T., Numerical Solutions for Laminar Flow and Heat Transfer in a Periodically Converging–Diverging Tube With Experimental Confirmation, *Numerical Heat Transfer*, vol. 6, pp. 441–461, 1983.

[2] Wang, G., and Vanka, S. P., Convective Heat Transfer in Periodic Wavy Passages, *International Journal of Heat and Mass Transfer*, vol. 38, no. 17, pp. 3219–3230, 1995.

[3] Niceno, B., and Nobile, E., Numerical Analysis of Fluid Flow and Heat Transfer in Periodic Wavy Channels, *International Journal of Heat and Fluid Flow*, vol. 22, pp. 156–167, 2001.

[4] Wang, C. C., and Chen, C. K., Forced Convection in a Wavy Wall Channel, *International Journal of Heat and Mass Transfer*, vol. 45, pp. 2587–2595, 2002.

[5] Mahmud, S., Sadrul Islam, A. K. M., and Feroz, C. M., Flow and Heat Transfer Characteristics Inside a Wavy Tube, *Journal of Heat and Mass Transfer*, vol. 39, pp. 387–393, 2003.

[6] Stalio, E., and Piller, M., Direct Numerical Simulation of Heat Transfer in Converging–Diverging Wavy Channels, *ASME Journal of Heat Transfer*, vol. 129, pp. 769–777, 2007.

[7] Bahaidarah, M. S. H., A Numerical Study of Fluid Flow and Heat Transfer Characteristics in Channels With Staggered Wavy Walls, *Journal of Numerical Heat Transfer*, vol. 51, pp. 877–898, 2007.

[8] Naphon, P., Laminar Convective Heat Transfer And Pressure Drop in the Corrugated Channels, *International Communications in Heat and Mass Transfer*, vol. 34, pp. 62–71, 2007.

[9] Nishimura, T., Bian, Y. N., Matsumoto, Y., and Kunitsugu, K., Fluid Flow and Mass Transfer Characteristics in a Sinusoidal Wavy-Walled Tube at Moderate Reynolds Numbers for Steady Flow, *Journal of Heat and Mass Transfer*, vol. 39, pp. 239–248, 2003.

[10] Russ, G., and Beer, H., Heat Transfer and Flow Field in A Pipe With Sinusoidal Wavy Surface—Ii: Experimental Investigation, *International Journal of Heat and Mass Transfer*, vol. 40, no. 5, pp. 1071–1081, 1997.

[11] Burns, J. C., and Parkes, T., Peristaltic Motion, *Journal of Fluid Mechanics*, vol. 29, pp. 731–743, 1967.

[12] Manton, M. J., Low Reynolds Number Flow in Slowly Varying Axisymmetric Tubes, *Journal of Fluid Mechanics*, vol. 49, pp. 451–459, 1971.

[13] Langlois, W. E., Creeping Viscous Flow Through a Circular Tube of Non-Uniform Cross- Section, *ASME Journal of Applied Mechanics*, vol. 39, pp. 657–660, 1972.

[14] MacDonald, D. A., Steady Flow in Tubes of Slowly Varying Cross-Section, *ASME Journal of Applied Mechanics*, vol. 45, pp. 475–480, 1978.

[15] Brod, H., Invariance Relations for Laminar Forced Convection In Ducts With Slowly Varying Cross Section, *International Journal of Heat and Mass Transfer*, vol. 44, pp. 977–987, 2001.

[16] Squires, T. M., and Quake, S. R., Microfluidics: Fluid Physics at Nano-Liter Scale, *Review of Modern Physics*, vol. 77, pp. 977–1026, 2005.

[17] Lee, S. H., Yandong, H., and Li, D., Electrokinetic Concentration Gradient Generation Using a Converging–Diverging Microchannel, *Analytica Chimica Acta*, vol. 543, pp. 99–108, 2005.

[18] Hung, C. I., Wang, K., and Chyou, C., Design and Flow Simulation of a New Micromixer, *JSME International Journal*, vol. 48, no. 1, pp. 17–24, 2005.

[19] Hardt, S., Drese, K. S., Hessel, V., and Schonfeld, F., Passive Micromixers for Applications in the Microreactor and μ-TAS Fields, *Microfluids and Nanofluids*, vol. 1, no. 2, pp. 108–118, 2005.

[20] Chung, C. K., and Shih, T. R., Effect of Geometry on Fluid Mixing of the Rhombic Micromixers, *Microfluids and Nanofluids*, vol. 4, pp. 419–425, 2008.

[21] McDonald, J. C., Duffy, D. C., Anderson, J. R., Chiu, D. T., Wu, H., Schueller, O. J., and Whiteside, G. M., Fabrication of Microfluidic Systems in Poly(demethylsiloxane), *Electrophoresis*, vol. 21, pp. 27–40, 2000.

[22] Bahrami, M., Yovanovich, M. M., and Culham, J. R., Pressure Drop of Fully-Developed, Laminar Flow in Rough Microtubes, *ASME Journal of Fluids Engineering*, vol. 128, pp. 632–637, 2006.

Mohsen Akbari is a Ph.D. student at Mechatronic System Engineering, School of Engineering Science, Simon Fraser University, Canada. He received his bachelor's and master's degrees from Sharif University of Technology, Iran, in 2002 and 2005. Currently, he is working on transport phenomena at micro and nano scales with applications in biomedical diagnosis and energy systems.

David Sinton received the B.Sc. degree from the University of Toronto, Toronto, Ontario, Canada, in 1998, the M.Sc. degree from McGill University, Montreal, Quebec, Canada, in 2000, and the Ph.D. degree from the University of Toronto in 2003, all in mechanical engineering. He is currently an associate professor in the Department of Mechanical Engineering, University of Victoria, Victoria, British Columbia, Canada. His research interests are in microfluidics and nanofluidics and their application in biomedical diagnostics and energy systems.

Majid Bahrami is an assistant professor with the School of Engineering at the Simon Fraser University, British Columbia, Canada. Research interests include modeling and characterization of transport phenomena in microchannels and metalfoams, contacting surfaces and thermal interfaces, development of compact analytical and empirical models at micro and nano scales, and microelectronics cooling. He has numerous publications in refereed journals and conferences. He is a member of ASME, AIAA, and CSME.

Appendix F

Viscous flow in variable cross-section microchannels of arbitrary shapes

(with permission from Elsevier)

International Journal of Heat and Mass Transfer 54 (2011) 3970–3978

Contents lists available at ScienceDirect

International Journal of Heat and Mass Transfer

journal homepage: www.elsevier.com/locate/ijhmt

Viscous flow in variable cross-section microchannels of arbitrary shapes

M. Akbari [a,*], D. Sinton [b], M. Bahrami [a]

[a] Mechatronic Systems Engineering, School of Engineering Science, Simon Fraser University, Surrey, BC, Canada V3T 0A3
[b] Department of Mechanical Engineering, University of Victoria, Victoria,BC, Canada V8W 2Y2

ARTICLE INFO

Article history:
Received 9 October 2010
Received in revised form 11 April 2011
Available online 14 May 2011

Keywords:
Slowly-varying microchannels
Arbitrary cross-section
Pressure drop
Modeling
Characteristic length scale
Inertial effect
Frictional effect

ABSTRACT

This paper outlines a novel approximate model for determining the pressure drop of laminar, single-phase flow in slowly-varying microchannels of arbitrary cross-section based on the solution of a channel of elliptical cross-section. A new nondimensional parameter is introduced as a criterion to identify the significance of frictional and inertial effects. This criterion is a function of the Reynolds number and geometrical parameters of the cross-section; i.e., perimeter, area, cross-sectional polar moment of inertia, and channel length. It is shown that for the general case of arbitrary cross-section, the cross-sectional perimeter is a more suitable length scale. An experimental investigation is conducted to verify the present model; 5 sets of rectangular microchannels with converging–diverging linear wall profiles are fabricated and tested. The collected pressure drop data are shown to be in good agreement with the proposed model. Furthermore, the presented model is compared with the numerical and experimental data available in the literature for a hyperbolic contraction with rectangular cross-section.

1. Introduction

The concept of flow through microchannels with gradually varying walls forms the basis of a class of problems in microfluidics which has applications in micromixer design [1–5], accelerated particle electrophoresis [6,7], heat transfer augmentation in micro heat sinks [8–10], flow through porous media [11–15], blood flow in the context of biomechanics [16], preconcentration and separation of molecules [17–19], and polymer processing [20,21]. In most of these applications, it is required to obtain a reasonable estimate of the pressure drop in the channel for basic design and optimization. As a result, pressure drop in microconduits with variable cross-sections has been the subject of several investigations; examples are [2,16,22–29].

A simple model to approximate the flow in a variable cross-section microchannel is to assume that the fluid flow at each axial location x along the channel resembles the fully developed flow that would exist at that location if the channel shape did not vary with x; this is usually referred as the *lubrication approximation* [29,30]. The overall pressure drop is then calculated by integrating the local pressure gradient over the total length of the channel. Although good results can be obtained for creeping flow in mildly constricted channels, this method is not very accurate when the inertia effects become important or the amplitude of the constriction is substantial [26]. To obtain more accurate solutions, *asymptotic series solution* has been used by several authors for sinusoidal tubes [16,23–26] and two-dimensional channels with sinusoidal walls [22]. In this method, the solution of the Navier–Stokes equations is obtained by expanding the flow variables in powers of a small parameter characterizing the slowly varying character of the bounding walls, usually referred as *perturbation parameter*. Although the asymptotic solution method gives more accurate results compared to the lubrication approximation, the final solution for pressure drop and velocity field has a complex form even for simple cross-sectional geometries such as parallel plates or circular tubes.

Numerical and experimental methods are also used to investigate the laminar flow along slowly varying cross-section channels. Deiber and Schowalter [31] performed numerical study for the creeping flow through tubes with sinusoidal axial variations in diameter by using finite difference technique. The pressure drop results were then compared with those of measured through an independent experimentation. Hemmat and Borhan [32] used the boundary integral method to solve the Navier–stokes equations under the condition of creeping flow for axisymmetric capillary tubes whose diameter varies sinusoidally in the axial direction. Detailed velocity and pressure distributions within the capillary were obtained and the critical values of the geometrical parameters leading to flow reversal are reported.

As a result of recent advances in microfabrication techniques, microchannels with different cross-sectional geometries are fabricated for both commercial and scientific purposes. Finding analytical solutions for many practical cross-sections such as rectangle or trapezoid even for straight channels is complex and/or impossible.

* Corresponding author.
E-mail addresses: mohsen_akbari@sfu.ca, maa59@sfu.ca (M. Akbari).
URL: http://www.mohsenakbari.com (M. Akbari).

0017-9310/$ - see front matter © 2011 Elsevier Ltd. All rights reserved.
doi:10.1016/j.ijheatmasstransfer.2011.04.028

Nomenclature

a	major axis of ellipse/width of rectangle (m)	$Re_{\mathscr{L}}$	Reynolds number, $\rho U\mathscr{L}/\mu$ (–)
a_0	radius/width of the reference channel (m)	u	x-component of the velocity field (m/s)
A	local cross-sectional area (m^2)	U	local average velocity, Q/A (m/s)
A_0	cross-sectional area of the reference channel (m^2)	v	y-component of the velocity field (m/s)
b	minor axis of ellipse/height of rectangle (m)	w	z-component of the velocity field (m/s)
D_h	hydraulic diameter, $4A/\Gamma$ (m)		
f	fanning friction factor (–)	*Greek*	
I_p	polar momentum of inertia (m^4)	δ	maximum deviation from a_0 (m)
I_p^*	specific polar momentum of inertia, I_p/A^2 (–)	ϵ	aspect ratio, b/a (–)
L	channel length (m)	ε	perturbation parameter (–)
Q	volumetric flow rate (m^3/s)	Γ	local cross-sectional perimeter (m)
R	flow resistance, $\Delta p/Q$ (Pa s/m^3)	Γ_0	cross-sectional perimeter of the reference channel (m)
R_0	flow resistance of a reference straight channel, (Pa s/m^3)	$\mathscr{L}$	characteristic length scale (m)
R^*	dimensionless flow resistance, R/R_0 (–)	μ	viscosity (Pa s)
R_f^*	dimensionless frictional flow resistance (–)	ρ	density (kg/m^3)
R_i^*	dimensionless inertial flow resistance (–)	ξ	deviation parameter, δ/a_0 (–)

There are few works in the literature which are dealing with the hydrodynamics of laminar flow in slowly-varying channels of non-circular cross-section [2,27,28]. Lauga et al. [2] used the perturbation theory for creeping flow in channels constrained geometrically to remain between two parallel planes. Up to the first order accuracy of the perturbation solution, they showed that the velocity components perpendicular to the constraint plane cannot be zero unless the channel has both constant curvature and constant cross-sectional width. They only reported the zeroth order of the pressure gradient, which is identical to the lubrication approximation and only accounts for frictional effects. In another work, Gat et al. [28] studied the laminar incompressible gas flow through narrow channels with a variable cross-section using a higher order Hele–Shaw approximation [33]. Their method shows improvement over the classical Hele–Shaw solution [33], however, it does not account for the inertia effects that usually occurs in contractions or expansions. Wild et al. [27] used the perturbation theory to calculate the velocity and pressure distribution in an elliptical tube whose cross-sectional area varies slowly with a given profile along the axial direction. They [27] showed that the velocity distribution has a complicated form even up to the first order accuracy, but the local pressure gradient remains only a function of axial direction.

In the context of fluid flow in microchannels of arbitrary cross-section, few analytical studies have been performed for straight microchannels [34–36]. Yovanovich and Muzychka [34] showed that if the square root of cross-sectional area is used in the definition of the Poiseuille number, more consistent results can be obtained for various geometries. Zimmerman et al. [37] made an assessment of hydraulic radius, Saint–Venant, and Aissen's approximations to determine the hydraulic resistance of laminar fully developed flow in straight channels with irregular shapes. Comparing the proposed approximations with the available exact solutions, they showed that Saint–Venant, and Aissen's approximations are within 15% of the exact solution, whereas using the hydraulic radius can be in error by as much as 50%. Later, Bahrami et al. [35] introduced a general analytical model for the prediction of the Poiseuille number based on the square root of cross-sectional area in laminar fully developed flow along a straight microchannel of arbitrary cross-section. Using a "bottom-up" approach, they [35] showed that for constant fluid properties and flow rate in fixed cross-section channels, the Poiseuille number is only a function of geometrical parameters of the cross-section, i.e., cross-sectional perimeter, area, and polar moment of inertia. Their model was successfully validated against the numerical and experimental data for a wide variety of geometries including: hyperellipse, trapezoid, sine, square duct with two adjacent round corners, rhombic, circular sector, circular segment, annular sector, rectangular with semi-circular ends, and moon-shaped channels [35,38]. In a recent paper, Bahrami et al. [36] extended their general model to slip flow condition in a straight channel of arbitrary cross-section. Their model is shown to predict the numerical and experimental results obtained from the literature with good accuracy.

The purpose of this work is to develop an approximate method for the determination of the pressure drop of laminar, single-phase flow in slowly-varying microchannels of arbitrary cross-section by extending the previous models of Bahrami et al. [35] to slowly-varying microchannels of arbitrary cross-section. Starting from the solution of an elliptical cross-section [27], a generalized approximate model is proposed to compute the pressure drop in stream-wise periodic geometries, expansions and contractions. To verify the proposed model, an independent experimental investigation is carried out for stream-wise converging–diverging channels of rectangular cross-section with linear wall. Further validation is performed by comparing the results obtained from the present model and those obtained experimentally and numerically for a hyperbolic contraction of rectangular cross-section [21]. The proposed approach provides a powerful tool for basic designs, parametric studies, and the optimization analyses.

2. Model development

We seek a solution for steady-state laminar flow of a Newtonian fluid with constant properties in a slowly-varying conduit of arbitrary cross-section and wall profiles subjected to no-slip boundary condition on the walls. A schematic illustration of this channel is plotted in Fig. 1. Finding an exact analytical solution for such a problem is highly unlikely, but approximations can be obtained for a long channel in the form of a series in terms of a small perturbation parameter, ε. The idea is to take the advantage of the fact that variation in the direction of flow, x, is gradual compared to variation in the orthogonal directions; y and z. With ε is small, a regular perturbation expansion for both velocity and pressure fields can be written as [2]:

$$(u, v, w, p) = \sum_{n=0}^{\infty} \varepsilon^n (u_n, v_n, w_n, p_n), \tag{1}$$

where u, v, w are the velocity components and p is the pressure. The well-known perturbation approach [23–25] provides a method to

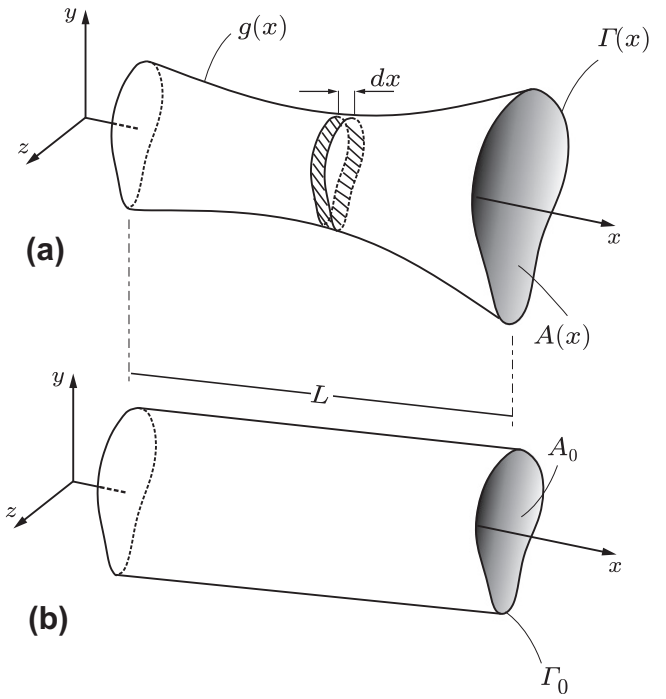

Fig. 1. (a) Schematic of a slowly-varying microchannel of arbitrary cross-section with a general wall profile of $g(x)$. (b) A reference straight channel with the cross-sectional area and perimeters of A_0 and Γ_0, respectively.

obtain the values of u_n, v_n, w_n and p_n by substituting Eq. (1) into the momentum and mass conservation equations. Finding u_n, v_n, w_n, and p_n, for the general case of three dimensional flows in arbitrary cross-section channels is impractical. Here, we use the perturbation solution of fluid flow in a slowly-varying tube of elliptical cross-section which is developed by Wild et al. [27] to propose a general model for arbitrary cross-section microchannels with a given wall profile. Elliptical cross-section is selected not because it is likely to occur in practice, but rather to utilize the unique geometrical property of its velocity solution.

Under the assumption of $\varepsilon^2 \ll 1$ where $\varepsilon = a_0/L$;a_0 is the hydraulic radius of a reference straight tube with the length of L, using the perturbation solution of Wild et al. [27], and after some rearrangements, the local pressure gradient for a slowly-varying conduit of elliptical cross-section can be obtained from the following relationship:

$$-\frac{1}{Q}\frac{dp}{dx} = \underbrace{\frac{4\mu[a^2(x)+b^2(x)]}{\pi a^3(x)b^3(x)}}_{\text{frictional}} - \underbrace{2\rho Q\left[\frac{dA(x)/dx}{A^3(x)}\right]}_{\text{inertial}}, \qquad (2)$$

$$A(x) = \pi a(x)b(x),$$

where $a(x)$ and $b(x)$ are the channel local half-major and half-minor axes, respectively; Q is the volumetric flow rate; $A(x)$ is the local cross-sectional area; $\mu$is the fluid viscosity; and $\rho$is the fluid density. For simplicity, we drop all (x) after this point. Noting Eq. (2), the followings can be concluded:

- The pressure gradient at each axial location can be obtained from the superposition of the frictional and the inertia terms.
- The frictional term in Eq. (2) resembles the laminar fully-developed flow in a straight channel of elliptical cross-section [39] and is a function of the major and minor axes of the ellipse. This is analogous to the lubrication approximation. One can follow the same steps introduced by Bahrami et al. [35] to obtain the local pressure gradient for slowly-varying microchannels of arbitrary cross-section.
- The inertia term only depends on dA/dx and the cross-sectional area but not the cross-sectional shape of the channel. In a converging channel, $dA/dx < 0$, the inertia term takes a positive value while for a diverging channel, $dA/dx > 0$, the inertia term is negative.
- The inertia term will vanish for any periodic profile, $dA(x)/dx = 0$. This is because the higher orders of the perturbation expansion are neglected, i.e., $\varepsilon^2 \ll 1$. It has been shown for simple geometries that the inertial pressure drop in a periodic channel will be non-negligible for sufficiently high Reynolds numbers or when the higher order terms in the perturbation expansion, i.e., Eq. (1), becomes significant [26,37].

Using Eq. (2), the local Poiseuille number based on an arbitrary length scale of $\mathscr{L}$ for slowly-varying microchannels of elliptical cross-section, $fRe_{\mathscr{L}}$, takes the following form:

$$fRe_{\mathscr{L}} = \left(\frac{\mathscr{L}}{\Gamma}\right)\left\{\underbrace{32\pi^2 I_p^*}_{\text{frictional}} - \underbrace{\frac{4\rho Q}{\mu}\left(\frac{dA/dx}{A}\right)}_{\text{inertial}}\right\}, \qquad (3)$$

where

$$fRe_{\mathscr{L}} = \frac{2}{\mu}\frac{(-dp/dx)}{Q}\left(\frac{\mathscr{L}}{\Gamma}\right)A^2, \qquad (4)$$

and

$$f = \frac{(-dp/dx)}{Q}\left(\frac{1}{1/2\rho U}\right)\left(\frac{A^2}{\Gamma}\right), \qquad (5)$$

$$Re_{\mathscr{L}} = \frac{\rho U \mathscr{L}}{\mu}, \qquad (6)$$

where U is the local average velocity, Γ is the local cross-sectional perimeter, and $I_p^* = I_p/A^2$ with $I_p = \int_A (y^2+z^2)dA$ is called the *specific polar moment of cross-sectional inertia* [35] and can be obtained from the following relationship for an elliptical cross-section:

$$I_p^* = \frac{1+\epsilon^2}{4\pi\epsilon}, \qquad (7)$$

where $0 < \epsilon \equiv b/a \leqslant 1$ is the aspect ratio of the channel cross-section such that the $\epsilon = 1$ leads to the circular cross-section. For other cross-sectional geometries such as rectangular, rhombic, trapezoidal, moon-shaped, triangular, circular segment, and annular sector, a comprehensive list of relationships can be found in Refs.[35,40].

Consistent with the model developed by Bahrami et al. [35] for straight microchannels of arbitrary cross-section, the present approximate model postulates that for constant fluid properties and flow rate in a variable cross-section channel, the local $fRe_{\mathscr{L}}$ for an arbitrary cross-section channel is only a function of the local specific polar momentum of cross-sectional area, I_p^*, $\mathscr{L}/\Gamma$ and the ratio of $(A^{-1}dA/dx)$.

Selection of the characteristic length scale is an arbitrary choice and will not affect the final solution. However, a more appropriate length scale leads to more consistent and similar results, especially when general cross sections are considered. For instance, a circular duct is fully described by its diameter; thus the obvious length scale is the diameter (or radius). For non-circular cross sections, the selection is not as clear. Possible length scales are: (i) the hydraulic diameter $D_h = 4A/\Gamma$, which has been conventionally used in many textbooks [39], (ii) effective radius defined as the average between the radius of largest inscribed circle and the radius of the circle with same area [41], (iii) the square root of the cross-sectional area,$\sqrt{A}$, which has been widely used for non-circular heat

conduction and convection problems [35,36,42,43], and (iv) the perimeter of the cross-section, Γ.

Fig. 2 shows the comparison of the frictional Poiseuille number for elliptical and rectangular cross-sections based on the hydraulic diameter, D_h, perimeter, Γ, and the square root of cross-sectional area, $\sqrt{A}$. It can be observed that the hydraulic diameter does not lead to a consistent trend for rectangular and elliptical cross-sections; the maximum difference is 30%. However, using either perimeter or the square root of cross-sectional area as the characteristic length scale leads to similar trends for the frictional Poiseuille number with the relative difference of less than 4% and 8%, respectively. Similar to the frictional Poiseuille number, the hydraulic diameter leads to a large relative differences between the inertial Poiseuille numbers of elliptical and rectangular cross-sections; the maximum relative difference is 24%. The square root of cross-sectional area leads to the relative difference of less than 11% between the inertial Poiseuille numbers of elliptical and rectangular cross-sections. However, when the cross-sectional perimeter is used as a characteristic length scale, Eq. (3) clearly shows that for constant fluid properties, flow rate, and geometrical parameters, there is no relative difference between the inertial Poiseuille numbers of the elliptical and rectangular cross-sections. These results suggest that using the cross-sectional perimeter as the characteristic length scale for overall Poiseuille number leads to better accuracies. Therefore, we use $\mathscr{L} = \Gamma$ through all our calculations. As a result, Eq. (3) reduces to:

$$fRe_\Gamma = 32\pi^2 I_p^* - \frac{4\rho Q}{\mu}\left(\frac{dA/dx}{A}\right). \tag{8}$$

It should be noted that one can convert the Poiseuille number based on different length scales using the following relationships:

$$\begin{aligned} fRe_{\sqrt{A}} &= \left(\frac{\sqrt{A}}{\Gamma}\right) fRe_\Gamma, \\ fRe_{D_h} &= \left(\frac{4A}{\Gamma^2}\right) fRe_\Gamma. \end{aligned} \tag{9}$$

For many applications, it is desired to calculate the total flow resistance of the channel. Using Eqs. (4) and (8) and integrating over the length of the channel, the total flow resistance of a slowly-varying microchannel of arbitrary cross-section, shown in Fig. 1, can be obtained from the following relationship:

$$R = \Delta p/Q = 16\pi^2\mu \int_{x_1}^{x_2} \frac{I_p^*}{A^2}dx + \rho Q\left(\frac{1}{A_2^2} - \frac{1}{A_1^2}\right), \tag{10}$$

where A_2^2 and A_1^2 are the microchannel cross-sectional area at x_1 and x_2 locations, respectively. It is beneficial to normalize the flow

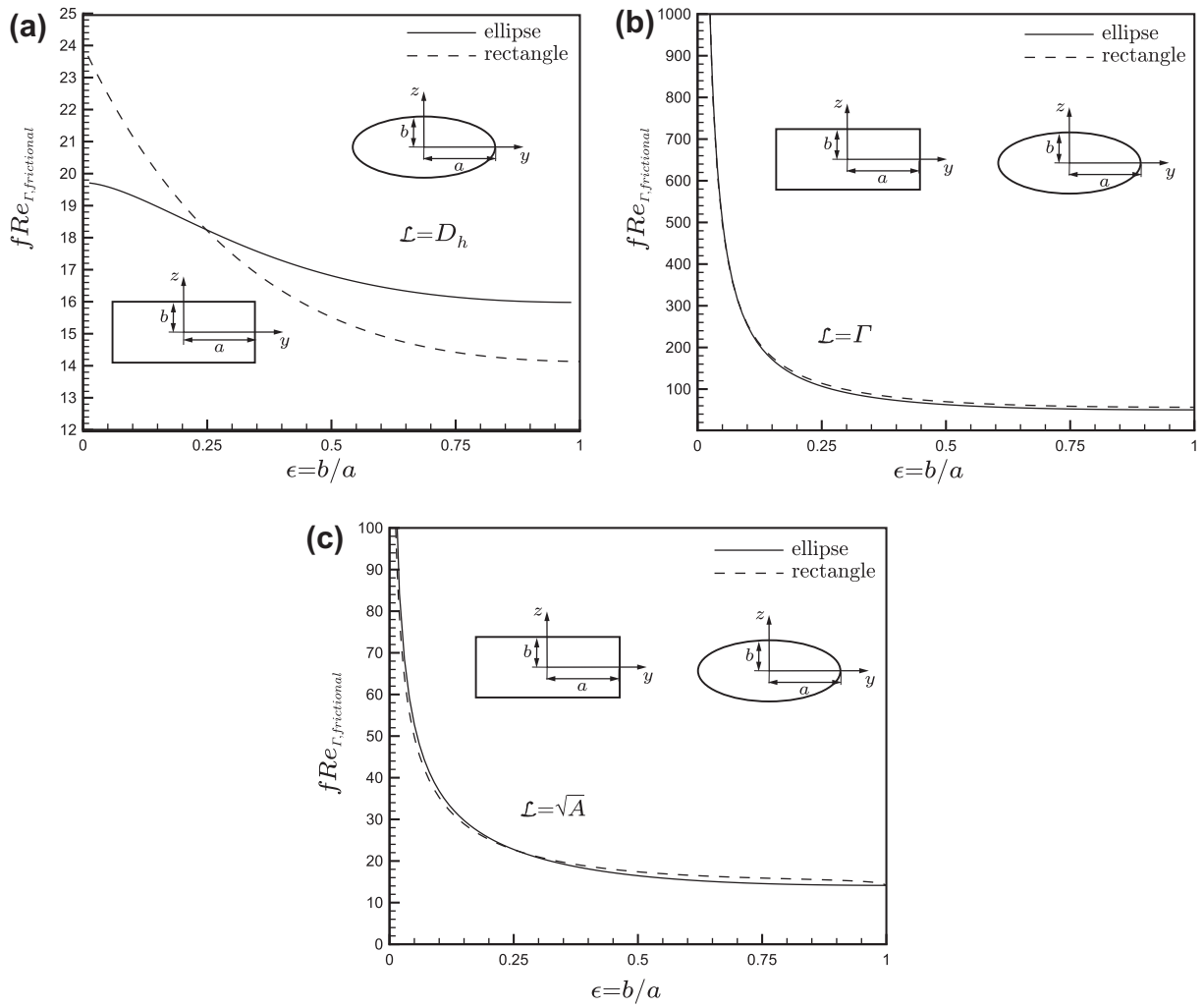

Fig. 2. Effect of the selection of (a) hydraulic diameter, D_h, (b) perimeter, Γ, and (c) square root of area, $\sqrt{A}$ as characteristic length scale on the relative difference between the frictional Poiseuille numbers of rectangular and elliptical cross-sections. The maximum differences are 30%, 8%, and 4%, for the hydraulic diameter, the square root of cross-sectional area, and the perimeter of cross-sectional area, respectively.

resistance with that of a straight reference channel with the specific polar momentum of inertia of $I^*_{p,0}$, length of L, and cross-sectional area of A_0. Thus:

$$R^* = R/R_0 = \underbrace{\int_{x_1^*}^{x_2^*} \frac{I_p^*/I_{p,0}^*}{A^{*2}} dx^*}_{R_f^*} + \underbrace{\frac{Re_{\Gamma_0}}{16\pi^2 I_{p,0}^*}\left(\frac{A_0/\Gamma_0}{L}\right)\left(\frac{1}{A_2^{*2}} - \frac{1}{A_1^{*2}}\right)}_{R_i^*}, \quad (11)$$

where $x^* = x/L, A_1^* = A_1/A_0$ and $A_2^* = A_2/A_0$. In Eq. (11), Γ_0 is the perimeter of the reference channel cross-section; $Re_{\Gamma_0} = \rho Q \Gamma_0/\mu A_0$; and R_0^* can be computed from the following relationship [35]:

$$R_0 = 16\pi^2 \mu \frac{I_{p,0}^*}{A_0^2} L. \quad (12)$$

Eq. (11) is a general relationship that accounts for both frictional and inertial effects on the flow resistance of fluid flow in slowly-varying microchannels of arbitrary cross-section. Dividing both sides of Eq. (11) by the frictional flow resistance, R_f^*, one obtains:

$$\frac{R^*}{R_f^*} = 1 + \frac{R_i^*}{R_f^*}. \quad (13)$$

Eq. (13) can be rearranged as follows:

$$\frac{R^*}{R_f^*} = 1 + \Phi Re_{\Gamma_0}. \quad (14)$$

The dimensionless parameter Φ appears in Eq. (14) is purely geometrical and defined as follows:

$$\phi = \frac{\left(\frac{1}{A_1^{*2}} - \frac{1}{A_2^{*2}}\right)}{16\pi^2 \int_{x_1}^{x_2} \frac{I_p^*}{A^{*2}} dx^*}\left(\frac{A_0/\Gamma}{L}\right) \quad (15)$$

Eq. (14) implies that the inertia term in a slowly-varying microchannel can be neglected under the following condition:

$$\Phi Re_{\Gamma_0} \ll 1. \quad (16)$$

3. Experimental procedure

3.1. Chemicals and materials

Distilled water was used as the testing liquid. SU-8 photoresist (Microchem, Newton, MA) and diacetone–alcohol developer solution (Sigma–Aldrich, St. Louis, MO) were used in the making of the positive relief masters by the procedure outlined below. Polydimethylsiloxane (PDMS) casts were prepared by thoroughly mixing the base and curing agent at a 10:1 ratio as per the manufacturer's instructions for the Sylgard 184 silicon elastomer kit (Dow Corning, Midland, MI).

3.2. Microfabrication

The PDMS/PDMS converging–diverging and reference straight microchannels were manufactured using the soft lithography technique [44]. Briefly, photomasks were designed by AutoCAD software (www.usa.autodesk.com) and printed with a 3500DPI printer (Island graphics Ltd., Victoria, BC). Masters containing the desired microchannel pattern have been made by spin coating of SU-8 negative photoresist on a glass slide to the desired nominal thickness. Both converging–diverging and reference channels were fabricated on the same master. Prior to the spin coating of SU-8, the glass slide was cleaned with isopropyl alcohol (IPA) and dried by high pressure air. The photoresist film was then hardened through a two-stage direct contact pre-exposure bake procedure (65 °C for 5 min and 95 °C for 30 min) and exposed to UV light for 100 s through the mask containing the channel pattern. A two stage post-exposure bake procedure (65 °C for 5 min, 95 °C for 30 min) was then used to enhance cross-linking in the exposed portion of the film. The slide was then placed in quiescent developer solution for 10 min to dissolve the unexposed photoresist, leaving a positive relief containing the microchannel pattern. Liquid PDMS was then poured over the master and exposed to vacuum condition (1 h) to extract all the bubbles in it and cured at 85 °C for 15 – 20 min yielding a negative cast of the microchannel pattern. An enclosed microchannel was then formed by bonding the PDMS cast with another piece of PDMS via plasma treatment. Each variable cross-section microchannel contained ten converging–diverging modules with linearly varying wall with the module length of 3 mm ± 0.02 mm.

Dimensions of the channel were measured by an image processing method described in [38]. Briefly, an inverted microscope (Unitron, Commack, NY) equipped with 5 X, 0.12 N.A. and 10 X, 0.4 N.A. objectives and a CCD camera was used. The low magnification objective was used to measure the length of each module. Images of the channels were taken at three different locations and then imported into an image processing software (Zarbco video toolbox, Ver. 1.65), which was calibrated with an optical ruler (Edmund optics, Barrington, NJ), to measure the in-plane geometrical parameters. For each microchannel, average values are reported. To determine the channel depth, the pressure drop along each straight reference channel was measured using the method described later and Eq. (12) with constant geometrical parameters was used to compute the channel depth. The geometrical parameters are reported in Table (1).

3.3. Experimental procedure

Schematic diagram of the experimental setup is depicted in Fig. 3. Controlled measurements of the flow resistance for flow through a microchannel were performed using a syringe pump (Harvard Apparatus, Quebec, Canada) with Hamilton Gastight glass syringes, which provides a constant flow rate with the accuracy of ±0.5%. A range of Reynolds number from $Re_{\Gamma_0} = 10 - 75$ (corresponding Reynolds number based on the hydraulic diameter falls in the range of 2 – 15) was covered by changing the volumetric flow rate from 30 L/min to 100 μL/min.The accuracy of the nominal flow rate was independently evaluated by weighting the collected water over the elapsed time. It was observed that the relative difference between the measured and nominal flow rate was less than 4% in our experiments. This value is taken as the uncertainty in the flow rate readings. The pressure drop along the flow channel was measured using a gauge pressure transducer (Omega Inc., Laval) with the accuracy of ±0.004 psi (±30 Pa) and a nominal pressure range of 0 – 5 psi. This pressure sensor was connected to the entrance of the microchannel using a 1 cm-long piece of plastic tubing with an inner diameter of 3 mm. From the exit of the microchannel, 2 cm of the same kind of plastic tubing released the fluid into a waste container at atmospheric pressure. The contribution of the connecting tube is calculated to be less than 0.01% of the total measured pressure drop. Measured pressure was monitored and recorded with a computerized data acquisition system (Labview 8.5, National Instrument, www.ni.com). The flow was considered to have reached a steady state condition when the readings of the pressure drop did not change with time. Due to the fluctuations of the volumetric flow rate provided by the syringe pump and formation of the droplets at the tube exit, periodic pressure fluctuations were observed in the pressure vs. time graph, even for the steady-state condition. Average values of these fluctuations are considered in this experiment. For a given channel, the measurement of pressure drop was repeated three times for each

Table 1
Experimental parameters in present work.

Channel #	$2a_0$ (μm)	$2b$ (μm)	$D_{h,0}$ (μm)	Γ_0 (μm)	L (mm)	$\epsilon_0 = b/a_0$	$\xi = \delta/a_0$
1	311	78	125	780	3	0.25	0.27
2	286	93	140	760	3	0.32	0.42
3	283	62	103	691	3	0.22	0.53
4	389	36	66	850	3	0.09	0.09
5	286	63	104	700	3	0.22	0.42

$Q = 30 - 100$ μL/min; $\Delta p = 0.86 - 24.13$ kPa.

flow rate to ensure the reproducibility of the results. An arithmetic averaging method [45] was performed to determine the final results. The maximum difference between the averaged and the actual values was observed to be less than 1.5%. In this experiment the effects of the developing length, minor losses, viscous heating and channel deformation were neglected [38]. The experimental values of R_f^* were computed from the following relationship:

$$R^*_{\text{exp}} = \frac{(\Delta p/Q)}{(\Delta p/Q)_0}, \tag{17}$$

where the parameters with "0" subscript correspond to the measured flow resistance of the reference straight channel. The uncertainty associated with the measured R^*_{exp} is calculated from the following relationship [45]:

$$\frac{\psi_{R^*}}{R^*} = \left[\left(\frac{\psi_{\Delta p}}{\Delta p}\right)^2 + \left(\frac{\psi_Q}{Q}\right)^2\right]^{1/2}, \tag{18}$$

where ψ_{R^*}/R^* is the relative uncertainty of the dimensionless flow resistance, $\psi_{\Delta p}$ is the uncertainty associated with the pressure measurement is ±0.25% of the full scale, i.e., ±30 Pa, and ψ_Q is the uncertainty associated with the flow rate provided by the syringe pump with $\psi_Q/Q = \pm 0.04$. The calculated uncertainties are reported as error bars in the experimental results.

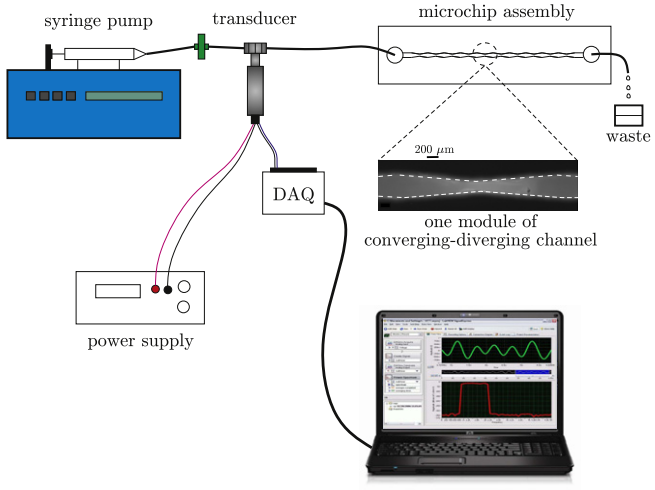

Fig. 3. Schematic diagram of the experimental setup for pressure measurements in converging–diverging channels. The inert in the module of converging–diverging channel is Rhodamine B, for clarity.

4. Results and discussion

In this section, the present model is compared against the experimental data obtained in this work for stream-wise periodic channels of rectangular cross-section and numerical and experimental data collected from the work of Oliveira et al. [21] for a hyperbolic contraction.

The converging–diverging channels were fabricated with a linear wall profile defined as follows, see Fig. 4(a):

$$a^* = a(x^*)/a_0 = \begin{cases} [1 - \xi(4x^* + 1)], & -1/2 \leqslant x^* \leqslant 0, \\ [1 + \xi(4x^* - 1)], & 0 \leqslant x \leqslant 1/2, \end{cases} \tag{19}$$

where the origin is located at the channel throat, a^* is the channel with normalized with respect to the staight reference channel with the with of a_0; $x^* = x/L$ is the normalized coordinate in the axial dimention with respect to the module lenght of L; $\xi = \delta/a_0$is the *deviation parameter* which shows the amount of deviation from a straight channel with the average width of a_0. For such a geometry, the inertia term in Eq. (11) is eliminated because $A_2^* = A_1^*$. Specific polar moment of inertia for a rectangular cross-section microchannel can be obtained from Ref. [40]; thus one can calculate the ratio of $I_p^*/I_{p,0}^*$ as follows:

$$I_p^*/I_{p,0}^* = \frac{a^* + \epsilon_0^2}{a^*(1 + \epsilon_0^2)}, \tag{20}$$

where similar to an elliptical cross-section channell, $\epsilon = b/a$, is the local channel aspect ratio, $\epsilon_0 = b/a_0$ is the aspect ratio of the straight reference channel, and a. Dimensionless cross-sectional area for a rectangular cross-section can be obtained from the following relationship:

$$A^* = a^*, \tag{21}$$

where the ratio of a/a_0 can be obtained from Eq. (19). Substituting Eqs. (21) and (20) into Eq. (11) gives:

$$R^* = \int_{-1/2}^{1/2} \frac{a^* + \epsilon_0^2}{1 + \epsilon_0^2} dx^*, \tag{22}$$

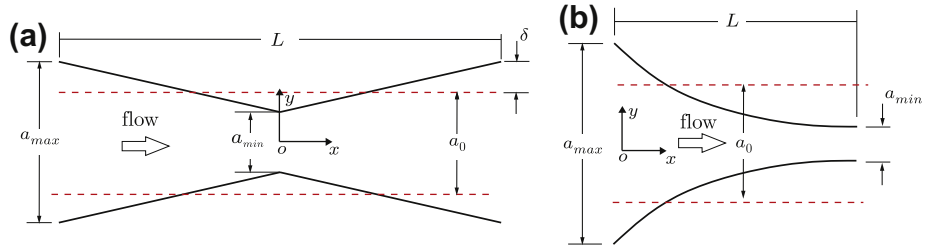

Fig. 4. Schematic of the studied wall geometries: (a) stream-wise periodic wall with linear profile and (b) hyperbolic contraction.

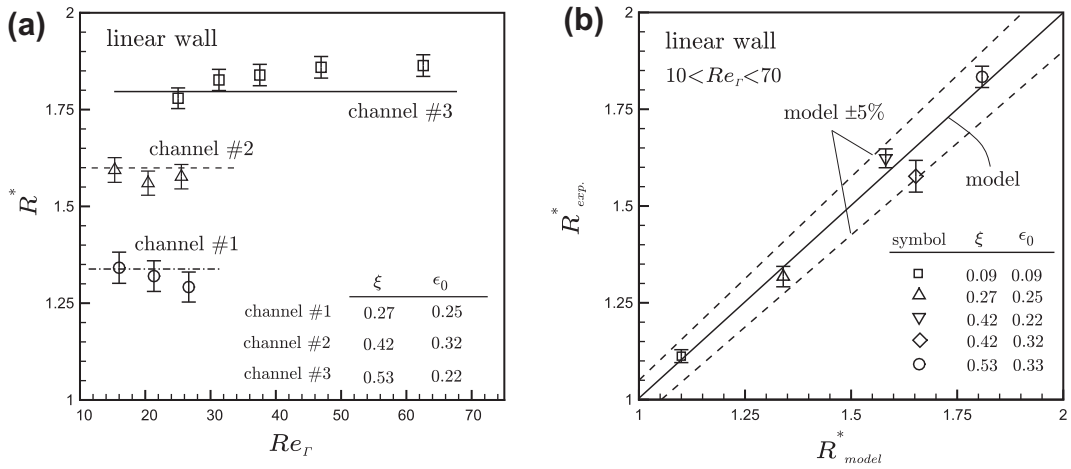

Fig. 5. Experimental data for stream-wise periodic geometry with linear wall: (a) variation of the data with respect to the Reynolds number, the symbols are the experimental data and the lines represent the values predicted by Eq. (23); (b) experimental data vs. proposed model. Each symbol corresponds to one channel, the solid line shows the proposed model and the dashed lines are model ±5%. Note that the range of Reynolds number based on the hydraulic diameter is less than 15.

Integrating Eq. (22) and after some simplifications, the dimensionless flow resistance of a rectangular microchannel cross-section with a linear wall profile can be obtained from the following relationship:

$$R^* = \frac{2\xi\epsilon_0^2 + (1-\xi^2)^2 \ln\left(\frac{1+\xi}{1-\xi}\right)}{2\xi(1-\xi^2)^2(1+\epsilon_0^2)}. \tag{23}$$

Fig. 5(a) shows the variation of experimental data for R_f^* with Reynolds number. For clarity, the results are only plotted for three samples. The geometrical parameters for each channel are shown in the plot. In agreement with the proposed theory, the trend of data shows that R_f^* is an independent function of the Reynolds number. Thus for each microchannel, the average value of R^* over the Reynolds number is taken and plotted against the values obtained from the compact relationship of Eq. (23) in Fig. 5(b). Good agreement between the model and experimental results can be observed.

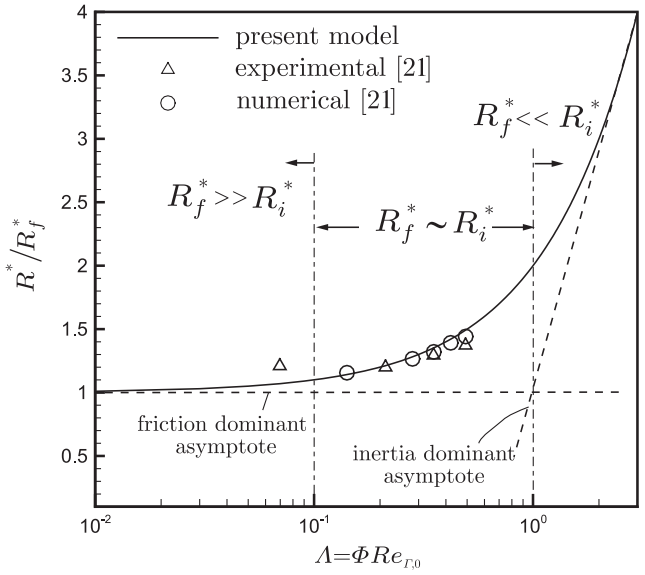

Fig. 6. Comparison of the theoretical model to experimental and numerical results from Oliveira et al. [21]. The solid line corresponds to the proposed model, Eq. (25) which includes both frictional and inertia terms, and delta (△) and circular (○) symbols are the experimental and numerical data, respectively. Two asymptotes of friction dominant and inertia dominant regions are shown in the plot by dashed lines.

A hyperbolic contraction as shown in Fig. 4(b) is defined as follows:

$$a^* = a(x^*)/a_{\max} = \frac{1}{1+(\beta-1)x^*}, \tag{24}$$

where a^* is the channel with normalized with respect to the maximum width of $a_{\max}$; $\beta = a_{\max}/a_{\min}$; $a_{\min}$ is the minimum width of the channel; and L is the channel length. For such a geometry, both frictional and inertia terms exist. Following the same steps explained for the linearly varying wall microchannel the total dimensionless flow resistance can be obtained from the following compact relationship:

$$R^* = \frac{\left[2(\beta-1)^2 + (\beta^2+1)(\epsilon_0 \ln\beta)^2\right](\beta+1)\ln\beta}{4(\beta-1)^2(1+\epsilon_0^2)} + \frac{3(\beta+1)(\ln\beta)^2\epsilon_0\sqrt{\epsilon_0}}{16\pi^2(\beta-1)(1+\epsilon_0^2)(1+\epsilon_0)^2} Re_{\Gamma_0}\varepsilon. \tag{25}$$

Fig. 6 shows the comparison between the experimental and numerical data obtained by Oliveira et al. [21] for a hyperbolic contraction defined by Eq. (24) with rectangular cross-section and the proposed model, Eq. (14). The geometrical and flow conditions used by Oliveira et al. [21] are listed in Table (2). The present model illustrates good agreement with the data; the relative difference between the data and the compact relationship of Eq. (25) is less than 8%. Three regions can be identified in Fig. 6 based on the value dimensionless parameter $\Lambda = \Phi Re_{\Gamma_0}$:

(i) Friction dominated, $\Lambda \ll 1$, the flow is purely frictional and the lubrication theory gives accurate prediction of the pressure drop.
(ii) Transitional, $\Lambda \sim O(1)$, both frictional and inertial effects should be taken into account.
(iii) Inertia dominated, $\Lambda \gg 1$, the inertial effect is dominant, thus the effect of wall profile becomes negligible and the flow resistance can be obtained by computing the cross-section geometrical parameters for the reference channel,

Table 2
Geometrical and flow conditions used for the hyperbolic contraction.

Parameter	$a_{\max}$ (μm)	$a_{\min}$ (μm)	b (μm)	Γ_0 (μm)	L (μm)	ϵ_0	β	$Re_{\Gamma,0}$
Value	400	19.9	46	217	382	0.7	20.1	20–160

inlet and outlet cross-sectional area, and the Reynolds number, see Eq. (11).

As an example, the data obtained from [21] fall in the transitional region which means that considering the lubrication approximation will lead to an underprediction of the pressure drop. One should note that for a stream-wise periodic geometry, the inlet and outlet cross-sectional areas for one module are the same, thus $\Lambda = 0$ and the inertial effect through the entire module of a converging–diverging channel becomes negligible.

5. Summary and conclusions

The pressure drop of single phase flow in slowly-varying microchannels of arbitrary cross-section has been investigated in this study. Starting from the available perturbation solution of an elliptical cross-section and assuming that the second and higher order perturbation terms are negligible, a general approximate model has been developed. The proposed model presents improved accuracy over the lubrication approximation by taking the inertial effect into account. An independent experimental study has been conducted for microchannels with stream-wise periodic geometry and rectangular cross-section. Experimental results have been used to verify the proposed model. Further validation is performed by comparing the model with the numerical and experimental data collected from the literature for a hyperbolic contraction. The highlights of this study are as follows:

- Selection of the characteristic length scale does not affect the flow regime or pressure drop. Using the cross-sectional perimeter or square root of area as a characteristic length scale in the definition of the Poiseuille number leads to a more consistent trend between different cross-sections. Since the cross-sectional perimeter gives better accuracy, it has been used as the characteristic length scale through our analysis.
- For a slowly-varying microchannel of arbitrary cross-section, the Poiseuille number of laminar flow of a fluid with constant properties can be obtained from the superposition of frictional and inertial terms. A dimensionless parameter is introduced to determine the importance of each term.
- Comparison with experimental and numerical results shows good agreement between the proposed model and the collected data. It has been observed that for a hyperbolic contraction, using the lubrication approximation underestimates the pressure drop. However, taking the inertia term into account by the proposed model gives excellent improvement over the lubrication approximation.

Acknowledgments

The authors gratefully acknowledge the financial support of the Natural Sciences and Engineering Research Council of Canada (NSERC), BC Innovation Council (BCIC), Canada Research Chair Program, and K. Wong's assistance in experimental setup design and pressure measurements.

References

[1] A. Stroock, S. Dertinger, A. Ajdari, I. Mezic, H. Stone, G. Whitesides, Chaotic mixer for microchannels, Science 295 (5) (2002) 647–651.
[2] E. Lauga, A. Stroock, H. Stone, Three-dimensional flows in slowly varying planar geometries, Phys. Fluids 16 (2004) 3051–3063.
[3] S. Hsieh, Y. Huang, Passive mixing in micro-channels with geometric variations through μPIV and μLIF measurements, J. Micromech. Microeng. 18 (2008) 065017.
[4] R. Liu, K. Sharp, M. Olsen, M. Stremler, J. Santiago, R. Adrian, H. Aref, D. Beebe, A passive three-dimensional C-shapehelical micromixer, J. Microelectromech. Syst. 9 (2) (2000) 190–198.
[5] A. Bertsch, S. Heimgartner, P. Cousseau, P. Renaud, Static micromixers based on large-scale industrial mixer geometry, Lab Chip 1 (1) (2001) 56–60.
[6] X. Xuan, B. Xu, D. Li, Accelerated particle electrophoretic motion and separation in converging–diverging microchannels, Anal. Chem. 77 (14) (2005) 4323–4328.
[7] X. Xuan, D. Li, Particle motions in low-Reynolds number pressure-driven flows through converging–diverging microchannels, J. Micromech. Microeng. 16 (2006) 62–69.
[8] E. Sparrow, A. Prata, Numerical solutions for laminar flow and heat transfer in a periodically converging–diverging tube, with experimental confirmation, Numer. Heat Transfer A. Appl. 6 (4) (1983) 441–461.
[9] G. Wang, S. Vanka, Convective heat transfer in periodic wavy passages, Int. J. Heat Mass Transfer 38 (17) (1995) 3219–3230.
[10] T. Nishimura, Y. Bian, Y. Matsumoto, K. Kunitsugu, Fluid flow and mass transfer characteristics in a sinusoidal wavy-walled tube at moderate Reynolds numbers for steady flow, Heat Mass Transfer 39 (3) (2003) 239–248.
[11] A. Lahbabi, H. Chang, Flow in periodically constricted tubes: transition to inertial and nonsteady flows, Chem. Eng. Sci. 41 (10) (1986) 2487–2505.
[12] A. Payatakes, C. Tien, R. Turian, A new model for granular porous media: part I. Model formulation, AIChE J. 19 (1) (1973) 58–67.
[13] Y. Bernabé, J. Olson, The hydraulic conductance of a capillary with a sinusoidally varying cross-section, Geophys. Res. Lett. 27 (2) (2000) 245–248.
[14] A. Tamayol, M. Bahrami, Analytical determination of viscous permeability of fibrous porous media, Int. J. Heat Mass Transfer 52 (9–10) (2009) 2407–2414.
[15] A. Tamayol, M. Bahrami, In-plane gas permeability of proton exchange membrane fuel cell gas diffusion layers, J. Power Sources 196 (2010) 3559–3564.
[16] J. Forrester, D. Young, Flow through a converging–diverging tube and its implications in occlusive vascular disease–II: theoretical and experimental results and their implications, J. Biomech. 3 (3) (1970) 307–310.
[17] D. Ross, L. Locascio, Microfluidic temperature gradient focusing, Anal. Chem. 74 (11) (2002) 2556–2564.
[18] G. Sommer, Electrokinetic Gradient-Based Focusing Mechanisms for Rapid, On-Chip Concentration and Separation of Proteins, University of Michigan, 2008.
[19] S. Kim, G. Sommer, M. Burns, E. Hasselbrink, Low-power concentration and separation using temperature gradient focusing via Joule heating, Anal. Chem. 78 (23) (2006) 8028–8035.
[20] D. James, G. Chandler, S. Armour, A converging channel rheometer for the measurement of extensional viscosity, J. Non-Newton. Fluid Mech. 35 (2–3) (1990) 421–443.
[21] M. Oliveira, M. Alves, F. Pinho, G. McKinley, Viscous flow through microfabricated hyperbolic contractions, Exp. Fluids 43 (2) (2007) 437–451.
[22] P. Kitanidis, B. Dykaar, Stokes flow in a slowly varying two-dimensional periodic pore, Transport Porous Med. 26 (1) (1997) 89–98.
[23] M. Manton, Low Reynolds number flow in slowly varying axisymmetric tubes, J. Fluid Mech. 49 (3) (2006) 451–459.
[24] J. Chow, K. Soda, Laminar flow in tubes with constriction, Phys. Fluids 15 (1972) 1700–1717.
[25] M. Van Dyke, Slow variations in continuum mechanics, Adv. Appl. Mech. 25 (1987) 1–45.
[26] S. Sisavath, X. Jing, R. Zimmerman, Creeping flow through a pipe of varying radius, Phys. Fluids 13 (2001) 2762–2772.
[27] R. Wild, T. Pedley, D. Riley, Viscous flow in collapsible tubes of slowly varying elliptical cross-section, J. Fluid Mech. 81 (2) (1977) 273–294.
[28] A. Gat, I. Frankel, D. Weihs, A higher-order Hele–Shaw approximation with application to gas flows through shallow micro-channels, J. Fluid Mech. 638 (2009) 141–160.
[29] M. Akbari, D. Sinton, M. Bahrami, Laminar fully developed flow in periodically converging–diverging microtubes, Heat Transfer Eng. 31 (8) (2010) 628–634.
[30] S. Sisavath, A. Al-Yaaruby, C. Pain, R. Zimmerman, A simple model for deviations from the cubic law for a fracture undergoing dilation or closure, Pure Appl. Geophys. 160 (5) (2003) 1009–1022.
[31] J. Deiber, W. Schowalter, Flow through tubes with sinusoidal axial variations in diameter, AIChE J. 25 (4) (1979) 638–645.
[32] M. Hemmat, A. Borhan, Creeping flow through sinusoidally constricted capillaries, Phys. Fluids 7 (1995) 2111.
[33] G. Batchelor, An Introduction to Fluid Dynamics, Cambridge University Press, 2000.
[34] M. Yovanovich, Y. Muzychka, Solutions of Poisson equation within singly and doubly connected prismatic domains, in: 1997 National Heat Transfer Conference, Baltimore, MD, 1997.
[35] M. Bahrami, M. Michael Yovanovich, J. Richard Culham, A novel solution for pressure drop in singly connected microchannels of arbitrary cross-section, Int. J. Heat Mass Transfer 50 (13–14) (2007) 2492–2502.
[36] M. Bahrami, A. Tamayol, P. Taheri, Slip-flow pressure drop in microchannels of general cross section, J. Fluids Eng. 131 (2009) 031201–031208.
[37] R. Zimmerman, A. Al-Yaarubi, C. Pain, C. Grattoni, Non-linear regimes of fluid flow in rock fractures, Int. J. Rock Mech. Min. Sci. 41 (3) (2004) 384.
[38] M. Akbari, D. Sinton, M. Bahrami, Pressure drop in rectangular microchannels as compared with theory based on arbitrary cross section, ASME J. Fluids Eng. 131 (2009) 041202-1–041202-8.
[39] F. White, Viscous Flow, McGraw-Hill Inc, 1991.

[40] M. Bahrami, M. Yovanovich, J. Culham, et al., Pressure drop of fully-developed, laminar flow in microchannels of arbitrary cross-section, J. Fluids Eng. 128 (2006) 1036–1044.
[41] S. Bryant, P. King, D. Mellor, Network model evaluation of permeability and spatial correlation in a real random sphere packing, Transport Porous Med. 11 (1) (1993) 53–70.
[42] M. Yovanovich, A general expression for predicting conduction shape factors, AIAA Prog, in Astro, and Aeronautics: Thermophysics and Spacecraft Thermal Control, vol. 35, 1974, pp. 265–291.
[43] Y. Muzychka, M. Yovanovich, Laminar flow friction and heat transfer in non-circular ducts and channels: part I – hydrodynamic problem, in: Proceedings of Compact Heat Exchangers, A Festschrift on the 60th Birthday of Ramesh K. Shah, Grenoble, France, 2002, pp. 123–130.
[44] J. McDonald, D. Duffy, J. Anderson, D. Chiu, H. Wu, O. Schueller, G. Whitesides, Fabrication of microfluidic systems in poly (dimethylsiloxane), Electrophoresis 21 (1) (2000) 27–40.
[45] J. Holman, W. Gajda, Experimental Methods for Engineers, McGraw-Hill, New York, 1994.

Appendix G

Uncertainty analysis

Suppose a set of measurements is made and the result, R, is a given function of independent variables x_1, x_2, x_3, ..., x_n. Thus,

$$R = R(x_1, x_2, x_3, ..., x_n) \tag{G.1}$$

To calculate the uncertainty associated with the experimental measurements, ω_R, the following relationship can be used [1]

$$\omega_R = \left[\sum \left(\frac{\partial R}{\partial x_i} \omega_n \right)^2 \right]^{1/2} \tag{G.2}$$

where ω_i is the uncertainty of the independent variable of x_i. In the cases that the result function, Eq. (G.1), takes the form of a product of the respective independent variables, i.e.,

$$R = x_1^{a_1} x_2^{a_2} x_3^{a_3} ... x_n^{a_n} \tag{G.3}$$

the relative uncertainty, ω_R/R, takes the following simple form

$$\frac{\omega_R}{R} = \left[\sum \left(\frac{a_i}{x_i} \omega_i \right)^2 \right]^{1/2} \tag{G.4}$$

For the case that the result function, R, cannot be written as an explicit function of independent variables, one can use the following relationship to estimate the uncertainty

associated with the measurements [2]

$$\frac{\omega_R}{R} = \left[\sum \left(\frac{\omega_i}{x_i}\right)^2\right]^{1/2} \tag{G.5}$$

G.1 Uncertainty analysis for pressure measurements for straight microchannels of rectangular cross-section

Pressure drop in its dimensionless form is usually referred to as the Poiseuille, fRe, which can be obtained from [3]

$$fRe = \frac{4}{\mu Q}\left(\frac{A^2\sqrt{A}}{L\Gamma}\right)\Delta p \tag{G.6}$$

where, fRe is defined based on the square root of cross-sectional area, $\sqrt{A}$,as the characteristic length scale, μ, is the viscosity, Q is the volumetric flow rate, L is the channel length, Γ is the wetted perimeter, and Δp is the measured pressure drop along the channel. Using Eq. (G.3), the relative uncertainty associated with fRe can be obtained from the following relationship [3]

$$\frac{\omega_{fRe}}{fRe} = \sqrt{\left(\frac{\omega_{\Delta p}}{\Delta p}\right)^2 + \left(\frac{\omega_L}{L}\right)^2 + \left(\frac{\omega_\Gamma}{\Gamma}\right)^2 + \frac{25}{4}\left(\frac{\omega_A}{A}\right)^2 + \left(\frac{\omega_Q}{Q}\right)^2} \tag{G.7}$$

where ω_A/A and ω_Γ/Γ are the relative uncertainties associated with the cross-sectional area and wetted perimeter, respectively and can be obtained from the following relationships [3]:

$$\frac{\omega_A}{A} = 4\sqrt{(H\omega_W)^2 + (W\omega_H)^2} \tag{G.8}$$

$$\frac{\omega_\Gamma}{\Gamma} = 4\sqrt{\omega_W^2 + \omega_H^2} \tag{G.9}$$

where ω_W and ω_H are the uncertainties in the measurement of channel width and height, respectively. Table G.1 lists the uncertainties associated with the measured parameters in

Table G.1: Uncertainty values in measured parameters in the pressure measurement in straight channels of rectangular cross-section.

Parameter	Maximum uncertainty
$\Delta P_{measured}$	$\pm$0.0375 psi ($\pm$258 pa)
L	$\pm$0.02 mm
W	$\pm$3.6 μm
H	$\pm$3.6 μm
Q	$\pm$0.5% of the measurement

Table G.2: Uncertainty values of experimental Poiseuille number for tested microchannels.

Microchannel	Maximum uncertainty
# PPR-0.13	8.7%
# PPR-0.17	9.3%
# PPR-0.4	8.9%
# PPR-0.6	9.3%
# PPR-0.76	11.1%

the experiment performed for pressure measurement in straight microchannels of rectangular cross-section [my paper]. Table G.2 shows the maximum uncertainty associated for the fRe in different samples.

For the variable cross-seciton microchannels, dimensionless flow resistance defined as follows is reported [4]:

$$R^*_{\exp} = \frac{\left(\frac{\Delta p}{Q}\right)_{variable}}{\left(\frac{\Delta p}{Q}\right)_{straight}} \tag{G.10}$$

The uncertainty associated with the dimensionless flow resistance, $R^*_{\exp}$, can be obtained from the following relationship

$$\frac{\omega_R}{R} = \sqrt{\left(\frac{\omega_{\Delta p}}{\Delta p}\right)^2 + \left(\frac{\omega_Q}{Q}\right)^2} \tag{G.11}$$

Table G.3: Uncertainty values in measured parameters in the pressure measurement in variable cross-section channels of rectangular cross-section.

Parameter	Maximum uncertainty
$\Delta P_{measured}$	± 0.004 psi (± 30 pa)
Q	$\pm 0.5\%$ of the measurement

Table G.3 shows the uncertainty associated with the measured parameters.

The uncertainty calculated for this experiment was less than 5%.

G.2 Uncertainty analysis for groove depth measurements

The groove depth, d_g, is a complex function of laser power, $\dot{q}$, beam speed, U, spot size, d_s, thermal diffusivity, α, and absorption coefficient, γ:

$$d_g = f\left(\dot{q}, U, d_s, \alpha, \gamma\right) \tag{G.12}$$

Using Eq. (G.5), the following relationship can be used to estimate the uncertainty associated with the measured depth

$$\frac{\omega_{d_g}}{d_g} = \sqrt{\left(\frac{\omega_{\dot{q}}}{\dot{q}}\right)^2 + \left(\frac{\omega_U}{U}\right)^2 + \left(\frac{\omega_{d_s}}{d_s}\right)^2 + \left(\frac{\omega_\alpha}{\alpha}\right)^2 + \left(\frac{\omega_\gamma}{\gamma}\right)^2} \tag{G.13}$$

Table G.4: Estimated uncertainty of involving parameters in the experimental test.

Parameter	Maximum uncertainty
$\omega_{\dot{q}}/\dot{q}$	11.1%
ω_U/U	2.0%
ω_{d_s}/d_s	3.9%
ω_α/α	5.0%
ω_γ/γ	5.0%

Bibliography

[1] J.P. Holman and W.J. Gajda, Experimental methods for engineers, (2001) McGraw-Hill New York.

[2] J.R. Taylor, Introduction to Error Analysis:The Study of Uncertainties in Physical Measurements, (1997) University Science Books, Herndon, VA.

[3] M. Akbari, D. Sinton, and M. Bahrami, Pressure drop in rectangular microchannels as compared with theory based on arbitrary cross section, J. of Fluids Engineering 131 (2009) 041202.

[4] M. Akbari, D. Sinton, and M. Bahrami, Viscous flow in variable cross-section microchannels of arbitrary shapes, Int. J.Heat and Mass Transfer 54 (2011) 3970-3978.

Appendix H

Experimental and numerical data

This appendix contains the experimental and numerical data obtained in the present study.

Table H.1: Variation of Poiseuille number versus Reynolds number in straight channels of rectangular cross-section.

Sample# PPR-0.13						
$Re_{\sqrt{A}}$	2.25	3.35	4.50	5.74	6.94	29.04
$fRe_{\sqrt{A}}$	0.84	0.92	0.86	0.99	0.96	0.97
Sample# PPR-0.17						
$Re_{\sqrt{A}}$	2.77	8.23	16.51	25.50	31.34	38.01
$fRe_{\sqrt{A}}$	0.86	1.12	0.95	1.01	0.97	0.98
Sample# PPR-0.4						
$Re_{\sqrt{A}}$	3.30	4.40	5.45	6.56	13.16	23.25
$fRe_{\sqrt{A}}$	0.97	0.96	0.78	1.01	1.11	0.98
Sample# PPR-0.6						
$Re_{\sqrt{A}}$	4.54	6.79	9.09	11.39	13.68	27.32
$fRe_{\sqrt{A}}$	1.04	1.03	1.02	1.02	1.03	1.03
Sample# PPR-0.76						
$Re_{\sqrt{A}}$	5.64	8.51	11.39	14.21	17.03	34.11
$fRe_{\sqrt{A}}$	0.98	0.96	0.94	0.95	0.93	0.92

Table H.2: Variation of Poiseuille number versus Reynolds number in straight channels of rectangular cross-section.

aspect ratio, ε	0.13	0.17	0.4	0.6	0.76
$fRe_{\sqrt{A}}$	28.70	27.16	16.67	15.00	12.87

Table H.3: Variation of Poiseuille number versus Reynolds number in straight channels of rectangular cross-section.

Sample #	ξ	ε_0	$R^*_{\text{mod.}}$	$R^*_{\text{exp.}}$	$\left(R^*_{\text{mod.}} - R^*_{\text{exp.}}\right)/R^*_{\text{mod.}} * 100$
1	0.09	0.09	1.10	1.11	$+0.91$
2	0.27	0.25	1.34	1.32	-1.42
3	0.42	0.22	1.58	1.62	$+2.53$
4	0.42	0.32	1.65	1.58	-4.24
5	0.53	0.33	1.81	1.83	$+1.05$

Table H.4: Comparison of the proposed model and the numerical results.

$\phi = 2^\circ$							
		$Re = 1$		$Re = 10$		$Re = 100$	
$a_{\min}/a_{\max}$	model	numerical	difference%	numerical	difference%	numerical	difference%
0.5	4.67	4.59	-1.7	4.59	-1.7	4.96	+6.2
0.6	3.02	2.97	-1.7	2.98	-1.7	3.14	+3.7
0.7	2.13	2.09	-1.7	2.09	-1.7	2.17	+1.9
0.8	1.59	1.56	-1.8	1.56	-1.8	1.59	0
0.9	1.24	1.21	-2.2	1.22	-1.6	1.23	-0.8
1	1	1	0	1	0	1	0
$\phi = 7^\circ$							
		$Re = 1$		$Re = 10$		$Re = 100$	
$a_{\min}/a_{\max}$	model	numerical	difference%	numerical	difference%	numerical	difference%
0.5	4.67	4.67	0	4.72	+1.2	6.00	+28.6
0.6	3.02	3.02	0	3.05	+0.9	3.55	+17.2
0.7	2.13	2.12	-0.2	2.14	+0.7	2.33	+9.7
0.8	1.59	1.58	-0.2	1.60	+0.7	1.66	+4.5
0.9	1.24	1.24	-0.6	1.24	0	1.25	+0.6
1	1	1	0	1	0	1	0
$\phi = 15^\circ$							
		$Re = 1$		$Re = 10$		$Re = 100$	
$a_{\min}/a_{\max}$	model	numerical	difference%	numerical	difference%	numerical	difference%
0.5	4.67	5.01	+7.3	5.25	+12.4	7.33	+57.0
0.6	3.02	3.24	+7.3	3.33	+10.0	4.11	+36.0
0.7	2.13	2.26	+6.2	2.32	+8.9	2.57	+20.7
0.8	1.59	1.67	+5.4	1.70	+6.7	1.76	+10.7
0.9	1.24	1.28	+3.4	1.29	+3.7	1.32	+6.8
1	1	1	0	1	0	1	0

Table H.5: Variation of the channel depth in micrometer with the beam speed for two typical constant beam powers.

U^*	$P^* = 0.2$	$P^* = 0.4$
0.4	157	212
0.5	142	177
0.7	121	164
0.8	131	150

Table H.6: Variation of the channel depth in micrometer with the beam power for constant beam speed.

P^*	$U^* = 1$
0.2	90
0.3	118
0.4	141
0.6	156
0.7	160

Table H.7: Variation of maximum temperature rise versus time for a typical heater width of 1.5 mm.

	heating		cooling	
time $[s]$	$T_{\max}$ $[^\circ C]$	$\Delta T_{\max}$ $[^\circ C]$	$T_{\max}$ $[^\circ C]$	$\Delta T_{\max}$ $[^\circ C]$
0	29.1	-0.9	53.4	23.4
2	29.3	-0.7	50.1	20.1
4	31.9	1.9	48.4	18.4
6	33.9	3.9	44.3	14.4
8	36.1	6.1	40.0	10.0
10	38.5	8.5	39.9	9.9
12	39.0	9.0	36.9	6.9
14	42.2	12.2	35.1	5.1
16	45.5	15.5	33.3	3.3
18	45.9	15.9	36.1	6.1
20	46.9	16.9	33.9	3.9
22	46.6	16.6	31.3	1.3
24	48.0	18.0	31.7	1.7
26	49.5	19.5	32.7	2.7
28	47.5	17.5	32.3	2.3
30	47.2	17.2	33.3	3.3
32	48.1	18.1	30.4	0.4
34	47.6	17.6	31.7	1.7
36	48.2	18.2	30.9	0.9
38	47.4	17.4	33.6	3.6
40	49.9	19.9	30.4	0.4
42	49.2	19.2	30.4	0.4

Table H.8: Peak sample concentration versus time for two focusing trials.

time $[s]$	Trial 1	Trial 2
0	1	1
20	14.4	1
40	18.3	1.23
60	24.0	19.9
80	31.3	23.8
100	36.9	29.4
120	44.4	35.9
140	49.9	49.8
160	62.2	78.2
180	73.5	68.8
200	89.0	105.7
220	102.6	133.3
240	115.9	159.0
260	106.4	168.2
280	116.1	199.8
300	148.8	219.4
320	162.5	252.8
340	189.1	272.7
360	146.4	254.5
380	205.4	262.0
400	220.3	262.1
420	216.7	339.2